

# Fatigue Behaviour of Steel Reinforcement Bars at Very High Number of Cycles

THÈSE N° 6382 (2014)

PRÉSENTÉE LE 22 OCTOBRE 2014

À LA FACULTÉ DE L'ENVIRONNEMENT NATUREL, ARCHITECTURAL ET CONSTRUIT  
LABORATOIRE DE MAINTENANCE, CONSTRUCTION ET SÉCURITÉ DES OUVRAGES  
PROGRAMME DOCTORAL EN GÉNIE CIVIL ET ENVIRONNEMENT

ÉCOLE POLYTECHNIQUE FÉDÉRALE DE LAUSANNE

POUR L'OBTENTION DU GRADE DE DOCTEUR ÈS SCIENCES

PAR

Marina ROCHA PINTO PORTELA NUNES

acceptée sur proposition du jury:

Prof. N. Geroliminis, président du jury  
Prof. E. Brühwiler, Prof. A. Nussbaumer, directeurs de thèse  
Dr S. Michel, rapporteur  
Dr A. Pipinato, rapporteur  
Dr C. Zeltner, rapporteur



ÉCOLE POLYTECHNIQUE  
FÉDÉRALE DE LAUSANNE

Suisse  
2014

*“In fatigue and solitude men emanate the divine.”*

— Louis-Ferdinand Céline, *Journey to the End of the Night*



---

## *Foreword*


---

Today's engineering methods of fatigue safety verification of existing civil structures like reinforced concrete bridges are still based on conservative methodologies used for the design of new structures and on incomplete knowledge on the fatigue behaviour of steel rebars in particular in the relevant domain of very high number of cycles at relatively low fatigue stresses, as experienced by reinforced concrete bridge deck slabs.

This situation often leads to the unsatisfactory situation that the fatigue safety of existing bridges cannot be verified "on paper" although there are no signs of any fatigue damage. This situation may lead to costly unnecessary interventions for strengthening or even replacement of bridges. Consequently, there is an obvious need to improve knowledge about the fatigue behaviour of reinforced concrete elements subjected to very high number of stress cycles, in particular for steel reinforcing bars which are the fatigue vulnerable part of reinforced concrete.

In her doctoral thesis, Marina Rocha investigates the fatigue behaviour of steel reinforcement bars at very high number of stress cycles using concepts of mechanics of materials including micro and macro structural material aspects and fracture mechanics. By an increase in knowledge about the fatigue behaviour of reinforced concrete, more realistic methods for the examination of existing bridges will be developed contributing to devise novel ways how to "get more out of an existing structure subjected to fatigue". This thesis contributes to this ambitious goal and is thus much relevant from a socio-economic viewpoint and sustainability of civil structures.

The doctoral thesis by Marina Rocha contains a significant amount of new data and information on the fatigue behaviour of steel reinforcement bars subjected to very high number of stress cycles. The research includes fatigue test results at very high number of stress cycles, micro-macro structural material characterisation of



steel rebars as well as numerical and analytical modelling to investigate the main parameters influencing the fatigue behaviour and fatigue strength of steel rebars.

With her doctoral thesis, Marina Rocha provides the proof of her capabilities to conduct a significant scientific study and to solve complex scientific questions by applying scientific approaches. The present thesis delivers results and findings that are useful and applicable to improve structural engineering methods for the fatigue safety verification of existing reinforced concrete structures. In the name of the whole MCS Team, I thank Marina for her constant and thorough investment in the thesis topic as well as for her professional skills and personal qualities.

Lausanne, September 2014

Professor Eugen Brühwiler

---

## *Acknowledgements*

---


My gratitude firstly goes to Prof. Eugen Brühwiler (MCS Lab.), director of my thesis and Prof. Alain Nussbaumer (ICOM Lab.), co-director, for their support, patience and valuable advices and interesting discussions on a broad range of topics. I would also like to thank Prof. Brühwiler who gave me the opportunity to work in a high-quality research environment.

I would like to thank MCS and Vale for funding this research, Dr. Zeltner and Mr. Opatz, from Stahl Gerlafingen, for the donation of the specimens analysed in the thesis as well as for the information provided on the rebars.

My sincere thanks go to the examining committee for their valuable input: Dr. Silvain Michel (EMPA) who also helped me with the fatigue tests, Dr. Alessio Pipinato (University of Padova) Dr. Christoph Zeltner (Stahl Gerlafingen) and Prof. Nikolas Geroliminis (chairman).

I wish to express my gratitude to Sylvain Demierre, Frédérique Dubugnon, Danièle Laub (CIME), Cyril Dénéreaz (LMM), Dr. Emmanuelle Boehm-Courjault (LSMX), Dr. Cayron (CEA-Grenoble) who greatly helped me with the experimental work and analysis.

I have spent a memorable time at MCS thanks to Dr. Denarié, Christine, Hamid, Florence, Alexis, Talayeh, Hadi, Tohru, Mark, Maléna, Vasileios, Christophe and also other friends: Paulo, Francisco and Maria, Farshid, Toktam and Parastoo, Luca and Fran-cesca, José and Adriana, Alessandro, José Pedro, Manuel, Raphaël, Mohadeseh, Petra and the rest of my peers in doctoral school. Thank you for the time we spent together inside as well as outside of the EPFL.



I offer my most sincere thanks to my family, specially my parents, for their support and encouragement. This work couldn't have been done without the unconditional support of Julien whom I am deeply grateful to.

---

## *Abstract*


---

A large portion of reinforced concrete (RC) bridges in the western world were built in the second half of the last century. RC bridge deck slabs are nowadays often subjected to increased traffic loading and volume than originally designed for and thus, steel reinforcement bars (rebars) are more susceptible to fatigue damage. Fatigue life of rebars can be largely affected by the crack initiation phase characterised by the growth of short cracks. The approaches available for fatigue damage evaluation of rebars fail to predict the crack initiation phase. Microstructural barriers control the short crack behaviour which can be significantly different from the stable long crack growth described by Paris' law. The stochastic nature of the fatigue life comes mainly from the scatter of these short cracks. Research on this domain is attractive since it can help to understand more accurately the fatigue behaviour of rebars. A better understanding can result in more accurate fatigue damage evaluation of RC elements.

The aim of this thesis is to predict the scatter and fatigue behaviour of hot rolled (HR), cold worked (CW) as well as quenched and self-tempered (QST) rebars incorporating the crack initiation phase. The research commences with an experimental investigation on the fatigue strength of QST rebars under high and very high cycle fatigue (HCF-VHCF) at constant amplitude ( $R=0.1$ ). A non-destructive inspection technique was applied for surface crack detection based on the frequency change monitored during the tests.

Surface and near surface macro residual stresses on QST rebars were determined by X-ray diffraction and Cut Compliance techniques. Surface imperfections and roughness were identified with Scanning Electron Microscopy mainly near the ribs. A parametric study of the rebar geometry, using 3D Finite Element Models, allowed to determine the influence of rib inclination and rebar diameter on the stress concentration factors.





A short crack growth model was developed to study the scatter resulting from the interaction between short crack and microstructural barriers. The model includes dispersion of grain orientation ratio, grain size variation and different phases (ferrite-pearlite and martensite). This model was then modified to include the surface roughness effects and long crack propagation. The stress concentration factor was considered as a constant parameter. The model predicted the fatigue behaviour of HR-CW and QST rebars.

**Keywords:** Steel reinforcement bars; Fatigue tests under HCF-VHCF; Micro-macro structural surface characterisation; Constant amplitude; Short crack growth model; Scatter; Fatigue behaviour prediction.

---

## Résumé

---

Une grande partie des ponts en béton armé (BA) dans le monde occidental ont été construits au cours de la seconde moitié du siècle dernier. Les dalles en BA de ponts sont aujourd'hui soumises à des charges et volumes accrus vis-à-vis de leur conception initiale et par conséquent, les barres d'armature en acier sont plus sensibles aux dommages de fatigue résultants de l'augmentation du trafic. La résistance à la fatigue des armatures peut-être en grande part influencée par la phase d'initiation des fissures — caractérisée par la croissance de fissures courtes. Les approches disponibles pour l'évaluation des dommages en fatigue des armatures ne parviennent pas à prédire la phase d'initiation des fissures. Les barrières microstructurelles contrôlent le comportement des fissures courtes qui diffère de celui des fissures longues décrites par la loi de Paris en régime stable. La nature stochastique de la vie en fatigue provient principalement de la dispersion générée par les fissures courtes. La recherche dans ce domaine est intéressante, car elle peut aider à appréhender plus précisément le comportement en fatigue des armatures. Une meilleure compréhension entraînera une plus grande précision de l'évaluation des dommages en fatigue des éléments en BA.

L'objectif de cette thèse est de prédire la dispersion et le comportement des essais de fatigue des barres d'armature laminées à chaud (HR), travaillées à froid (CW) ainsi que des barres trempées et revenues (QST) en considérant la phase d'initiation des fissures. Le projet de recherche débute par une étude expérimentale de la résistance à la fatigue des armatures QST à grand et très grand nombre de cycles (HCF-VHCF) à amplitude constante ( $R=0.1$ ). Une technique d'inspection non destructive a été appliquée pour la détection des fissures de surface se basant sur la variation de la fréquence mesurée pendant les essais.

Les contraintes résiduelles macroscopiques de surface et près de la surface des armatures QST ont été déterminées par diffraction des rayons X et par la méthode

”Cut Compliance”. Les imperfections de surface et la rugosité ont été identifiées principalement près des nervures par microscopie électronique à balayage. Une étude paramétrique de la géométrie des barres d’armature, à l’aide de modèles 3D par éléments finis, a permis de déterminer l’influence de l’inclinaison de la nervure et du diamètre des barres d’armature sur les facteurs de concentration des contraintes.

Un modèle de propagation des fissures courtes a été développé pour étudier la dispersion résultant de l’interaction entre les fissures courtes et les barrières microstructurales. Le modèle inclut la dispersion liée à l’orientation cristallographique des grains, à la variation de la taille des grains et des phases (ferrite-perlite et martensite). Ce modèle a ensuite été amélioré pour inclure les effets de la rugosité de surface ainsi que la phase de propagation linéaire des fissures longues. Le facteur de concentration de contrainte a été considéré comme un paramètre constant. Le modèle a prédit le comportement en fatigue des armatures HR-CW et QST.

**Mots-clés :** Barres d’armature en acier ; Essais en fatigue HCF-VHCF ; Caractérisation microstructurale et macrostructurale de surface ; Modèle de propagation de fissures courtes ; Dispersion ; Prédiction du comportement en fatigue.

---

## *Resumo*

---

Uma grande parte das pontes de concreto armado (CA) no mundo ocidental foi construída na segunda metade do século passado. Atualmente, as lajes em CA das pontes estão sujeitas a um aumento de carga e volume de tráfego em relação ao projeto inicial e, conseqüentemente, as barras de aço estão mais suscetíveis a danos por fadiga. A vida à fadiga das barras pode ser, em grande parte, influenciada pela fase de iniciação das fissuras caracterizada pelo crescimento de microfissuras. Os métodos utilizados para avaliação dos danos por fadiga em barras de aço são incapazes de prever essa fase de iniciação. Barreiras microestruturais controlam o comportamento das microfissuras o qual pode diferenciar significativamente do crescimento estável das fissuras descrito pela lei de Paris. A natureza estocástica da vida à fadiga é principalmente influenciada pela dispersão gerada pelas microfissuras. Pesquisa nessa área é relevante pois contribui para um melhor entendimento do comportamento à fadiga das barras e, portanto, uma avaliação mais precisa do dano por fadiga em elementos de CA.

O objetivo desta tese é prever a dispersão e comportamento à fadiga das barras de aço laminadas a quente (HR), trabalhadas a frio (CW) assim como temperadas e revenidas (QST) considerando a fase de iniciação das fissuras. Este projeto de pesquisa inicia-se por uma investigação experimental da resistência à fadiga das barras QST sujeitas a alto e muito alto ciclos à amplitude constante ( $R=0.1$ ). Uma técnica de inspeção não destrutiva foi utilizada para identificação de fissuras na superfície da barra baseada na variação da frequência monitorada durante os ensaios.

Tensões residuais macroscópicas foram determinadas na superfície e subsuperfície das barras QST por difração de raio X e o método "Cut Compliance". Imperfeições e rugosidade da superfície foram identificadas principalmente próximas aos dentes das barras pelo microscópio eletrônico de varredura. Um estudo paramétrico da geometria das barras usando modelos 3D de elementos finitos permitiu deter-

minar a influência da inclinação dos dentes e do diâmetro das barras nos fatores de concentração de tensão.

Um modelo de crescimento de microfissuras foi desenvolvido para estudo da dispersão resultante da interação entre fissuras e barreiras microestruturais. O modelo inclui a dispersão da razão de orientação dos grãos, variação do tamanho do grão e diferentes fases (ferrita-perlita e martensita). Este modelo foi posteriormente modificado para inclusão dos efeitos da rugosidade da superfície e propagação de microfissuras. O fator de concentração de tensão foi considerado como um parâmetro constante. O modelo previu o comportamento à fadiga das barras HR, CW e QST.

**Palavras-chave:** Barras de aço; Ensaios de fadiga a HCF-VHCF; Caracterização micro e macroestrutural da superfície; Amplitude constante; Modelo de crescimento das microfissuras; Dispersão; Previsão do comportamento à fadiga.

---

# Contents

---

<b>Foreword</b>	<b>v</b>
<b>Acknowledgements</b>	<b>vii</b>
<b>Abstract</b>	<b>ix</b>
<b>Résumé</b>	<b>xi</b>
<b>Resumo</b>	<b>xiii</b>
<b>Contents</b>	<b>xviii</b>
<b>List of Figures</b>	<b>xxiv</b>
<b>List of Tables</b>	<b>xxv</b>
<b>1 Introduction</b>	<b>1</b>
1.1 Objectives of thesis . . . . .	3
1.2 Scope of thesis . . . . .	3
1.3 Structure of thesis . . . . .	4
<b>2 Very high cycle fatigue tests of quenched and self-tempered steel reinforcement bars</b>	<b>9</b>
2.1 Introduction . . . . .	11
2.2 Material properties . . . . .	12
2.3 Test details . . . . .	14
2.3.1 Grip arrangement and specimen preparation. . . . .	14
2.3.2 Test method . . . . .	16
2.4 Results and discussions . . . . .	18

xv

2.4.1	Test results . . . . .	18
2.4.2	Non-destructive inspection . . . . .	19
2.4.3	Fractured surface analyses . . . . .	21
2.5	Conclusions . . . . .	26
2.6	Acknowledgements . . . . .	26

**3 Material and geometrical characterisation of quenched and self-tempered steel reinforcement bars 29**

3.1	Introduction . . . . .	31
3.2	Material characteristics . . . . .	32
3.3	Fabrication process . . . . .	33
3.4	Microstructure . . . . .	34
3.4.1	Metallographic analysis . . . . .	34
3.4.2	Grain size and area fraction . . . . .	35
3.4.3	Microhardness test . . . . .	36
3.5	Residual stresses . . . . .	37
3.5.1	Residual stress on QST rebars . . . . .	37
3.5.2	Cut Compliance technique . . . . .	38
3.5.3	X-ray diffraction technique . . . . .	41
3.5.4	Results and discussion . . . . .	43
3.6	Surface imperfections . . . . .	44
3.7	Stress concentration . . . . .	46
3.7.1	Stress concentration on the ribbed profile . . . . .	46
3.7.2	Numerical analysis . . . . .	46
3.7.3	$K_t$ determined on the rib . . . . .	50
3.8	Conclusions . . . . .	56
3.9	Acknowledgements . . . . .	57

**4 Microstructural influence on the scatter in the fatigue life of steel reinforcement bars 63**

4.1	Introduction . . . . .	65
4.2	Reconstruction of parent austenite grains . . . . .	68
4.2.1	Experimental analysis . . . . .	68
4.3	Short crack growth model . . . . .	70
4.3.1	Grain structure . . . . .	70
4.3.2	Grain orientation . . . . .	75
4.3.3	Material properties . . . . .	77

4.4	Results and Discussion . . . . .	78
4.5	Conclusion . . . . .	81
4.6	Acknowledgements . . . . .	82
<b>5</b>	<b>Fatigue behaviour prediction of steel reinforcement bars using an adapted Navarro and De Los Rios model</b>	<b>89</b>
5.1	Introduction . . . . .	91
5.2	Crack growth model . . . . .	92
5.2.1	Threshold for short crack growth . . . . .	94
5.2.2	$f$ function . . . . .	95
5.3	Surface roughness . . . . .	95
5.3.1	3D surface roughness profile . . . . .	96
5.3.2	Fatigue stress concentration factor . . . . .	98
5.4	Stress concentration factor-rib geometry . . . . .	99
5.5	Results and discussion . . . . .	100
5.6	Conclusion . . . . .	102
<b>6</b>	<b>Conclusion</b>	<b>109</b>
6.1	Introduction . . . . .	109
6.2	Response to research questions . . . . .	109
6.2.1	Fatigue testing . . . . .	109
6.2.2	Micro-macro structural characterisation . . . . .	110
6.2.3	Analytical model-part I . . . . .	111
6.2.4	Analytical model-part II . . . . .	112
6.3	Future work . . . . .	113
6.3.1	Fatigue crack detection . . . . .	113
6.3.2	Grain orientation ratio . . . . .	113
6.3.3	Surface roughness . . . . .	113
6.3.4	Fatigue behaviour modelling-other methods . . . . .	113
<b>A</b>	<b>Stress-Strain curve</b>	<b>117</b>
<b>B</b>	<b>Rebar <math>K_t</math></b>	<b>119</b>
B.1	D10h03r02 . . . . .	120
B.2	D10h08r02 . . . . .	121
B.3	D10h08r04 . . . . .	122
B.4	D10h15r04 . . . . .	123
B.5	D10h08 . . . . .	124



B.6	D16ho3ro2	125
B.7	D16ho8ro2	126
B.8	D16ho8ro4	127
B.9	D16ho8ro8	128
B.10	D16ho8	129
B.11	D16ho8ro4co4	130
B.12	D16ho8ro4c12	131
B.13	D26ho3ro2	132
B.14	D26ho8ro2	133
B.15	D26ho8ro4	134
B.16	D26h15ro4	135
B.17	D26h15ro8	136
<b>C</b>	<b>Model</b>	<b>137</b>
C.1	File experiment.m	138
C.2	File mainNR.m	140
C.3	File classTM.m	159
C.4	File classFP.m	167
<b>D</b>	<b>3D Surface</b>	<b>175</b>
<b>E</b>	<b>S-N-P fatigue curves using maximum likelihood</b>	<b>177</b>
E.1	Statistical evaluation of S-N-P curves	178
E.1.1	Statistical evaluation of S-N-P curves based on EN background documentation	178
E.1.2	Statistical evaluation of S-N-P curves based on maximum likelihood approach	179
E.2	Results of statistical analysis	181
E.3	Discussion of statistical analysis results	185
<b>F</b>	<b>Curriculum Vitae</b>	<b>189</b>

---

## *List of Figures*

---

1.1	Structure of the thesis. . . . .	5
2.1	Etched cross section of a 16 mm diameter QST rebar. . . . .	14
2.2	(a) Initial grip system used for the fatigue tests. Rebar failure in the grip area with (b) Aluminium sheet; (c) Shot peened rebar ends; (d) Welded and machined rebar. . . . .	15
2.3	(a) Conical grip system used for the fatigue tests; (b) Detail of the conical grip. . . . .	16
2.4	Rib patterns at both sides of the tested QST rebars. . . . .	16
2.5	Representative frequency drop (%) of a failed specimen during the fatigue test. . . . .	17
2.6	Frequency drop versus number of cycles obtained for specimens 7, 14 & 15. . . . .	19
2.7	(a) Specimen 15: Two dots of penetrant ink indicating the fatigue crack tips on the specimen surface; (b) Crack on the specimen surface when the test was stopped. . . . .	20
2.8	Frequency drop versus number of cycles obtained for specimens 1, 2 & 3. . . . .	20
2.9	Frequency drop versus number of cycles obtained for specimens 4, 5 & 6. . . . .	21
2.10	Frequency drop versus number of cycles obtained for specimens 8, 9 & 10. . . . .	21
2.11	Frequency drop versus number of cycles obtained for specimens 11, 12 & 13. . . . .	22

2.12	(a) Location where fatigue crack initiates on the surface of specimen 7; (b) OM image (10×) of the fractured cross section; (c) SEM image (65×) of the imperfection from where fatigue crack initiated. . . . .	23
2.13	(a) Location where fatigue crack initiates on the surface of specimen 14; (b) OM image (10×) of the fractured cross section; (c) SEM image (65×) of the imperfection from where fatigue crack initiated. . . . .	24
2.14	(a) Location where fatigue crack initiates on the surface of specimen 15; (b) OM image (10×) of the fractured cross section; (c) SEM image (65×) of the imperfections from where fatigue crack initiated. . . . .	25
3.1	(a) Etched cross section of the QST rebar; (b) Tempered martensite (TM); (c) Transition zone (TZ) of acicular ferrite (light areas) and pearlite (darker areas); (d) Quasi-equiaxed ferrite (light areas) and pearlite (dark areas) (F-P). . . . .	35
3.2	Hardness map of the QST rebars with diameters of 16, 26 and 34 mm. . . . .	37
3.3	Cut Compliance technique. . . . .	38
3.4	Location and orientation of cuts and strain gauges after measurements. . . . .	39
3.5	Longitudinal residual stress profile determined on the rebar subsurface. . . . .	40
3.6	Path difference. . . . .	41
3.7	Locations of the X-ray measurements between non-uniform ribs. . . . .	42
3.8	Locations of the X-ray measurements between uniform ribs. . . . .	42
3.9	Longitudinal residual stresses obtained on the rebar surface and subsurface by X-ray diffraction technique. . . . .	43
3.10	Surface imperfections identified on QST rebars with diameter of 16 mm (a) Marks near the transversal rib; (b) Semi-circular marks near the transversal rib. . . . .	44
3.10	Surface imperfections identified on QST rebars with diameter of 16 mm (c) Marks and cracks near the transversal rib; (d) Cracks near the transversal rib; (e) Cracks perpendicular to the longitudinal rib; (f) Location of the analysed imperfections on the QST rebar surface. . . . .	45
3.11	Illustration of the ribbed profile. . . . .	46
3.12	Illustration of the rib geometry and the paths along and perpendicular to the ribs where stress concentrations were investigated. . . . .	48
3.13	Typical mesh considered in the models. . . . .	49
3.14	Mesh convergence for rib radius $r=0.2$ mm. . . . .	49

3.15	Stress concentration profile obtained in a perpendicular to the rib axis of D26ho8ro2 model. . . . .	50
3.16	$K_t$ curves obtained for different rib inclinations $\theta$ of D16ho8ro4 and D16ho8ro4 $\theta$ 90 models. . . . .	51
3.17	Example of the peak positions (PP)s and peak zones (PZ)s along the rib of an original model. . . . .	53
3.18	Influence of the rib inclination $\theta$ on $K_t$ . . . . .	53
3.19	Influence of the rib radius $r$ on $K_t$ . . . . .	54
3.20	Influence of the rib height $h$ on $K_t$ . . . . .	55
3.21	Influence of the rebar diameter $D$ on $K_t$ . . . . .	55
3.22	Influence of the rib spacing $c$ on $K_t$ . . . . .	56
4.1	Two-zone [6], [7] and three-zone [10] models. . . . .	67
4.2	Reconstruction of the austenite grains in the QST rebar: (a) Martensite grains obtained from EBSD analyses; (b) Reconstructed austenite grains determined from ARPGE software. . . . .	69
4.3	Example of a simulation result obtained in F-P with a crack length $2a \approx 8D_m$ at $N = 2 \times 10^6$ cycles: (a) Illustration of a surface short crack growth in ferrite (dark grey) and pearlite (ligh grey) grains represented by Voronoi cells; (b) Short crack growth rate as a function of the crack length. . . . .	71
4.4	Schematic diagram of the crack with its plastic zones in the grains. . . . .	73
4.5	Illustration of a subsurface crack growth and variation of the grain orientation ratio $m_i/m_1$ : (a) A crack length $2a$ reaches 7 grains on the surface, the subsurface crack tip extends over $\mathfrak{N} = 14$ grains; (b) The graph represents the evolution of $m_i/m_1$ scatter as the crack grows using Eq. 4.10; To illustrate this scatter, it was computed 1000 $m_i/m_1$ values for each step. The greyscale represents the amount of $m_i/m_1$ with same values in a region. In the first step, $m_i/m_1=1$ and there is no dispersion. In the second step, a higher dispersion is obtained compared to the 10th step when the dispersion decreases. The red lines represent the evolution of $m_i/m_1$ obtained by Eq. 4.9. . . . .	76
4.6	Scatter obtained for different area fractions % of pearlite in the F-P model. . . . .	79

4.7	Distribution of failures points obtained in the model and experimental data: <b>(a)</b> For F-P model with an area fraction of 53% of pearlite and HR-CW rebars [43, 44]; <b>(b)</b> For TM model and QST rebars [45–47]. . . . .	80
5.1	Flowchart of the adapted N-R model used in this work. . . . .	93
5.2	Roughness on the surface of a QST rebar near the rib. . . . .	96
5.3	3D profile of the surface roughness of the QST rebar obtained by photometric stereo technique. . . . .	97
5.4	Illustration of a surface roughness profile obtained for the QST rebar and the surface roughness parameters. . . . .	97
5.5	Dispersion determined for the stress concentration fatigue factor $K_f$ from the surface roughness profile obtained for the QST rebar. . . . .	99
5.6	Illustration of the critical zone along the ribs considered in this work. . . . .	99
5.7	Data points including the crack initiation phase (green marks: fatigue crack size = 1 grain; blue marks: fatigue crack size = 0.2 mm) in the F-P model and experimental data (black marks) of HR-CW rebars with diameter $D \leq 16$ mm [14, 15]. . . . .	102
5.8	Data points including the crack propagation phase (red marks) in the F-P model and experimental data (black marks) of HR-CW rebars with diameter $D \leq 16$ mm [14, 15]. . . . .	103
5.9	Data points including the crack initiation phase (green marks: fatigue crack size = 1 grain; blue marks: fatigue crack size = 0.2 mm) in the TM model and experimental data (black marks) of QST rebars with diameter $D \leq 16$ mm [9, 16, 17]. . . . .	104
5.10	Data points including the crack propagation phase (red marks) in the TM model and experimental data (black marks) of QST rebars with diameter $D \leq 16$ mm [9, 16, 17]. . . . .	104
5.11	Influence of the - 1) Microstructure and roughness together (all); 2) Microstructure, including grain orientation ratio $m_i/m_1$ , grain size variation, phases (ferrite-pearlite); 3) Each parameter of the microstructure separately and 4) Surface roughness - on the scatter obtained in the F-P model. . . . .	105

5.12	Influence of the - 1) Microstructure and roughness together (all); 2) Microstructure, including grain orientation ratio $m_i/m_1$ , grain size variation, phases (martensite); 3) Each parameter of the microstructure separately and 4) Surface roughness - on the scatter obtained in the TM model. . . . .	106
A.1	Stress $\times$ Strain curve of a QST rebar analysed in this thesis. . . . .	117
B.1	Paths (darker lines) where $K_t$ evolution was determined. . . . .	119
B.2	D10h03r02 model: (a) 3D FE mesh (b) Top view (c) $K_t$ plot (d) Bottom view. . . . .	120
B.3	D10h08r02 model: (a) 3D FE mesh (b) Top view (c) $K_t$ plot (d) Bottom view. . . . .	121
B.4	D10h08r04 model: (a) 3D FE mesh (b) Top view (c) $K_t$ plot (d) Bottom view. . . . .	122
B.5	D10h15r04 model: (a) 3D FE mesh (b) Top view (c) $K_t$ plot (d) Bottom view. . . . .	123
B.6	D10h08 model: (a) 3D FE mesh (b) Top view (c) $K_t$ plot (d) Bottom view. . . . .	124
B.7	D16h03r02 model: (a) 3D FE mesh (b) Top view (c) $K_t$ plot (d) Bottom view. . . . .	125
B.8	D16h08r02 model: (a) 3D FE mesh (b) Top view (c) $K_t$ plot (d) Bottom view. . . . .	126
B.9	D16h08r04 model: (a) 3D FE mesh (b) Top view (c) $K_t$ plot (d) Bottom view. . . . .	127
B.10	D16h08r08 model: (a) 3D FE mesh (b) Top view (c) $K_t$ plot (d) Bottom view. . . . .	128
B.11	D16h08 model: (a) 3D FE mesh (b) Top view (c) $K_t$ plot (d) Bottom view. . . . .	129
B.12	D16h08r04c04 model: (a) 3D FE mesh (b) Top view (c) $K_t$ plot (d) Bottom view. . . . .	130
B.13	D16h08r04c12 model: (a) 3D FE mesh (b) Top view (c) $K_t$ plot (d) Bottom view. . . . .	131
B.14	D26h03r02 model: (a) 3D FE mesh (b) Top view (c) $K_t$ plot (d) Bottom view. . . . .	132
B.15	D26h08r02 model: (a) 3D FE mesh (b) Top view (c) $K_t$ plot (d) Bottom view. . . . .	133



B.16 D26ho8ro4 model: **(a)** 3D FE mesh **(b)** Top view **(c)**  $K_t$  plot **(d)** Bottom view. . . . . 134

B.17 D26h15ro4 model: **(a)** 3D FE mesh **(b)** Top view **(c)**  $K_t$  plot **(d)** Bottom view. . . . . 135

B.18 D26h15ro8 model: **(a)** 3D FE mesh **(b)** Top view **(c)**  $K_t$  plot **(d)** Bottom view. . . . . 136

C.1 Model files: **(a)** file containing the input function to run an experiment; **(b)** the process will occur simultaneously in parallel on each core; **(c)** file containing all the function for the Voronoi structure and the propagation algorithm; **(d)** two files containing a class with properties for each of the two steels: TM & FP. . . . . 137

D.1 3D surface reconstruction using photometric stereo technique: **(a)**-**(d)** source SEM images. . . . . 175

D.1 3D surface reconstruction using photometric stereo technique: **(e)** 3D reconstructed surface. . . . . 176

---

## *List of Tables*

---

2.1	Chemical composition of the QST rebar with diameter of 16 mm. . .	13
2.2	Mechanical properties of the QST rebar with diameter of 16 mm. . .	13
2.3	Fatigue test results of 16 mm rebar. . . . .	18
3.1	Chemical composition of the QST rebars with diameters of 16, 26 and 34 mm. . . . .	33
3.2	Mechanical properties of QST rebars. . . . .	33
3.3	Average grain size of ferrite and area fraction of pearlite obtained in the core of QST rebars. . . . .	36
3.4	Geometrical parameters of the analysed models. . . . .	47
3.5	Peak values (PV)s and Peak positions (PP)s determined along the transition line (TL). . . . .	52
4.1	Material properties used in the model. . . . .	78
E.1	Summary of characteristic values of ML-based linearized S-N curves	184





LIST OF TABLES

## Context and motivation

In the second half of the last century, a significant increase in bridge construction was observed. This event was accompanied by the change from steel to reinforced concrete (RC) as the dominant structural material [1].

A survey performed on approximately 50 000 concrete bridges, (RC, prestressed and post-tensioned), by the railway administration in 17 European countries (including Switzerland), showed that about 80% of these bridges are classified as RC. From all concrete bridge types, 25% are less than 20 years old, 55% are between 20 and 50 years old, 16% are between 50 and 100 years old and 4% are over 100 years old [2].

In the United States, bridges have been mostly built in the last 50 years with RC material being predominant. RC bridges correspond to approximately 30% (or more than 140 000) of all bridge types in the United States [3].

Bridges are nowadays often subjected to increased traffic loading and volumes than originally designed for. RC bridge deck slabs can experience very high number of significant stress cycles during their service life i.e., exceeding 10 million cycles [3]. Thus, they are more susceptible to fatigue damage with a likely ultimate strength reduction of the building materials due to fatigue. Despite this fact, reinforced concrete deck slabs were commonly not designed for fatigue [4]. RC bridges built before 1989 in Switzerland, for example, often do not meet the current fatigue code requirements [5].

[4] and [6] showed that fatigue failure in slab-like members is always induced by the fracture of steel reinforcement bars (rebars). They are significantly more fatigue vulnerable than concrete which shows no or minor local fatigue damaging [4]. Therefore, the knowledge on the fatigue behaviour of rebars is of fundamental im-

portance for safety evaluation of RC elements.

Research on the fatigue strength of rebars was intensely carried out up to the 1980's on hot rolled (HR) and cold worked (CW) steels [7], [8] and [9]. Axial and bending fatigue tests were performed, under constant stress amplitude, on HR and CW rebars in air and embedded in concrete, respectively. These test results formed the basis of the standard S-N curves used still nowadays for fatigue safety verification. In the last decades, straight HR and CW steels have been replaced by quenched and self-tempered (QST) rebars. In some European countries, QST rebars were introduced in 1974 [10]. Straight QST rebars correspond to approximately 1/3 of the Swiss rebar market. Rebars with diameter greater than 20 mm are mainly QST steels; rebars with diameter smaller than 20 mm are mainly cold worked steels with very small diameters consisting of smooth cold worked bars. QST rebars are hot rolled steels followed by rapid water quenching. This process results in a harder outer surface layer compared to HR and CW rebars.

Although a large amount of experimental data of QST rebars is available, the test results are often limited to 2 million stress cycles with rarely tests exceeding 5 million cycles. These rebars have mostly shown improved fatigue strength and smaller scatter in the tests compared to HR and CW rebars.

The fatigue damage in rebars develops in two stages: crack initiation with nucleation and growth of short (micro) cracks followed by a linear long (macro) crack propagation until failure occurs. Rebar surface is a preferential site for fatigue crack initiation. Surface conditions may significantly influence the behaviour of short cracks. The understanding of the mechanisms of crack initiation is therefore a key issue.

In a damage-tolerance approach, it is assumed that a rebar contains an initial long crack. This crack propagates according to the Paris' law and since failure of one rebar is not failure of the slab, a different resistance factor is used. However, short cracks can behave significantly different from the long crack propagation predicted by Paris' law [11]. In addition, S-N curve approach used for fatigue life assessment, although relative simple and widely used, doesn't separate crack initiation and propagation phases.

Short crack growth models have been widely used to predict the fatigue behaviour of metals. The significance of microstructural features on the fatigue damage process is considered by these models. They can predict the behaviour of short cracks by simulating the interactions between crack and microstructural barriers.

## 1.1 Objectives of thesis

The main objectives of this thesis are summarised as follows:

1. Investigate experimentally the fatigue strength of QST rebars at high and very high number of constant amplitude stress cycles.
2. Characterise micro-macro structural aspects of QST rebars.
3. Investigate the influence of surface microstructure on the scatter above the fatigue limit of HR-CW and QST rebars.
4. Predict the scatter and fatigue behaviour of HR-CW and QST rebars.

## 1.2 Scope of thesis

This thesis focuses on the influence of surface microstructural features on the fatigue behaviour of rebars in the high and very high cycle domain. Both initiation (nucleation and short crack growth) and propagation of long fatigue cracks are important in understanding their behaviour. However, the prime importance of the crack initiation phase is addressed in this thesis.

In this research, microcracks or cracks coalescence are not considered. The analyses are restricted to fatigue under constant amplitude loadings (sequence, interaction effects are not studied). This research includes only straight rebars without concrete; no welding (rebars meshes) are analysed. The study covers only rebars tested under positive R-ratio ( $R=0$  to  $0.2$ ). The QST rebars analysed in this thesis were produced by Stahl Gerlafingen AG.

Fatigue tests with QST rebars carried out at high and very high number of stress cycles are discussed. It is followed by an experimental investigation of micro-macro structural surface conditions on QST rebars. A parametric study allowed to determine the influence of rib geometry on the stress concentration factors at the rebar surface. A model was then developed to quantify the contribution of microstructural parameters on the scatter found in fatigue tests. Although the experimental analyses were performed only on QST rebars, the model was also adapted to study the scatter on HR-CW rebars, present in older RC bridges. This model simulates the interactions between short crack and microstructural barriers. It considers stochastic crack initiation and long crack propagation phases. The model was applied for fatigue behaviour prediction of HR-CW and QST rebars and to investigate the scatter in fatigue tests. The model results were compared to experimental data.

### 1.3 Structure of thesis

The structure of this thesis and its contents are presented in Fig. 1.1. The thesis is divided in three parts: 1) Experimental, with fatigue test results and rebar characterisation 2) Theoretical, where a short crack model is developed 3) Application of the model to the scatter and fatigue behaviour prediction on experimental data.

This research consists of four journal papers, to be submitted, and appendices presented in an extended format.

**Chapter 2** presents axial fatigue test results of QST rebars between  $10^6$  and  $10^8$  stress cycles under constant amplitude,  $R=0.1$ . Gripping methods are investigated and a non-destructive inspection technique is proposed to detect surface cracks.

**Chapter 3** provides experimental investigation on surface and near surface residual stresses and surface imperfections on QST rebars. A parametric study using 3D Finite Element models is developed to determine the stress concentrations factors on the rebar surface.

**Chapter 4** presents a short crack growth model, adapted from Navarro and De Los Rios [12], which considers the dispersion in the grain orientation ratio, grain size variation and different phases on the scatter observed in experimental data as obtained above the fatigue limit.

**Chapter 5** presents modifications on the model developed in Chapter 4 to include surface roughness dispersion and long crack propagation. The stress concentration factor from the rib geometry is considered in the calculations. The model results are compared to experimental data.

Finally, **Chapter 6** summarises the main conclusions of the four previous or main chapters and suggests areas for future work in this field.

Supplementary information are presented in Appendices A to D which consist of:

- 3D Finite Element Models of the rebar geometry and stress concentrations analyses for different rib geometries;
- the algorithm developed for the short crack growth model presented in Chapters 3 and 4;
- the 3D roughness profile determined from the surface of the QST rebar;
- a Conference paper where an approach was proposed to determine S-N curve from fatigue test results including run-out results.

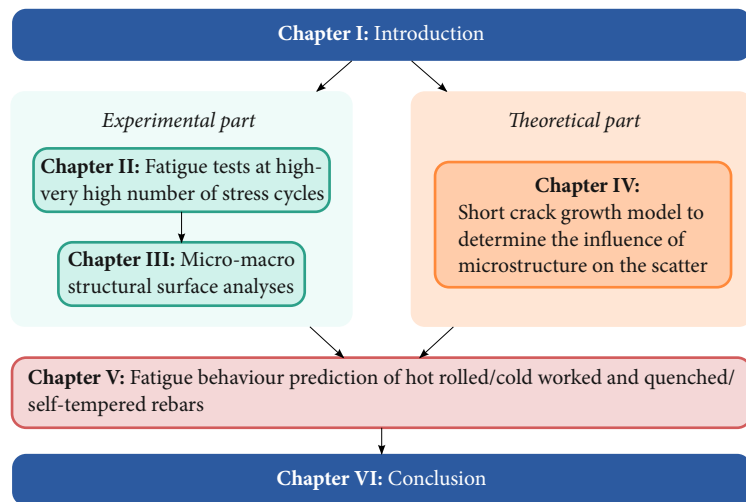


**Figure 1.1** – Structure of the thesis.



---

## Bibliography

---

- [1] Branco, F. A., & De Brito, J. (2004). Handbook of concrete bridge management. ASCE Publications.
- [2] Bell, B., & Rail, N. (2004). European railway bridge demography. European FP, 6.
- [3] Das, P. G. (1999). Management of highway structures. Thomas Telford, London.
- [4] Schläfli, M., & Brühwiler, E. (1997). Fatigue considerations in the evaluation of existing reinforced concrete bridge decks. IABSE reports, Rapports AIPC, IVBH Berichte, 76, 25-33.
- [5] Fehlmann, P., & Vogel, T. (2009). Experimental investigations on the fatigue behavior of concrete bridges. In IABSE Symposium Report, 96(5), 45-54. International Association for Bridge and Structural Engineering.
- [6] Johansson, U. (2004). Fatigue tests and analysis of reinforced concrete bridge deck models. Royal Institute of Technology, Stockholm.
- [7] Hanson, J. M., Somes, N. F., Helgason, T., Corley, W. G., & Hognestad, E. (1970). Fatigue strength of high-yield reinforcing bars. National Cooperative Highway Research program (NCHRP). Final report-Project n°4-7. Illinois.
- [8] Tilly, G. P. (1979). Fatigue of steel reinforcement bars in concrete: a review. Fatigue & Fracture of Engineering Materials & Structures, 2(3), 251-268.
- [9] Tilly, G. P. (1984). Fatigue testing and performance of steel reinforcement bars. Matériaux et Construction, 17(1), 43-49.



- [10] Virmani, Y. P., Wright, W., & Nelson, R. N. (1991). Fatigue testing for Thermex reinforcing bars. *Public Roads*, 55(3), 72-78.
- [11] Tokaji, K., & Ogawa, T. (1992). The growth behaviour of microstructurally small fatigue cracks in metals. *Short fatigue cracks*, ESIS, 13, 85-99.
- [12] Navarro, A., & De Los Rios, E. R. (1992). Fatigue crack growth modelling by successive blocking of dislocations. *Proceedings of the Royal Society of London. Series A: Mathematical and Physical Sciences*, 437(1900), 375-390.

## Very high cycle fatigue tests of quenched and self-tempered steel reinforcement bars

— Marina Rocha, Silvain Michel, Eugen Brühwiler, Alain Nussbaumer

**Abstract:** *Investigations on the fatigue strength of steel reinforcement bars (rebars) mainly involves fatigue tests with hot rolled (HR) and cold worked (CW) steels. However, in the last few decades, HR and CW rebars were replaced by quenched and self-tempered (QST) rebars with hardened surface layer. There still remains a lack of research on fatigue strength of QST rebars especially in the very high cycle domain i.e., number of stress cycles surpassing 5 million. This work aims to investigate the fatigue performance of QST rebars axially tested at number of stress cycles in the range of  $10^6$  to  $10^8$ . A preliminary study of the gripping method is followed by fatigue test results including non-destructive inspection of the rebar surface and fractographic analyses. The rebar surface is examined with liquid penetrant to reveal fatigue crack location and size in specific frequency interval monitored during the tests. Fractured surface analyses are performed by Scanning Electron Microscopy (SEM) to detect the location from where fatigue cracks initiate. Cross sectional area reduction resulting from fatigue crack propagation is also determined. Fractographic investigations are compared with the fractured surfaces of HR, CW and QST rebars from the literature.*

**Keywords:** Quenched and self-tempered rebars; High and very high cycle fatigue; Gripping method; Non-destructive inspection; Fractured surface analysis.



## Contents

---

<b>2.1</b>	<b>Introduction</b> . . . . .	<b>11</b>
<b>2.2</b>	<b>Material properties</b> . . . . .	<b>12</b>
<b>2.3</b>	<b>Test details</b> . . . . .	<b>14</b>
2.3.1	Grip arrangement and specimen preparation. . . . .	14
2.3.2	Test method . . . . .	16
<b>2.4</b>	<b>Results and discussions</b> . . . . .	<b>18</b>
2.4.1	Test results . . . . .	18
2.4.2	Non-destructive inspection . . . . .	19
2.4.3	Fractured surface analyses . . . . .	21
<b>2.5</b>	<b>Conclusions</b> . . . . .	<b>26</b>
<b>2.6</b>	<b>Acknowledgements</b> . . . . .	<b>26</b>

---

### 2.1 Introduction

Reinforced concrete structures such as bridges are nowadays subjected to higher and more frequent traffic loads and thus they are more susceptible to fatigue damage. One of the key elements contributing to the bridge deck slab service life is the fatigue strength of steel reinforcement bars (rebars). Fatigue loading may lead to failure of rebars in the reinforced concrete without any sign of external structural distress except local concrete cracking.

Axial and bending tests of plain rebars and within concrete beams respectively are the two test methods commonly used to study the fatigue strength of rebars. Generally, fatigue tests on rebars are carried out as repetitive loading with stress ratio between 0 and 0.2 [1–3]. Axial fatigue tests on rebars are usually conducted on electromagnetic resonance machines at frequencies up to 150 Hz [4]. The disadvantage of these tests is related to the method of gripping the rebar. It tends to cause local stress concentration and premature failure of the rebar in the gripping area which are not characteristic of the rebar itself. Bending fatigue tests have the advantage of simulating the service conditions at the steel-concrete interface. However, concrete beams are usually tested by hydraulic machines at frequency smaller than 10 Hz, with few tests conducted for number of cycles more than  $10^7$ , due to the high costs [1].

Fatigue tests carried out up to the 1980's were mainly on hot rolled (HR) and cold worked (CW) rebars. However, HR and CW rebars were replaced in most European countries by quenched and self-tempered (QST) rebars [5, 6]. These rebars have a hard outer layer of martensite as a result of the specific QST treatment. This process known as Thermex or Tempcore has been introduced in Western Europe since 1974 [7].

Axial and bending fatigue tests performed on QST rebars have been reported in the literature. Thandavamoorthy [8] conducted fatigue tests with Tempcore rebars in eight concrete beams up to 2 million cycles; fatigue strength of QST rebars was found to be comparable to HR and CW rebars. In [3], Tempcore rebars survived to stress levels as high as 40% of the tensile strength  $\sigma_u$  and in some cases reached 60% up to 2 millions cycles. Surface imperfections and stress concentrations arising from the rib geometry were significant factors affecting the fatigue lifetime of the fractured rebars. Axial fatigue tests with Tempcore rebars were performed to a maximum of 5 million cycles [9]. The test results showed small scatter for rebars with different diameters. In [10], fatigue tests with HR, CW and Tempcore rebars were run to utmost 2 million cycles. Tempcore rebars showed considerably smaller scatter and higher fatigue strength than HR and CW rebars. In [11], concrete beams with embedded 12 mm diameter Thermex rebars were tested to utmost 10 million cycles. Rebars survived at stress levels higher than 40% of their yield strength  $\sigma_y$ .

Fatigue tests performed on QST rebars are mostly limited to utmost 5 million cycles. Thus, fatigue resistance of QST rebars based on these test data can lead to incoherent resistance estimation in the very high cycle regime [12] i.e., beyond 5 million cycles. This paper presents an experimental investigation carried out on QST rebars in the very high cycle fatigue regime. The gripping arrangement used in the axial fatigue tests are discussed. The test frequency is monitored for fatigue crack detection using liquid penetrant testing. The fractured surfaces are analysed by Scanning Electron Microscopy (SEM) and sites where fatigue cracks initiate are identified. Crack propagation region is estimated after test stopping.

## 2.2 Material properties

The chemical composition and mechanical properties of QST (Thermex) rebars with diameter of 16 mm were provided by the manufacturer and are summarised in Tables 2.1 and 2.2.

**Table 2.1** – Chemical composition of the QST rebar with diameter of 16 mm.

Elements	%
C	0.186
Si	0.22
Mn	0.86
P	0.023
S	0.040
Cr	0.14
Mo	0.02
Ni	0.13
Cu	0.40
Sn	0.018
V	0.002
Nb	0.002
Al	0.004
Ceq*	0.398

Notes:

$$(*) \text{ Ceq: Carbon Equivalent } \text{Ceq} (\%) = \text{C} (\%) + \frac{\text{Mn}}{6} (\%) + \frac{\text{Cr} + \text{Mo} + \text{V}}{5} (\%) + \frac{\text{Ni} + \text{Cu}}{15} (\%)$$

**Table 2.2** – Mechanical properties of the QST rebar with diameter of 16 mm.

$\sigma_y$ (MPa)		$\sigma_u$ (MPa)		$\epsilon_u$ (%)	
M	SD	M	SD	M	SD
518	8.29	613	1.63	16.7	1.40

Notes:

 $\sigma_y$ : yield strength; $\sigma_u$ : tensile strength; $\epsilon_u$ : strain at maximum force;

M: mean;

SD: standard deviation.

The microstructure consists of a hardened outer layer of martensite as indicated in Fig. 2.1 with a thickness of approximately 1.2 mm and a soft core of ferrite-pearlite. Vicker's hardness, measured in the cross section, varied from 265 HV in the martensitic layer to 160 HV in the core; these values are expected for QST rebars as given in [3,6].

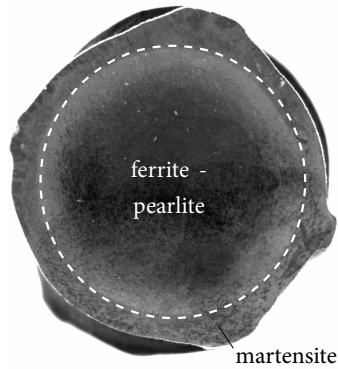


Figure 2.1 – Etched cross section of a 16 mm diameter QST rebar.

## 2.3 Test details

### 2.3.1 Grip arrangement and specimen preparation.

Axial fatigue tests are sensitive to the high stress concentration induced by the gripping pressure preventing the rebar from slipping. Some techniques were investigated to avoid premature failure of the rebar in the grip area.

The initial grip system used in the testing machine is shown in Fig. 2.2a. The grip has an inner-circular cross section of 20 mm. Three types of gripping arrangement were used with the initial system in order to obtain the failure in the rebar free length: 1) A 1 mm aluminium sheet was wrapped around the rebar ends within the grip area with the aim to distribute the force evenly over the surface of the rebar as shown in Fig. 2.2b; 2) Shot peening the rebar ends (see Fig. 2.2c) to induce compressive residual stresses on the surface and 3) Welding and machining the rebar ends to create a gradual and smooth transition between the grips and the ribbed surface Fig. 2.2d. The cross section diameter of the welded and machined rebar ends was 20 mm. However, all these methods were ineffective to prevent failure in the grip area.

Therefore, the initial grip system was replaced by a conical grip with maximum 18 mm diameter (see Figs. 2.3a and 2.3b) in the testing machine. Different conical

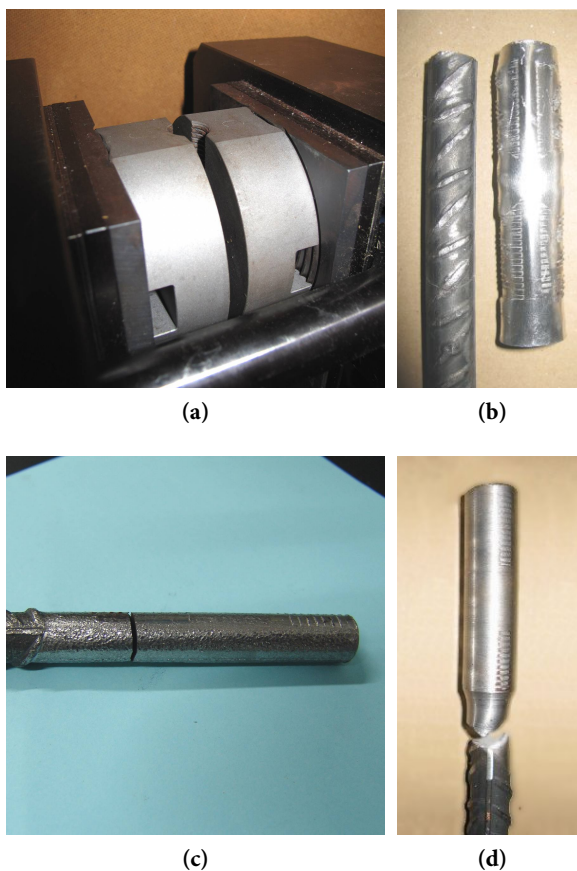


**Figure 2.2** – (a) Initial grip system used for the fatigue tests. Rebar failure in the grip area with (b) Aluminium sheet; (c) Shot peened rebar ends; (d) Welded and machined rebar.

arrangements have been shown to be effective for fatigue tests with rebars. However it required casting the rebar ends in alloys as given in [3,9]. In [7], QST rebar ends embedded in high strength metallic grout within a conical grip system showed 40% of the failures in the grips and 60% within a distance of 1 diameter outside the grip area.

In this work, three specimens were initially tested with the conical gripping system to verify its effectiveness. Failures occurred at least 39 mm away from the grip edges without modifying the rebar ends.

The specimen preparation was as follows: 16 mm raw material was first examined for defects, scratches and manufacturer's identification marks. Then it was cut into pieces of 400 mm length. 80 mm on each side were necessary for clamping; therefore the free length was 240 mm. The specimen free length considered in tests



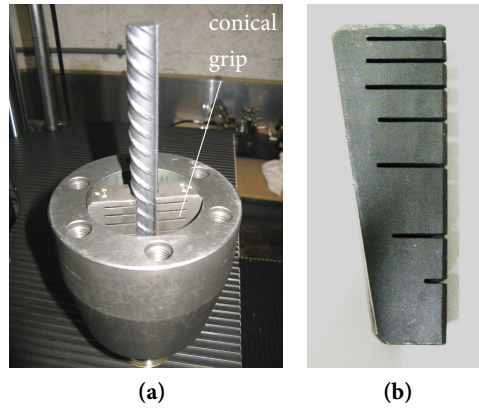


**Figure 2.3** – (a) Conical grip system used for the fatigue tests; (b) Detail of the conical grip.

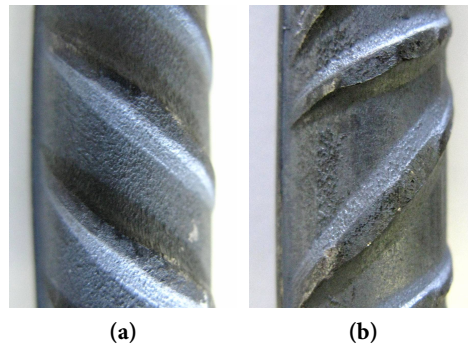


**Figure 2.4** – Rib patterns at both sides of the tested QST rebars.

is in accordance with standard recommended procedures [13] where the rebar's free length in axial tests should be at least 140 mm or 14 times the specimen diameter, whichever is greater. Care was taken to ensure that the free length was free of manufacturer's identification marks. The rib patterns on both rebar sides are shown in Figs. 2.4a and 2.4b.

### 2.3.2 Test method

Axial fatigue tests were performed on a RUMUL Testonic 100 kN 8601 resonance machine at 85 Hz and force-ratio of 0.1. A total of 21 specimens were tested; 6 tested specimens were considered as non-valid results since the failure occurred in the grip area. The valid tests i.e, rebars with failure in the free length were run to at least  $1.89 \times 10^6$  cycles but not longer than  $66.2 \times 10^6$  cycles as given in Table 2.3. The failure within the rebar's free length occurred in more than 70% of the tested

rebars. Whenever the specimen survived the test, it was termed "run-out". Two run-outs were retested under higher forces. It was assumed fatigue damage in the tested rebars for a surface crack length of at least 5 mm. This is the minimum crack length that can be detected by the non-destructive inspection technique used in this work.

During all the tests that were carried out, the resonance frequency was monitored. The frequency change was used as an indication of cracking in the specimen. A typical evolution of the frequency drop obtained during the fatigue tests is shown in Fig. 2.5. The frequency drop versus number of cycles can be separated in three stages. In stage I, the frequency drops continuously from the beginning of the tests up to approximately  $10^6$  cycles. The frequency drop in the beginning of the test was probably caused by the settlement of the specimen in the clamping area. A stabilization of the frequency is observed at stage II with the frequency variation being smaller than 0.1%. An abrupt frequency change occurs at stage III caused by fatigue crack propagation followed by failure of the specimen.

The test was interrupted just after the abrupt frequency change for non-destructive inspection by liquid penetrant for detection of fatigue cracks. The specimen remained mounted in the machine and loaded at the mean force while the liquid penetrant was applied on the surface. The liquid penetrant was applied only once. The test was stopped at a frequency drop of approximately 2.2%.

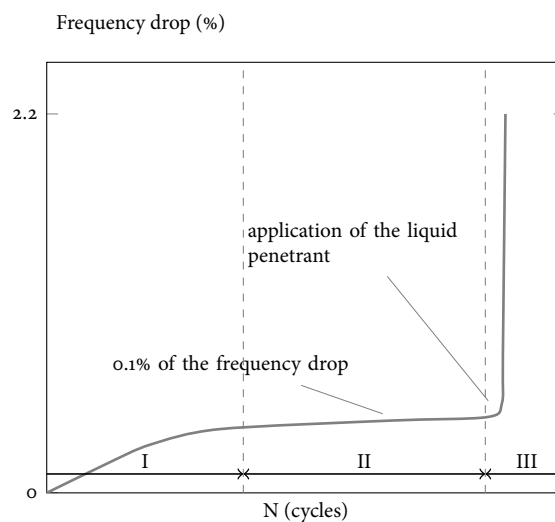


**Figure 2.5** – Representative frequency drop (%) of a failed specimen during the fatigue test.

**Table 2.3** – Fatigue test results of 16 mm rebar.

Specimen number	Stress range (MPa)	Number of cycles ( $\times 10^6$ )	Failure x Run-out o	Failure location <sup>(1)</sup> (mm)
1	225	30	o	-
2	235	30	o	-
3	235	35	o	-
4	243	36	o	-
5	243	51	o	-
6	243	49	o	-
7	245	1.89	x	92
8	247	30	o	-
9	247	30	o	-
10	247	30	o	-
11 <sup>(2)</sup>	251	64.5	o	-
12	251	66.2	o	-
13 <sup>(2)</sup>	255	34.6	o	-
14	255	2.71	x	60
15	255	1.97	x	39

Notes:

<sup>(1)</sup> Failure location: distance from the grip's edge to the failure in the free length.

<sup>(2)</sup> Specimens 11 and 13 correspond to the retested 8 and 9 specimens at 251 MPa and 255 MPa respectively.

## 2.4 Results and discussions

### 2.4.1 Test results

Table 2.3 shows the fatigue test results of the 16 mm rebars. Two specimens were retested at higher stresses after run-outs. Three rebars showed a failure and all the others were run-outs. The failure location on the rebars are given in Table 2.3. Run-outs represented 80% of the test results with one rebar surviving to a total of  $94.5 \times 10^6$  cycles for a stress level of approximately 48% of the mean yield strength  $\sigma_y$ .

Fatigue strength of rebars are traditionally expressed by S-N curves. S-N curves are obtained by linear regression applied only to failed data points; run-outs are neglected in the analysis. In the standard S-N curves, a minimum of 12 specimens is required for characteristic allowable and reliability data as given in [14]. The 3 failed specimens in this present work don't fit the minimum specimen size requirements for linear regression analysis. Therefore, the S-N curve for the present test results couldn't be determined. In [12], an alternative approach is proposed for statistical treatment of the data including run-out specimens.

### 2.4.2 Non-destructive inspection

Non-destructive inspection allowed identifying the fatigue crack location and size on the surface of the failed specimens. The liquid penetrant was applied at the beginning of stage III as indicated in Fig. 2.5.

The frequency change measured from the beginning of stage I until application of the liquid penetrant on the 3 failed specimens varied between 0.15 and 0.18%. Fig. 2.6 shows the frequency evolution obtained for the failed specimens 7, 14 and 15. Two dots of penetrant ink shown in Fig. 2.7a indicated the surface crack tips detected just after the abrupt frequency change in specimen 15. The distance between the crack tips was approximately 8 mm. Similar crack length was also detected on the surface of specimens 7 and 14. The crack propagated away from the non-uniform ribs and perpendicular to the longitudinal specimen axis. Fig. 2.7b shows the crack after the test stopping when the frequency dropped by 2.2%. The crack area was approximately 50% of the specimen cross section.

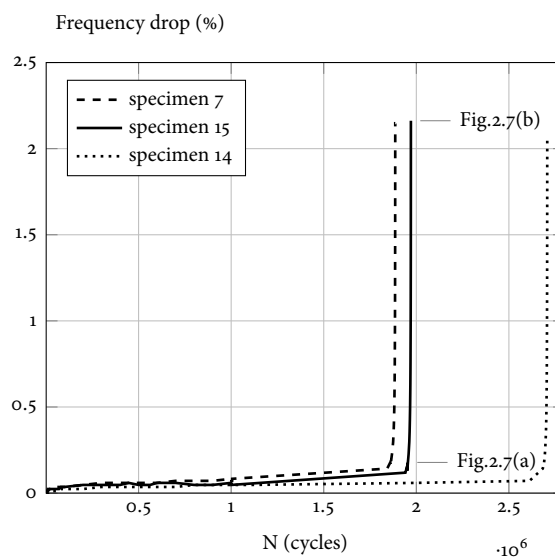


**Figure 2.6** – Frequency drop versus number of cycles obtained for specimens 7, 14 & 15.

The frequency drop versus number of cycles obtained for run-out specimens is given in Figs. 2.8 to 2.11. The frequency evolution of run-out specimens showed a similar tendency for stages I and II: A continuous frequency drop followed by an stabilization period until test stopping. The liquid penetrant was applied on the run-outs mounted in the machine at the end of the tests. However, no crack was detected

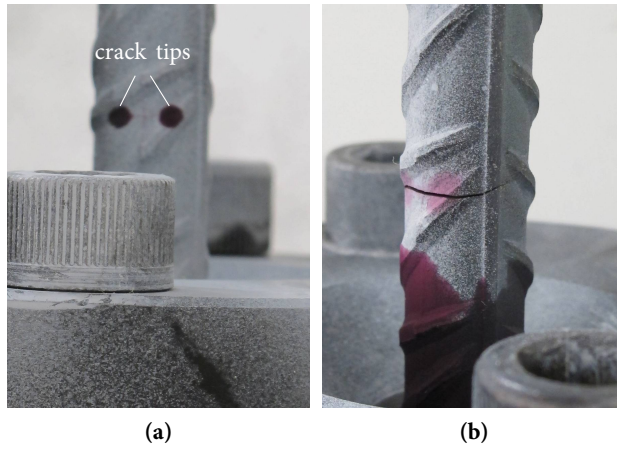


**Figure 2.7** – (a) Specimen 15: Two dots of penetrant ink indicating the fatigue crack tips on the specimen surface; (b) Crack on the specimen surface when the test was stopped.

on the surface of any surviving specimen, even for specimen 13 which showed a frequency drop of nearly 0.5%.

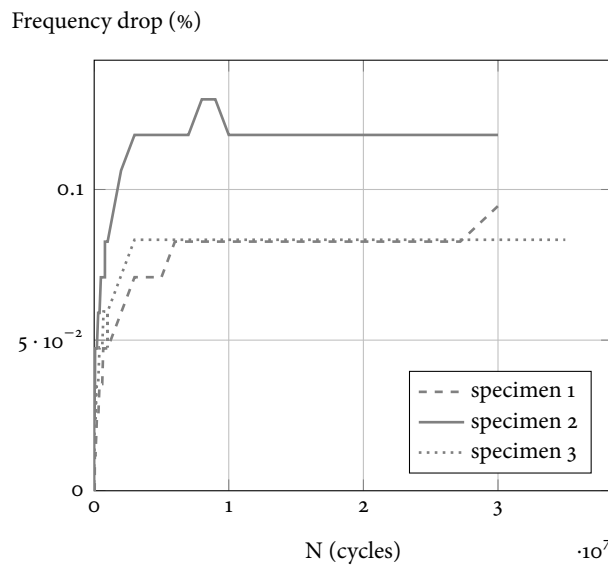


**Figure 2.8** – Frequency drop versus number of cycles obtained for specimens 1, 2 & 3.

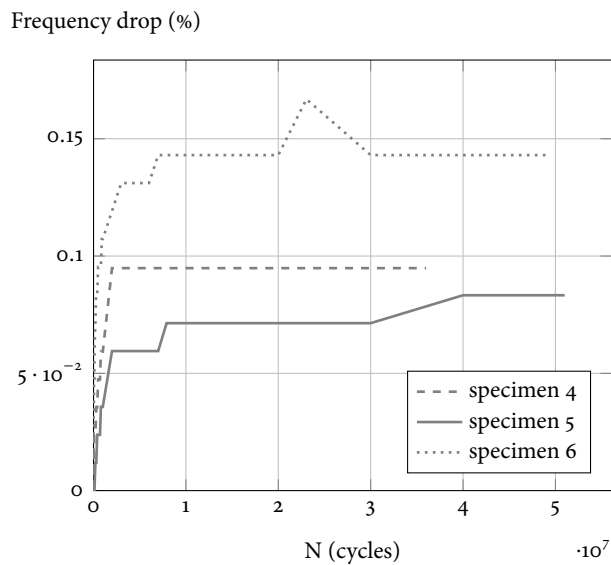


**Figure 2.9** – Frequency drop versus number of cycles obtained for specimens 4, 5 & 6.

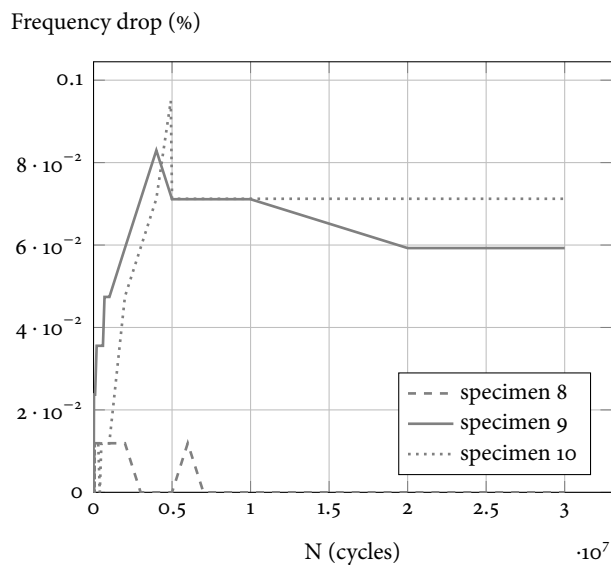


**Figure 2.10** – Frequency drop versus number of cycles obtained for specimens 8, 9 & 10.

### 2.4.3 Fractured surface analyses

Fractography analysis was performed by Optical Microscopy (OM) and XL30-FEG SEM in order to determine the location where fatigue cracks initiate. Since the tests were stopped before complete fracture of the specimens, it was required to split them and prepare the fractured surfaces before microscopic analysis. After test stopping,

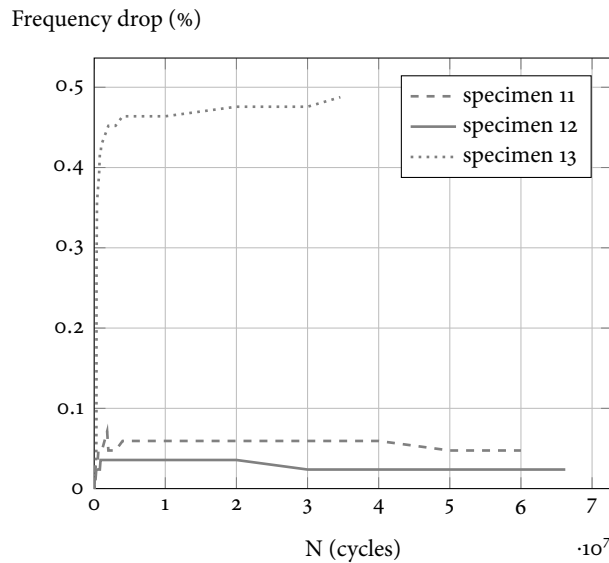


**Figure 2.11** – Frequency drop versus number of cycles obtained for specimens 11, 12 & 13.

the specimen was put in liquid nitrogen in order to split them in a brittle manner using an actuator. The average temperature measured on the specimen surfaces was approximately  $-65^{\circ}\text{C}$  after 30 min immersed in liquid nitrogen. QST rebars tends to have a brittle fracture at this temperature [15]. The frozen specimen surfaces were dried using ethanol and compressed air and then left in desiccator under vacuum for one day. The fractured surfaces were then immersed in a beaker containing melted paraffin at  $55^{\circ}\text{C}$  to protect them from damage. A cut was made at approximately 5 cm away from the fractured surfaces by Electric Discharge Machining.

The paraffin around the specimen's cross section was manually removed. The cross sections were then immersed in an ultrasonic cleaner containing Xylene for 10 minutes in order to remove the residual paraffin. Since some corrosion was visible on the fractured surfaces, two methods of removing corrosion were used: 1) One side of the cross section was immersed in a beaker with Alconox solution heated up to  $90^{\circ}\text{C}$  for 1 hour and 2) The other side was immersed in an ultrasonic cleaner for 10s containing an acid solution, consisting of 3 mL of hydrochloric acid, 4 mL of 2-butyne-1, 4-diol (35% aqueous solution) and 50 mL of deionized water [16]. Both methods were effective to remove the corrosion on the surface. After corrosion removal, the fractured surfaces were cleaned with ethanol, dried with compressed air and left in desiccator under vacuum to protect it from any damage before microscopic analysis.

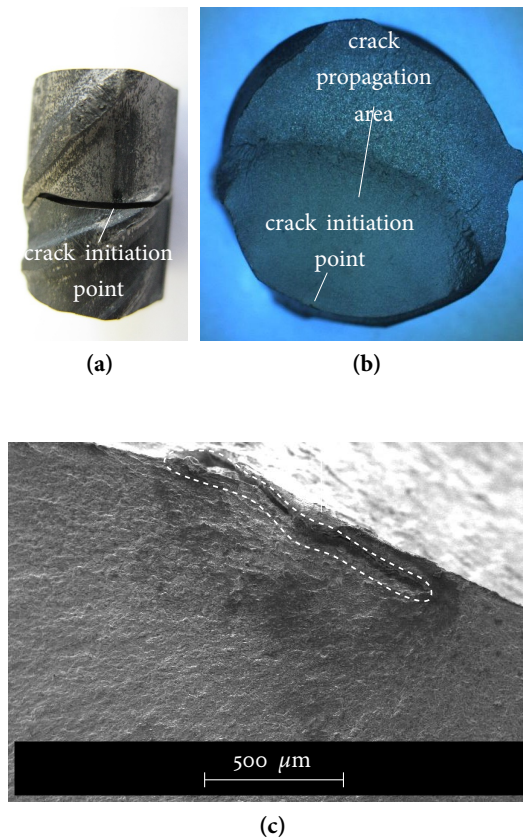


**Figure 2.12** – (a) Location where fatigue crack initiates on the surface of specimen 7; (b) OM image (10×) of the fractured cross section; (c) SEM image (65×) of the imperfection from where fatigue crack initiated.

The site from where fatigue cracks initiate on the specimen surface is indicated in Figs. 2.12a, 2.13a and 2.14a. The crack initiated at or very near the base of the transverse non-uniform ribs. Figs. 2.12b, 2.13b and 2.14b show the fatigue crack propagation region determined from fractography images obtained with OM. The bright rough area is the brittle fracture caused by the actuator whereas the smooth area is the fatigue crack region. The different surface texture allows determining the final fatigue crack area.

Imperfections on the fractured cross section from where fatigue cracks initiated are indicated in Figs. 2.12c, 2.13c and 2.14c. The cracks (white lines in the SEM images) emerging from the imperfections confirm the crack initiation site previously identified in the OM images. A single fatigue crack initiation site is identified on the cross sections of specimens 7 and 14: Cracks start to propagate from a imper-



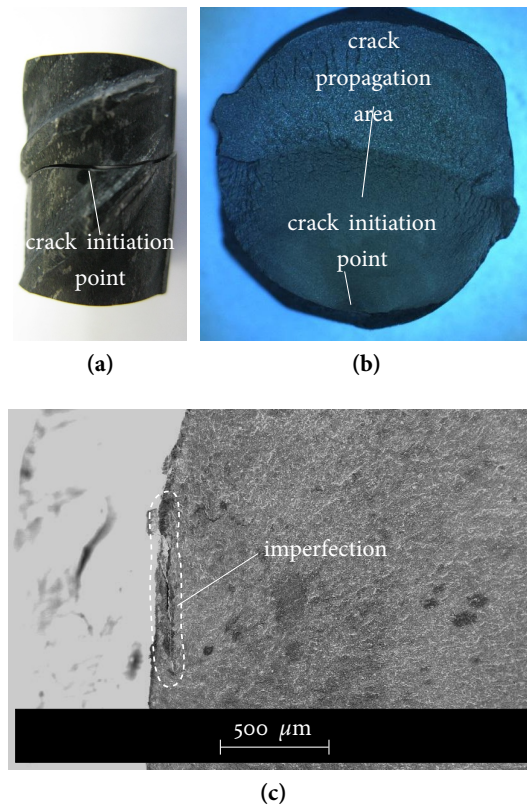


**Figure 2.13** – (a) Location where fatigue crack initiates on the surface of specimen 14; (b) OM image (10 $\times$ ) of the fractured cross section; (c) SEM image (65 $\times$ ) of the imperfection from where fatigue crack initiated.

fection size of approximately 1 mm and 0.8 mm in specimens 7 and 14 respectively as indicated in Fig. 2.12c and 2.13c. In specimen 15, fatigue cracks initiated from two imperfections on the cross section of approximately 0.3 mm and 0.45 mm as shown in Fig. 2.14c. Imperfections identified on the QST cross sections are originated from the manufacturing process.

Fractured surface analyses on HR, CW and QST rebars tested at high number of fatigue cycles have been reported in the literature [3, 4, 17]. According to [4], fatigue lifetime of HR and CW rebars axially tested at high number of cycles was mainly affected by surface defects ranging from 5 to 100  $\mu\text{m}$ . HR rebars mostly had a single fatigue crack initiation site and plane fractured surface. CW rebars had multiple initiation sites and helical fractured surfaces.

In [3], fatigue cracks on QST rebars initiated from surface defects and at the root of the transverse ribs from where arise the highest stress concentration [18].

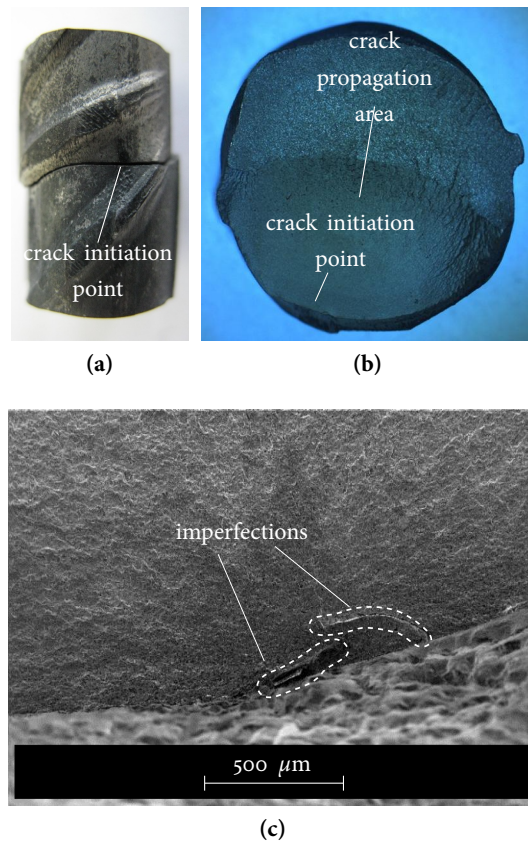


**Figure 2.14** – (a) Location where fatigue crack initiates on the surface of specimen 15; (b) OM image (10×) of the fractured cross section; (c) SEM image (65×) of the imperfections from where fatigue crack initiated.

The plane fractured surface showed single or multiple initiation sites: Higher stress range and lower ratio between rib radius and rib height  $r/h$  led to multiple initiation sites.

In [17], fatigue tests performed on HR rebars embedded in concrete beams resulted in fatigue cracks starting at the base of transverse ribs and plane fractured surface. The fractured surface of CW rebars embedded in concrete was plane inclined at an angle of approximately  $45^\circ$  and fatigue cracks initiated near to the transversal ribs.

Comparisons between the fractured surface investigations given in the literature [3,4,17] and the fractured surfaces analysed in this present work showed that fatigue life of HR, CW and QST was significantly affected by surface imperfections in axial fatigue tests at high cycle regime. In bending fatigue tests, the rib geometry had a

significant effect on the fatigue lifetime of rebars. Beside, HR and QST rebars tested at high cycle fatigue tended to have a single crack initiation site and a similar plane fractured surface while CW rebars show a helical fractured surface.

## 2.5 Conclusions

Fatigue tests were performed on QST rebars between  $10^6$  and  $10^8$  cycles and under constant amplitude loading. Non-destructive inspection using liquid penetrant allowed to determine the surface crack size and location just after the abrupt drop of the frequency. Fractured surfaces were analysed after test stopping by OM and SEM and compared to fractographic analysis from the literature. The following conclusions can be drawn from the present study:

- Conical grip arrangement was the only effective method to prevent failure in the grip area. The method provided more than 70% of the failures on rebar free length without requiring any modification at the rebar ends.
- QST rebars survived at least 30 million cycles in 80% of the tests and at stress levels of approximately 50% of the mean yield strength.
- Due to the small frequency change at almost the entire fatigue life of the rebars and the limitation of the penetrant liquid testing in detect surface cracks from few mm, fatigue cracks could only be detected when the rebar approached fracture.
- The fatigue lifetime of QST rebars was significantly controlled by manufacturing imperfections extending from surface to the depth cross section; fatigue cracks initiated from imperfections located at and very near the base of the transversal ribs.

## 2.6 Acknowledgements

The authors are grateful to Danièle Laub from the Interdisciplinary Centre For Electron Microscopy (CIME) at EPFL for her advices and help with the sample preparation for the microscopic analyses. We are also grateful to Prof. Francesco Stellacci from the Supramolecular Nanomaterials and Interfaces Laboratory (SuNMIL) who provided the laboratory space for the chemical attack and preparation of the samples.

---

## *Bibliography*

---

- [1] Tilly, G. P. (1979). Fatigue of steel reinforcement bars in concrete: A review. *Fatigue & Fracture of Engineering Materials & Structures*, 2(3), 251-268.
- [2] Tilly, G. P. (1984). Fatigue testing and performance of steel reinforcement bars. *Matériaux et Construction*, 17(1), 43-49.
- [3] Zheng, H., & Abel, A. A. (1999). Fatigue properties of reinforcing steel produced by Tempcore process. *Journal of Materials in Civil Engineering*, 11(2), 158-165.
- [4] Mallett, G. P. (1991). Fatigue of reinforced concrete. Transport and Road Research laboratory, HMSO, London.
- [5] Economopoulos, M., Respen, Y., Lessel, G. & Steffes, G. (1975). Application of the Tempcore process to the fabrication of high yield strength concrete-reinforcing bars. *Metallurgical reports CRM*, (45), 3-19.
- [6] Rehm, G., & Russwurm, D. (1977). Assessment of concrete reinforcing bars made by the Tempcore process. *Metallurgical reports CRM*, (51), 3-16.
- [7] Virmani, Y. P., Wright, W., & Nelson, R. N. (1991). Fatigue testing for Thermex reinforcing bars. *Public Roads*, 55(3), 72-78.
- [8] Thandavamoorthy, T. S. (1999). Static and fatigue of high-ductility bars reinforced concrete beams. *Journal of Materials in Civil Engineering*, 11(1), 41-50.
- [9] Donnell, M. J., Spencer, W., & Abel, A. (1986). Fatigue of Tempcore reinforcing bars - the effect of galvanizing. In *Australasian Conference on the Mechanics of Structures and Materials*, 10th, 1986, Adelaide, Australia (Volume 2).

- [10] Fehlmann P. (2012). Zur Ermüdung von Stahlbetonbrücken. ETH thesis, n° 20231, Zürich.
- [11] Schläfli M. (1999). Ermüdung von Brückenfahrbahnplatten aus Stahlbeton. EPFL thesis n° 1998, Lausanne.
- [12] D'Angelo, L., Rocha, M., Nussbaumer, A. & Brühwiler, E. (2014). S-N-P fatigue curves using Maximum Likelihood: Method for fatigue resistance curves with application to straight and welded rebars. EUROSTEEL, Naples, Italy.
- [13] EN ISO 15630-1. (2010). Steel for the reinforcement and prestressing of concrete-test methods - part 1: Reinforcing bars, wire rod and wire.
- [14] ASTM E739-10. (2010). Standard practice for statistical analysis of linear or linearized stress-life (S-N) and strain-life ( $\epsilon$ -N) fatigue data.
- [15] Nikolaou, J., & Papadimitriou, G. D. (2005). Impact toughness of reinforcing steels produced by (i) the Tempcore process and (ii) microalloying with vanadium. *International journal of Impact Engineering*, 31(8), 1065-1080.
- [16] ASM Handbook: Fractography (1992). ASM International.
- [17] Hanson, J. M., Burton, K. T., & Hognestad, E. (1968). Fatigue tests of reinforcing bars-effect of deformation pattern. *Journal of the PCA Research and Development Laboratories*, 10, 2-13.
- [18] Zheng, H., & Abel, A. (1998). Stress concentration and fatigue of profiled reinforcing steels. *International Journal of Fatigue*, 20(10), 767-773.

## Material and geometrical characterisation of quenched and self-tempered steel reinforcement bars

— Marina Rocha, Eugen Brühwiler, Alain Nussbaumer

**Abstract:** *Quenched and self-tempered (QST) steel reinforcement bar (rebar) is manufactured by Thermex or Tempcore process. Characterisation studies of QST rebars are mostly limited to reveal the hardened outer layer and some improved mechanical properties compared to hot rolled (HR) and cold worked (CW) rebars. However, investigations on residual stresses and imperfections originated from the manufacturing process as well as stress concentrations arising from the ribbed profile are rarely found in the literature. Surface residual stress may be beneficial or detrimental to the fatigue performance of rebars although they have been studied only on the subsurface of QST rebars. Surface imperfections are zones of stress concentration from where fatigue cracks may initiate. Imperfections are usually identified in the fractured cross section resultant from fatigue tests of re-*

*bars. Stress concentrations can also arise from the rib geometry. While the rib geometric parameters affect the stress concentration factor  $K_t$  on rebars, stress concentration analysis are restricted to 2D Finite Element Models (FEM)s. In this present work, characterisation analyses of QST rebars include: 1) Experimental investigation of surface and subsurface residual stresses on QST rebars by Cut Compliance and X-ray diffraction techniques. Residual stresses from both techniques are discussed. 2) Identification of surface imperfections by Scanning Electron Microscopy (SEM) analysis. 3) 3D Finite Element Analysis of stress concentrations on the ribbed profile. The influence of the rib geometry such as radius, width, height and inclination as well as the rebar diameter on  $K_t$  values are analysed. The critical zones are determined along the ribs.*

**Keywords:** Quenched and self-tempered rebars; Microstructure; Residual stress; Surface imperfection; Stress concentration factors.



## Contents

<b>3.1</b>	<b>Introduction</b> . . . . .	<b>31</b>
<b>3.2</b>	<b>Material characteristics</b> . . . . .	<b>32</b>
<b>3.3</b>	<b>Fabrication process</b> . . . . .	<b>33</b>
<b>3.4</b>	<b>Microstructure</b> . . . . .	<b>34</b>
3.4.1	Metallographic analysis . . . . .	34
3.4.2	Grain size and area fraction . . . . .	35
3.4.3	Microhardness test . . . . .	36
<b>3.5</b>	<b>Residual stresses</b> . . . . .	<b>37</b>
3.5.1	Residual stress on QST rebars . . . . .	37
3.5.2	Cut Compliance technique . . . . .	38
3.5.3	X-ray diffraction technique . . . . .	41
3.5.4	Results and discussion . . . . .	43
<b>3.6</b>	<b>Surface imperfections</b> . . . . .	<b>44</b>
<b>3.7</b>	<b>Stress concentration</b> . . . . .	<b>46</b>
3.7.1	Stress concentration on the ribbed profile . . . . .	46
3.7.2	Numerical analysis . . . . .	46
3.7.3	$K_t$ determined on the rib . . . . .	50
<b>3.8</b>	<b>Conclusions</b> . . . . .	<b>56</b>
<b>3.9</b>	<b>Acknowledgements</b> . . . . .	<b>57</b>

### 3.1 Introduction

Concrete structures show typically three types of steel reinforcement bars (rebars): hot rolled (HR), cold worked (CW) and quenched and self-tempered (QST) steels. HR rebars are produced through hot rolling followed by a slow cooling. Billets heated up to about 1200°C pass through rollers which squeeze them into the required diameter. The bars are then air cooled to ambient temperatures after emerge from the last rolling mill with a temperature of about 1000°C. As the rolling finish is above 900°C before the steel is allowed to naturally cool, the resulting properties are similar to those obtained by normalisation process [1]. CW rebars are submitted to strain hardening after hot rolling; cold twisted deformed rebars are produced by stretching and twisting of mild steel, beyond the elastic limit and subsequently releasing of the load [2].



HR and CW rebars were replaced by QST rebars in some European countries [3–5] i.e., hot rolled steels followed by a special thermal treatment. This thermal process known as Thermex is similar to the Tempcore process developed in 1974 [6]. QST rebars show advantages with respect to weldability, bendability and ductility compared to HR and CW rebars [4, 5, 7, 8].

Thermex process combines the conventional hot rolling with rapid water quenching which results in a hardened outer layer of martensite; HR and CW rebars show ductile ferritic-pearlitic microstructure [9]. The biggest temperature gradients are produced in the quenching stage and hence the greatest residual stresses. As freshly quenched steel tend to crack, the tempering process starts just after quenching to minimize distortion, cracking and residual stresses [10].

The residual stresses pattern in QST steels are mainly influenced by the combination of thermal and microstructural changes in the cross section during the fabrication process [10]. Residual stresses on rebars act in addition to the stresses due to service loading. Tensile residual stresses are detrimental while compressive stresses are beneficial to the rebar performance. In [11], residual stresses on QST rebars were experimentally determined by hole drilling method; compressive residual stresses were found to improve their fatigue strength. In this present study, residual stresses are determined on surface and subsurface of QST rebars by Cut Compliance and X-ray diffraction techniques. Results obtained from both techniques are discussed.

The ribs introduced in the rolling mill as well as the surface imperfections originated from the manufacturing process are zones of stress concentration. The inhomogeneous stress distribution at the ribbed profile and imperfections may initiate a failure and it should be mitigated or if possible avoided.

In this present work, Scanning Electron Microscopy (SEM) analyses were performed on the surface of QST rebars to detect imperfections near the ribs. Similar studies have not been reported in the literature. Moreover, a parametric study was developed to analyse the influence of the rib geometry, including rib inclination, and rebar diameter on the stress concentration factors  $K_t$ .  $K_t$  values were determined along the ribs by 3D Finite Element Analyses (FEA)s.

### 3.2 Material characteristics

The chemical composition of QST rebars analysed in this work, with diameters of 16, 26 and 34 mm, is given in Table 3.1. QST rebar is a low alloy carbon steel since it contains a Carbon content  $C < 0.3\%$  and Cu content which can exceed the maximum

**Table 3.1** – Chemical composition of the QST rebars with diameters of 16, 26 and 34 mm.

Elements <sup>1</sup>	Sample diameter (mm)			
	%	16	26	34
Carbon C		0.186	0.185	0.198
Silicon Si		0.22	0.20	0.24
Manganese Mn		0.86	0.74	0.97
Chromium Cr		0.14	0.18	0.10
Nickel Ni		0.13	0.13	0.14
Copper Cu		0.40	0.38	0.48
Ceq <sup>2</sup>		0.397	0.383	0.423

<sup>(1)</sup> It includes only elements with content equal or greater than 0.1%.

<sup>(2)</sup> Ceq: Carbon Equivalent

$$\text{Ceq} (\%) = \text{C} (\%) + \frac{\text{Mn}}{6} (\%) + \frac{\text{Cr} + \text{Mo} + \text{V}}{5} (\%) + \frac{\text{Ni} + \text{Cu}}{15} (\%)$$

**Table 3.2** – Mechanical properties of QST rebars.

$\sigma_y$	$\sigma_u / \sigma_y$	$\epsilon_u$
MPa	MPa	%
>500	>1.15	>7.5
<600	<1.25	

Notes:

$\sigma_y$ : yield strength;

$\sigma_u$ : tensile strength;

$\epsilon_u$ : strain at maximum force.

of 0.40% [12]. Mechanical properties are given in Table 3.2.

### 3.3 Fabrication process

QST rebars analysed in this work were produced by the Thermex process. Billets with cross section of 170 × 130 mm and length of 12.5 m are reheated up in furnaces at about 1200-1300°C. These billets pass through the rollers which squeeze them into the required diameter. After pass by the first rolling the temperature of the bars is between 1140-1180°C. The end rolling temperature is approximately 1050°C. The ribs are introduced on the surface of the bars at the last rolling. The rebars are then slitted in two strands.

Hot rolled steels are then quenched with water in tubes providing intensive cooling of the surface. The rapid quenching leads to the formation of martensite at the

surface layer and a hot core which remains austenitic. The martensite start temperature  $M_s$ , i.e., the temperature at which the transformation of austenite to martensite begins, can be estimated by Eq. 3.1 [13]:

$$M_s(^{\circ}) = 539 - 423 \cdot (\%C) - 30.4 \cdot (\%Mn) - 17.7 \cdot (\%Ni) - 12.1 \cdot (\%Cr) - 7.5 \cdot (\%Mo) \quad (3.1)$$

where  $M_s$  is approximately 430°C for QST rebars.

When the rebar emerges from the quenching zone, the thermal gradient across the rebar section causes heat to flow from the core toward the surface. This results in a tempered martensitic surface and an equalization of both surface and core temperatures at approximately 670°C [14]. During atmospheric cooling of the rolled bar on the cooling bed, the austenitic core is gradually transformed to a ferrite-pearlite microstructure.

## 3.4 Microstructure

### 3.4.1 Metallographic analysis

The microstructure of QST rebars was revealed by metallography analysis. Transversal and longitudinal sections were cut with Electrical Discharge Machining (EDM) and polished with abrasive papers and diamond paste [15] up to 0.25  $\mu\text{m}$ . The surfaces were then polished on cloth synthetic suede with alumina up to 0.05  $\mu\text{m}$  for 60 seconds. After polishing, the sections were etched with a fresh solution of Marshall's reagent [16] for 4 seconds. The sections were completely immersed in this solution where an effervescent etching reaction was observed. The etched surfaces were then rinsed with ethanol, dried with compressed air and analysed under an Optical Microscopy (OM).

Fig. 3.1a shows the transverse etched section of the QST rebar with 16 mm diameter. Fig. 3.1b consists of tempered martensite (TM) within prior austenite grains. Transition zone (TZ) with acicular ferrite and pearlite is shown in Fig. 3.1c and core with quasi-equiaxed ferrite and pearlite (F-P) is given in Fig. 3.1d. The longitudinal section showed similar grain shape to the microstructure of the transversal section in the three TM, TZ and F-P zones.

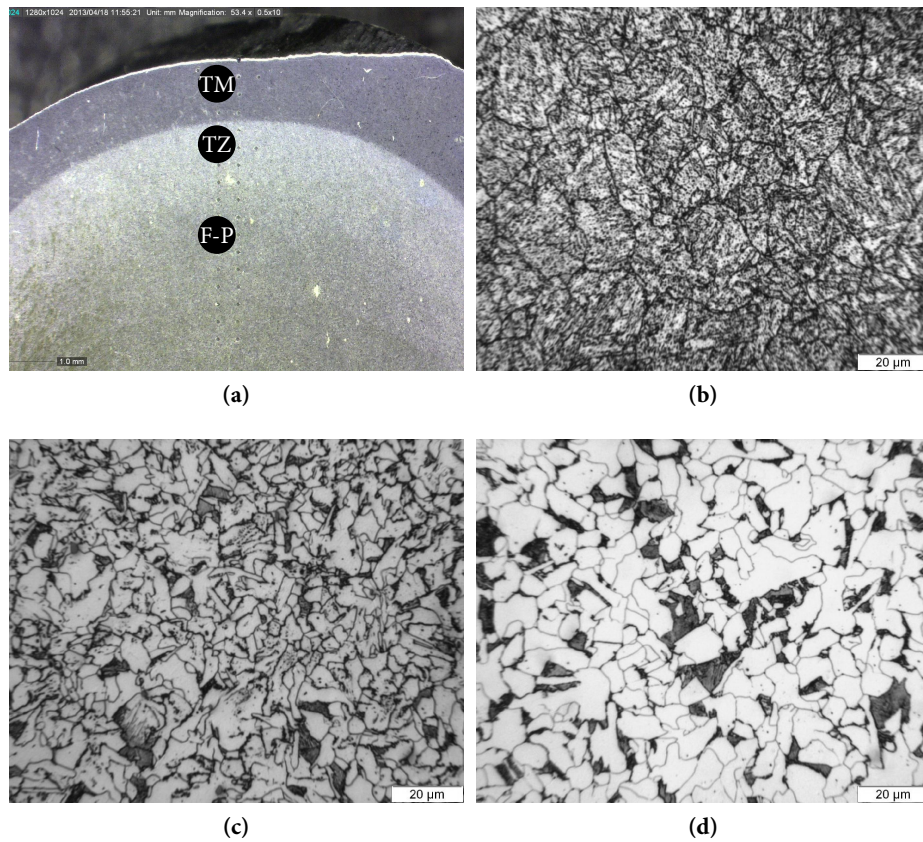


**Figure 3.1** – (a) Etched cross section of the QST rebar; (b) Tempered martensite (TM); (c) Transition zone (TZ) of acicular ferrite (light areas) and pearlite (darker areas); (d) Quasi-equiaxed ferrite (light areas) and pearlite (dark areas) (F-P).

### 3.4.2 Grain size and area fraction

The Abram's Three Circle method [17] was used to estimate the ferrite average grain size in the core of QST rebars. Cross sections with diameter of 16, 26 and 34 mm were analysed by OM. The area fraction of pearlite was also estimated according to the procedures given in [18].

The images of the microstructure were taken on the core centre. The average grain size of ferrite and area fraction of pearlite are given in Table 3.3.

The microstructure of the QST rebars became coarser with the increase of the diameter. Similar behaviour was observed by [19] for Tempcore rebars with diameter ranging from 10 to 16 mm.

HR and CW rebars show low ( $C \leq 0.3\%$ ) or medium Carbon content ( $0.3\% < C < 0.6\%$ ) [20, 21]. The microstructure in the entire cross section consists of du-

**Table 3.3** – Average grain size of ferrite and area fraction of pearlite obtained in the core of QST rebars.

Cross section mm	Ferrite ASTM number [17]	95% CI*	Pearlite %	95% CI*
16	11 (7.9 $\mu\text{m}$ )	0.20	11	3.33
26	10.5 (9.4 $\mu\text{m}$ )	0.19	13	2.04
34	10 (11.2 $\mu\text{m}$ )	0.30	25	4.62

(\*) Confidence interval determined according to the procedures given in [17,18].

plex ferrite-pearlite [3, 9]. HR rebars can show coarser microstructure in the core compared to QST rebars with similar or greater diameter. In [9], HR rebars with 12 mm diameter showed an average ferrite grain size of 43  $\mu\text{m}$  which is higher than the values given in Table 3.3. In [22], the average grain size of approximately 25  $\mu\text{m}$  was determined in the centre of HR rebars with diameter of 25 mm.

### 3.4.3 Microhardness test

Hardness may be related to the tensile strength of the steels and it is helpful to determine if the steel has been heat treated in accordance to a specification [10].

Vickers hardness testing was conducted on the QST cross sections with diameters of 16, 26 and 34 mm according to [23]. A hardness map was obtained in the three zones i.e., rim, intermediate and core as given in Fig. 3.1a. A 1 kg-force was applied for 12-15 seconds on the cross sections. The minimum distance of 2.5 t (t is the indenter diagonal) between indentations was respected to ensure that a measurement was not affected by the previous one. This distance was approximately 0.35 mm. The hardness maps are graphically shown in Fig. 3.2.

The minimum and maximum hardness values measured in the rim of the three cross sections were approximately 263 and 285 HV respectively. Similar hardness values can be found in [24] for Tempcore rebars. The hardness decreased continuously from the transition zone to the core where a small variation of the hardness values was measured. As it was expected, the hardness of QST cross sections decreased as the distance from the rim increased.

The core of the cross section with 34 mm showed considerable higher values of hardness compared to both 16 and 26 mm cross sections as shown in Fig. 3.2. This may be explained by the higher amount of pearlite determined in the core of the 34 mm diameter; the hardness increases with increasing pearlite content [25].

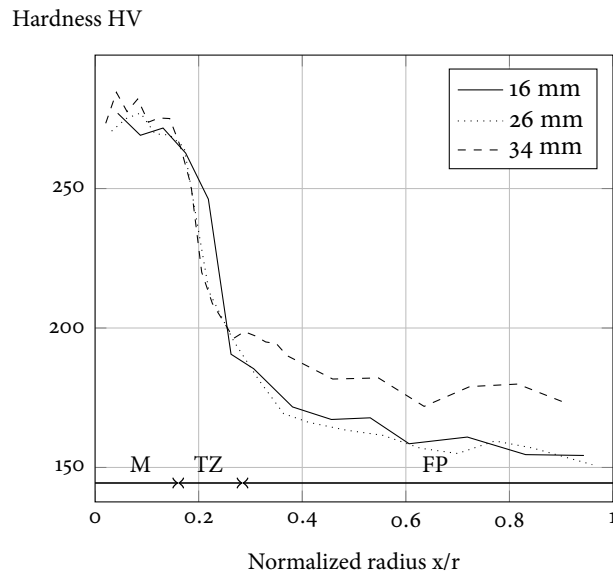


**Figure 3.2** – Hardness map of the QST rebars with diameters of 16, 26 and 34 mm.

CW and HR rebars show an entire cross section of ferrite-pearlite and homogeneous hardness. For HR rebars, the hardness can vary between 160 and 290 HV depending on the steel grade [26, 27].

## 3.5 Residual stresses

### 3.5.1 Residual stress on QST rebars

Residual stresses are those which remain in the material with no external applied force. These stresses are in self-equilibrium and consequently the resultant force produced by residual stresses must be zero.

Residual stress pattern on QST rebars result from combination of thermal and microstructural changes in the manufacturing process. The formation of martensite from austenite in the quenching process results in volume expansion at the surface whereas the remainder part is still austenitic. When the remainder austenite transforms to martensite, its volumetric expansion is restricted by the hardened surface layer. This restrain results in tensile residual stress at the surface and compressive residual stress in the interior [10]. At the same time, the interior contraction in the final cooling process is inhibited by the martensitic layer. This restrain generates tensile residual stress in the interior and compressive residual stress at the surface [10]. The tempering process starts just after quenching to minimize these

residual stresses.

Residual stress pattern of rebars are hardly found in the literature. Residual stress acts as a preloading when the rebar is subjected to fatigue loading and it can affect its fatigue strength: compressive residual stresses determined on Tempcore rebars were found to improve their fatigue strength [11] at  $R=0$ .

In this work, residual stresses at and near the surface of QST rebars were determined by Cut Compliance (CC) [28] and X-ray diffraction [29, 30] techniques. Since the X-ray diffraction technique is limited to a maximum depth of about  $5 \mu\text{m}$  from the surface of steels, it requires a layer removal at greater depth due to the low levels of penetration of approximately Angstrom wavelength X-ray beams [30].

As-received QST rebars used for residual stress analyses were slightly distorted. This may affect the results obtained from both CC and X-ray diffraction techniques.

### 3.5.2 Cut Compliance technique

CC (also called Crack Compliance) is a destructive technique to determine residual stresses from the material subsurface [28]. A cut is progressively introduced in the specimen using EDM. Strain gauges are glued on the specimen surface and near the cut (see Fig. 3.3) and the strain change is measured at each increment of depth.

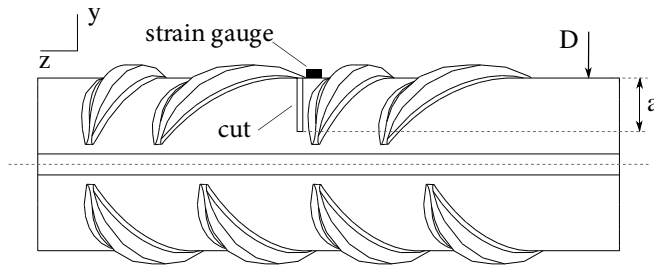


Figure 3.3 – Cut Compliance technique.

The residual stress is numerically estimated from the strain change measured during cutting. Since the cut is assumed as a crack [28], equations of Linear Elastic Fracture Mechanics are used for the residual stress calculation. Stress Intensity factor  $K_{Irs}$  due to the residual stress field at the cut tip is given by [31]:

$$K_{Irs}(a) = \frac{E'}{Z(a)} \frac{d\varepsilon}{da} \quad (3.2)$$

where  $\varepsilon$  is the strain measured during the cutting process,  $E'$  is the Young's Modulus ( $E' = E$  for plane stress and  $E' = E/(1-\nu^2)$  for plane strain) and  $Z(a)$  is called "influ-

ence function' which depends on the specimen geometry, cut plane and location of the measurement point. Eq. 3.2 is restricted to the Mode I case.  $K_{Irs}(a)$  is related to the normal residual stresses,  $\sigma_{rs}(y)$ , as given in Eq. 3.3.

$$K_{Irs}(a) = \int_0^a f(y, a) \sigma_{rs}(y) dy \quad (3.3)$$

Where  $f(y, a)$  is a weight function and  $\sigma_{rs}(y)$  can be obtained by inversion of Eq. 3.3 [31].

### Experimental description

Residual stresses were determined in a QST rebar with 16 mm diameter. A cut was incrementally introduced at the base of the transversal rib by EDM. Strain changes were measured by surface mounted strain gauges placed about 1.5 mm from the cut rim. Strain measurements were used to determine the residual stresses normal to the cut plane as a function of the cut depth. The measurements were taken near the surface up to 2 mm depth in 40 steps of 0.05 mm.

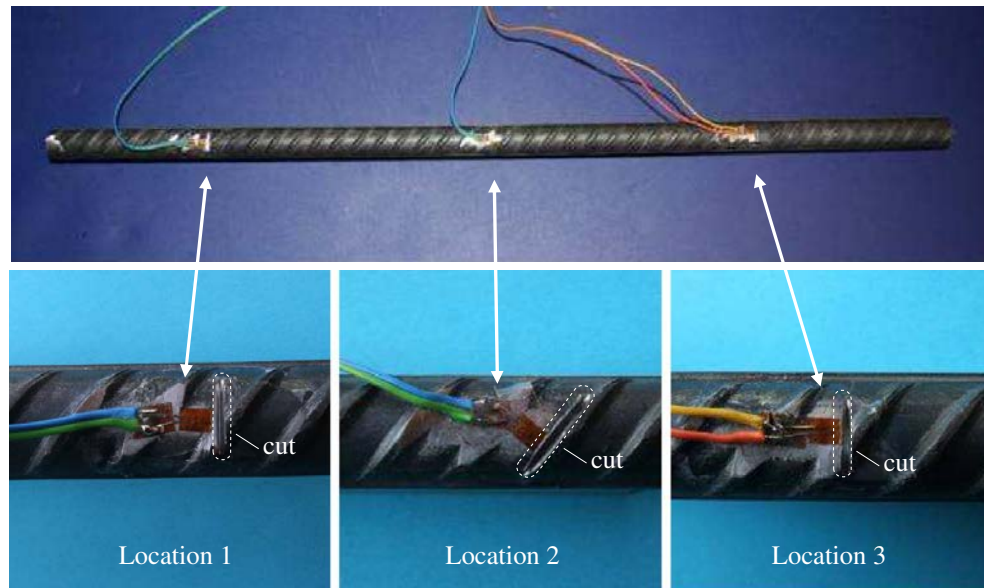


**Figure 3.4** – Location and orientation of cuts and strain gauges after measurements.

Position and orientation of cuts and strain gauges after measurements are shown in Fig. 3.4. Cuts were introduced parallel to the uniform rib and also perpendicular to the rebar axis. In this case, the stresses are at the same direction as the fatigue loading on rebars. The elastic constants  $E=205$  GPa and  $\nu=0.3$  given in [32] were



used for the residual stress calculations.

## Results and discussion

The average of the residual stresses evaluated from the strain gauge signals is given graphically in Fig. 3.5. All three profiles showed tensile residual stresses in the region covered by the measurements. The measurements show an imprecision from 5 to 10% up to 1 mm and from 10 to 20% up to 2 mm.

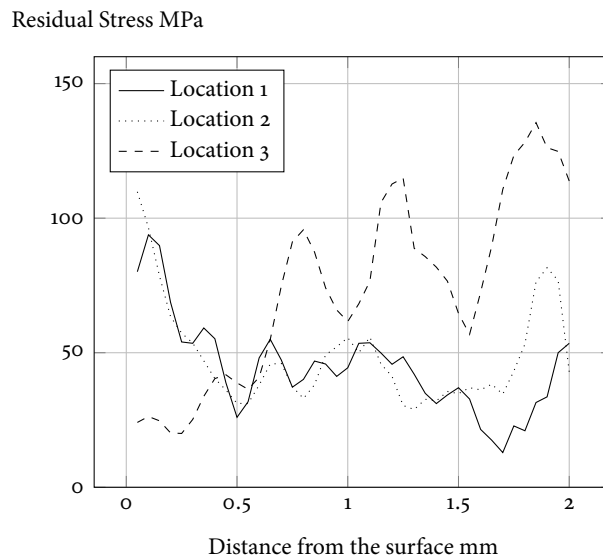


**Figure 3.5** – Longitudinal residual stress profile determined on the rebar subsurface.

A peak of stress near the surface is expected in all cases because of the notch effect at the rib base. The stress peak at the surface could not be obtained experimentally since the measurements required the introduction of a minimum cut of 0.05 mm. This peak is expected to be from 10 to 20% higher than the maximum values given at locations 1 and 3 since the rib removal may also release stress. The absence of near surface-stress peak at location 3 may be caused during rib removal by grinding. If the removal was somewhat too deep then the stress peak was eliminated. Moreover, the position of the strain gauge should be at  $90^\circ$  to the cut rim but this angle was not precisely defined.

The combination of these difficulties led to measurement uncertainties. It is likely that the more representative stress peak is at location 2 since the difficulties during the measurements could only reduce the stress peak but not amplify it. Maximum tensile residual stress of 120 MPa can be expected on the surface of QST rebar

based on CC measurement results at locations 1, 2 and 3.

### 3.5.3 X-ray diffraction technique

#### Bragg's law

When X-ray beam irradiates the surface of a crystalline material, with wavelength  $\lambda$  of same order of magnitude as the lattice spacing  $d$  of the material, Bragg diffraction occurs if scattered waves interfere constructively in accordance to the Bragg's law: the extra path  $2d\sin(\beta)$  travelled by the deepest wave is equal to integer  $n$  multiples of wavelengths [29] (see Fig. 3.6). When scattered waves satisfy the Bragg's law, a sharp intensity peak, known as Bragg peak, is produced at those diffracted directions. This intensity peak is observable by the X-ray detector.

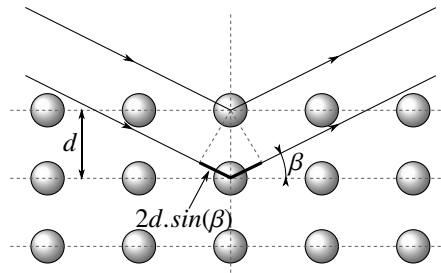


Figure 3.6 – Path difference.

The Bragg's law is given by Eq. 3.4 [29].

$$n\lambda = 2d\sin(\beta) \quad (3.4)$$

where  $\beta$  is the angle between the incident beam and the diffracting lattice planes. When the elastic properties of the material and the angular position of the Bragg peak  $2\beta$  are known, then stresses can be calculated [29]. The  $\sin^2\psi$  method is usually used to determine the residual stresses;  $d$  is plotted versus  $\sin^2\psi$  and a straight slope  $m$  is fitted by least squares regression [29].  $\psi$  is the angle between the normal of the specimen and the normal of the diffraction lattice planes.

#### Experimental description

Residual stresses were determined on the surface and subsurface of a QST rebar with 16 mm diameter. Material was removed by electrolytic polishing for measurements at depths of 0.02 and 0.05 mm. The electro polishing minimizes a possible alteration of the residual stress distribution as a result of material removal [33]. X-ray

measurements were performed between non-uniform ribs at locations MP1, MP2 and MP3 as indicated in Fig. 3.7 and between uniform ribs at locations MP4, MP5 and MP6 as shown in Fig. 3.8.

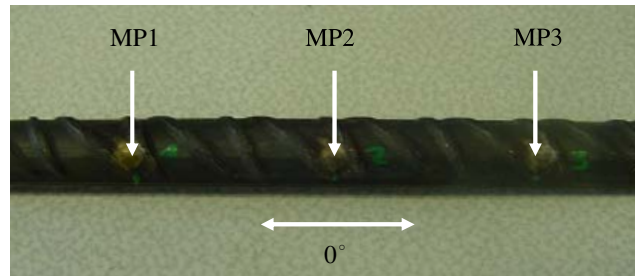


**Figure 3.7** – Locations of the X-ray measurements between non-uniform ribs.

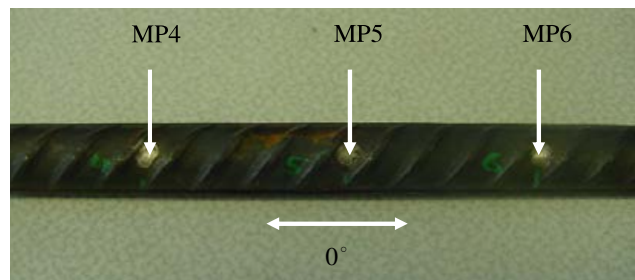


**Figure 3.8** – Locations of the X-ray measurements between uniform ribs.

CrK $\alpha$  beam was irradiated on the rebar surface over an area between 2 and 3 mm diameter. The X-ray penetration depth was about 5-7  $\mu\text{m}$ . Measurements were performed on the (211) plane with  $\lambda$  of 0.22897 nm. These parameters are recommended for ferritic and martensitic steels [29]. Measurements were taken under four tilt angles  $\psi$  of  $-5^\circ$ ,  $5^\circ$ ,  $-39^\circ$ ,  $39^\circ$  and  $2\beta$  of  $156.4^\circ$ . Young's modulus of  $E=205$  GPa and Poisson's ratio of  $\nu=0.3$  were considered for stress calculations. These values are in the range of  $E$  and  $\nu$  values in the (211) atomic plane of steels given in [34]. Residual stresses were determined by the XStress software using the  $\sin^2\psi$  method [29].

X-ray elastic constants, such as the Young's modulus, can produce systematic errors in the measured stresses [29]. Residual stress is proportional to  $E$  which can be measured or taken from the literature. However,  $E$  values found in the literature don't always provide the uncertainties around the measured values. Therefore, the uncertainties in  $E$  and  $\nu$  values were set to zero.

### 3.5.4 Results and discussion

Longitudinal residual stresses determined between uniform and non-uniform transversal ribs are given in Fig. 3.9. Measurement uncertainties varied from 2 to 9 MPa. These uncertainties are related to the peak fitting and the fit of  $d$  versus  $\sin^2\psi$  plot.

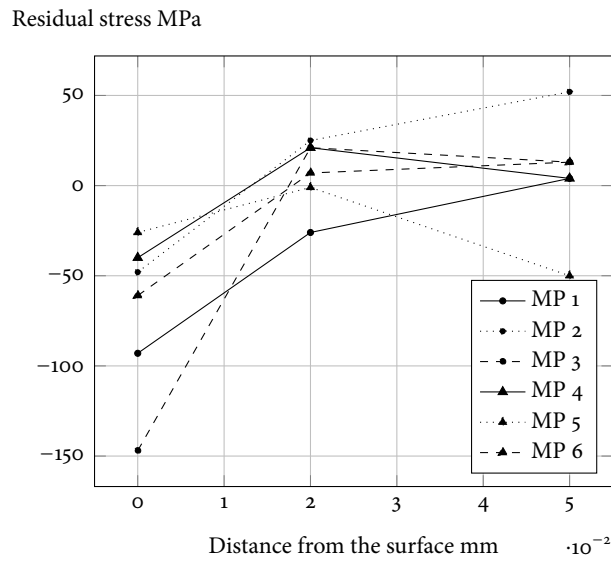


**Figure 3.9** – Longitudinal residual stresses obtained on the rebar surface and subsurface by X-ray diffraction technique.

Surface compressive residual stresses were obtained in all measurements. They varied from 48 to 147 MPa between non-uniform ribs and from 26 to 61 MPa between uniform ribs. In [24], compressive longitudinal residual stress values were also obtained for Tempcore rebars with diameters of 16, 24 and 32 mm. Surface compressive residual stresses of approximately 90 MPa were obtained by extrapolation of near surface measurements performed by the hole drilling method.

Tensile residual stresses varying between 4 to 52 MPa were determined at depth of 0.05 mm from the rebar surface (see Fig. 3.9); only a measurement taken between uniform ribs showed compressive residual stress value of 50 MPa at this depth.

Based on the X-ray diffraction measurements, tensile and compressive residual stresses can be found on the martensitic layer of QST rebars. Since fatigue cracks usually initiate on the martensitic surface layer of rebars and propagates in the presence of tensile stress fields, tensile residual stresses on the surface and near-surface may be detrimental to their fatigue performance.

### 3.6 Surface imperfections

Imperfections are introduced in the manufacturing process and create a local stress concentration effect (notch effect). They can act as crack initiator and thereby, it is important to quantify them.

In this work, surface imperfections on QST rebars were analysed by XL30-FEG SEM. Five sections were cut, from four as-received QST rebars with 16 mm diameter, by EDM. Size and orientation of these imperfections were determined.

Marks were identified near the transversal ribs as shown in Figs. 3.10a, 3.10b and 3.10c. These marks are introduced in the last rolling mill of the manufacturing process, when the ribs are formed, and they can show semi-circular shape (see Fig. 3.10b).

Cracks were identified near the marks as shown in Figs. 3.10c and 3.10d. Some of these cracks were perpendicular to the rebar axis; their length ranged from few micrometers to approximately  $200\ \mu\text{m}$  (see Fig. 3.10d). They may result from the water quenching process which produces rapid cooling and also high residual stresses that can lead to cracks on the material surface [10].

Cracks were also detected near the longitudinal ribs with similar length to the cracks identified at the vicinity of the transversal ribs. These cracks are perpendicular to the longitudinal ribs (see Fig. 3.10e).

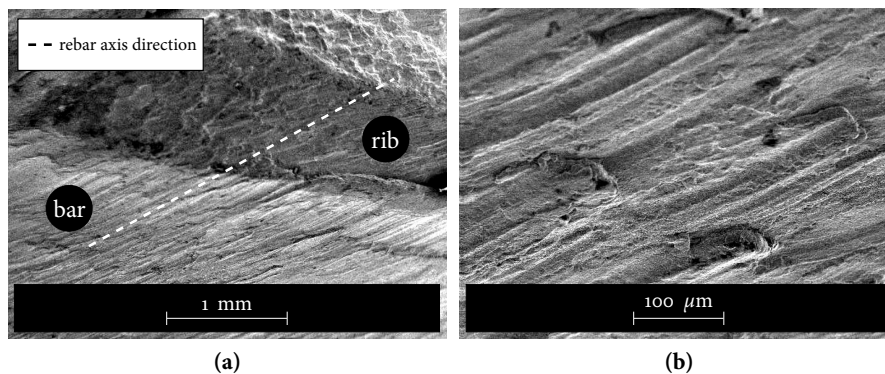


**Figure 3.10** – Surface imperfections identified on QST rebars with diameter of 16 mm (a) Marks near the transversal rib; (b) Semi-circular marks near the transversal rib.

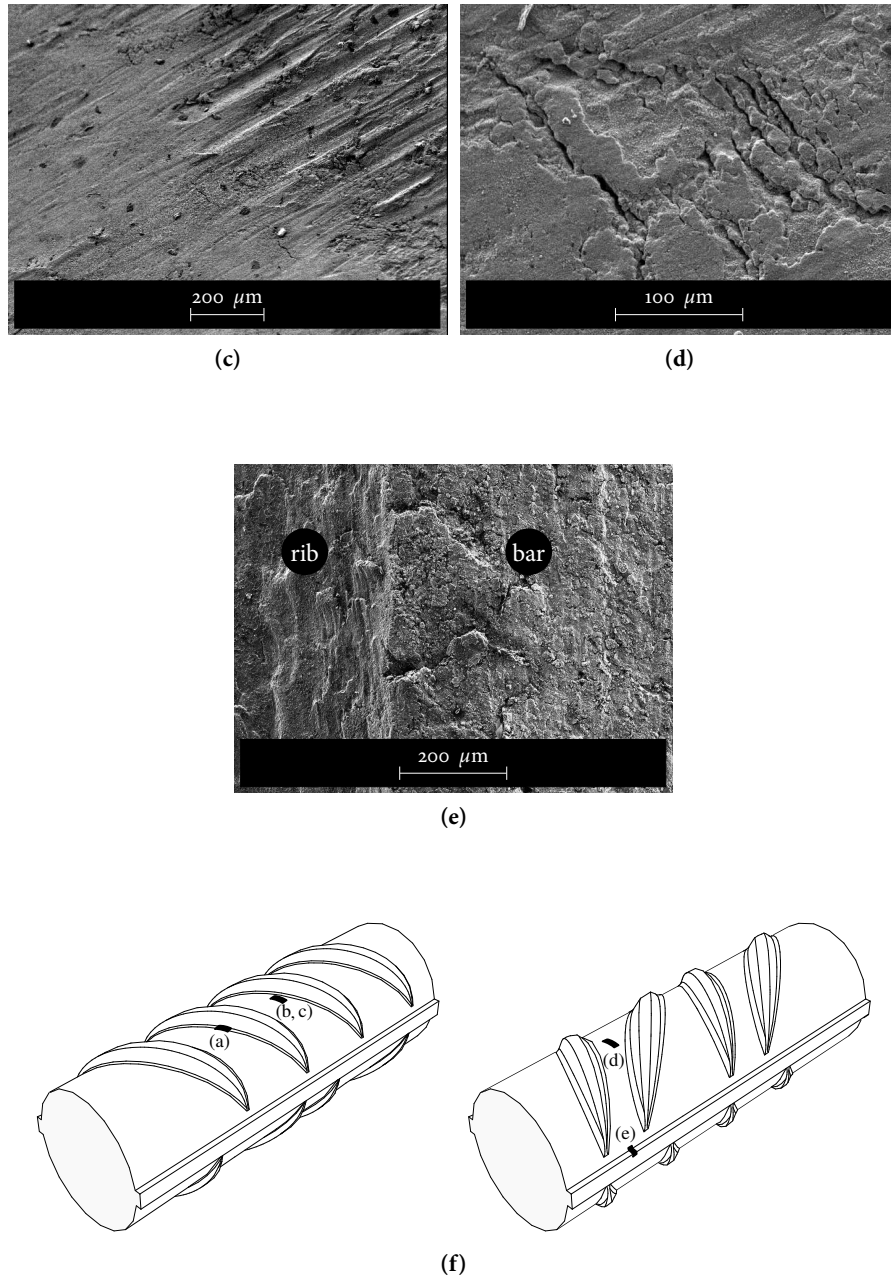


**Figure 3.10** – Surface imperfections identified on QST rebars with diameter of 16 mm (c) Marks and cracks near the transversal rib; (d) Cracks near the transversal rib; (e) Cracks perpendicular to the longitudinal rib; (f) Location of the analysed imperfections on the QST rebar surface.

## 3.7 Stress concentration

### 3.7.1 Stress concentration on the ribbed profile

A sudden change in the geometrical form of a member section produces local stress distribution. Stress concentration on rebars arises from the ribbed profile (see Fig. 3.11); they can be related to the rib geometry by the stress concentration factor  $K_t$ . This factor is defined as the ratio between the local stress at the rib and the stress assumed to be uniformly distributed over the total cross section.

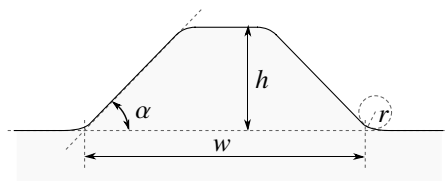


Figure 3.11 – Illustration of the ribbed profile.

Fatigue performance of rebars can be affected by the stress concentration on the rib geometry. In [22, 27], fatigue life of ribbed bars was considerable lower than smooth bars produced from the same steel. [22] associated the reduction in the fatigue strength of ribbed bars to the stress concentration on the ribs.

2D Finite Element Models FEMs have been used to investigate the influence of the rib geometry on  $K_t$  values. [35] concluded that  $K_t$  increases as the rib radius  $r$  decreases and as the rib width  $w$  and flank angle  $\alpha$  increases.  $K_t$  was found to be independent of the rebar diameter  $D$  when  $D/h$  ratio ranges from 10 to 20. [36] arrived at similar conclusions as [35]. The highest  $K_t$  values were obtained at the root of the ribs.

### 3.7.2 Numerical analysis

#### 3D Finite Element Model

$K_t$  values were determined for the rib geometry of QST rebars by Finite Element Analyses (FEA)s. Stress analyses were performed using Abaqus/CAE 6.12 software [38]. A parametric study was proposed and a script was developed to generate the 3D rib geometries. The geometrical rib details were provided by the manufacturer. A total of 24 models with different rebar diameters and rib geometries analysed in this paper is given in Table 3.4.

The flank angle  $\alpha$  of  $47.5^\circ$  and the shape of the ribs were kept constant in all models. Models without rib radius  $r$  were also investigated. Six models represent

**Table 3.4** – Geometrical parameters of the analysed models.

$D$	$r$	$h$	$w/h$	$c$	Models
10	0.2	0.03D	4.67	0.65D	D10h03r02
10	0.2	0.075D	2.97	0.65D	D10h08r02 <sup>(1)</sup>
10	0.4	0.075D	2.97	0.65D	D10h08r04 <sup>(1)</sup>
10	0.2	0.15D	2.40	0.65D	D10h15r02
10	0.4	0.15D	2.40	0.65D	D10h15r04
10	-	0.075D	2.97	0.65D	D10h08
16	0.2	0.03D	4.67	0.6D	D16h03r02
16	0.2	0.075D	2.97	0.6D	D16h08r02 <sup>(1)</sup>
16	0.4	0.075D	2.97	0.6D	D16h08r04 <sup>(1)</sup>
16	0.8	0.075D	2.97	0.6D	D16h08r08
16	0.2	0.15D	2.40	0.6D	D16h15r02
16	0.4	0.15D	2.40	0.6D	D16h15r04
16	0.8	0.15D	2.40	0.6D	D16h15r08
16	-	0.075D	2.97	0.6D	D16h08
16	0.4	0.075D	2.97	0.4D	D16h08r04c04
16	0.4	0.075D	2.97	1.2D	D16h08r04c12
16	0.4	0.075D	2.97	0.6D	D16h08r04 $\theta$ 90 <sup>(2)</sup>
26	0.2	0.03D	4.67	0.6D	D26h03r02
26	0.2	0.075D	2.97	0.6D	D26h08r02 <sup>(1)</sup>
26	0.4	0.075D	2.97	0.6D	D26h08r04 <sup>(1)</sup>
26	0.8	0.075D	2.97	0.6D	D26h08r08
26	0.4	0.15D	2.40	0.6D	D26h15r04
26	0.8	0.15D	2.40	0.6D	D26h15r08

Notes:

<sup>(1)</sup> Models which represent the original geometry of the QST rebars. They are referred as original models.<sup>(2)</sup> Model with rib inclinations of 90°.



the original geometry of the QST rebars i.e., the geometry as provided by the manufacturer. These models are indicated in Table 3.4.

Fig. 3.12 illustrates the typical rib geometry on both sides of the QST rebar analysed in this work. Four ribs were modelled on both sides of the bar and the  $K_t$ 's were analysed on the centre ribs (see Fig. 3.12). QST rebar shows uniform ribs with inclination  $\theta_1$  of  $54^\circ$  and non-uniform ribs with inclinations  $\theta_2$  of  $46^\circ$  and  $\theta_3$  of  $64^\circ$  as given in Fig. 3.12. Stress analyses were performed for paths 1) along the transition line between the weld toe radius and the rebar cylinder, referred in this paper as TL, and 2) perpendicular to the rib axis as indicated in blue color in Fig. 3.12. The influence of the rib geometry on the bond characteristics between concrete and rebar was not considered in this work. However, the parameter variations of the original models such as rib height  $h$  ( $0.03D$ ,  $0.15D$ ) and rib spacing  $c$  ( $0.4D$ ,  $1.2D$ ) were chosen according to recommendations given in [37].

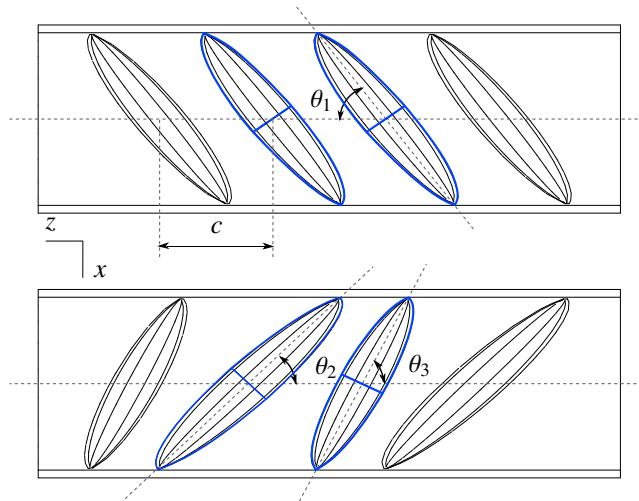


**Figure 3.12** – Illustration of the rib geometry and the paths along and perpendicular to the ribs where stress concentrations were investigated.

A free mesh was generated using 10-node quadratic tetrahedral elements (C3D10). The rib radius  $r$ , which is the critical region on the ribbed profile, was meshed finer. The location away from this region was coarser to save computing time. A uniform tensile stress was applied to the models and the material was considered elastic and isotropic. Material properties  $E=205$  GPa and  $\nu=0.3$  were considered as given in [32].

The mesh convergence was verified to obtain an optimum mesh density. Average element sizes  $e$  ranging from 0.8 to 0.05 mm were created for  $r$  equal to 0.2, 0.4

and 0.8 mm. A resulting mesh is given in Fig. 3.13.

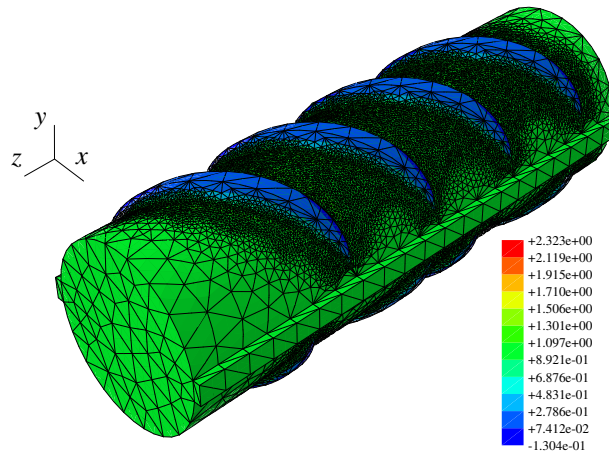


Figure 3.13 – Typical mesh considered in the models.

Fig. 3.14 shows the mesh convergence obtained for  $r=0.2$  mm.  $K_t$  curves obtained along  $r=0.2$  mm converged for  $e \leq 0.1$  mm. The mesh convergence for both  $r=0.4$  and 0.8 mm was verified for  $e \leq 0.2$  mm.

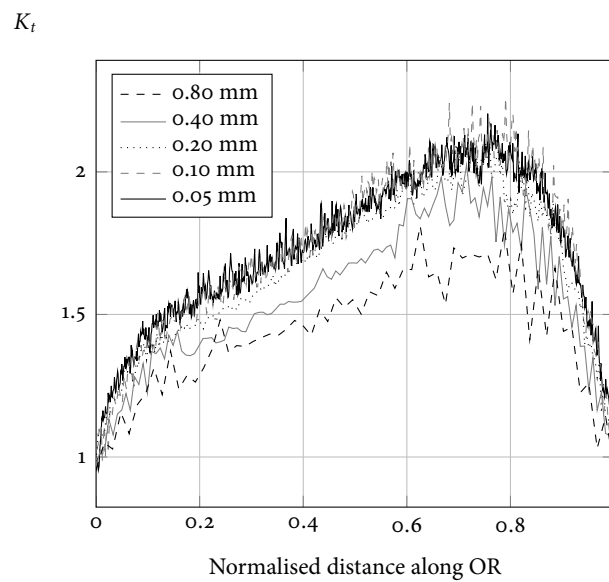
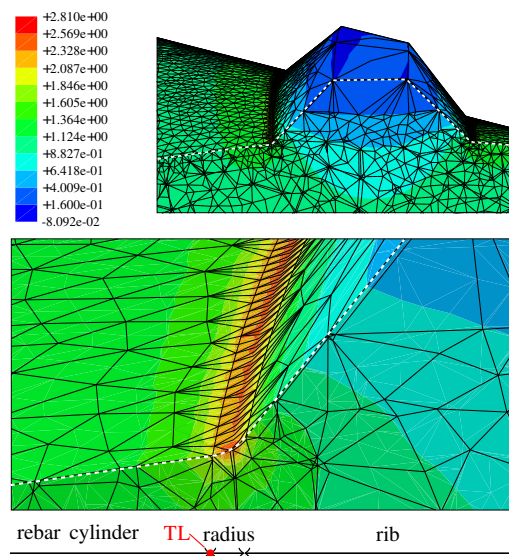


Figure 3.14 – Mesh convergence for rib radius  $r=0.2$  mm.

### 3.7.3 $K_t$ determined on the rib

$K_t$  values were calculated as the ratio between the largest principal stress and the applied stress.  $K_t$  curves were linearised using a sixth order polynomial function as given in Fig. 3.16. The maximum value obtained in a  $K_t$  curve after linearisation is referred as peak value (PV) in this paper.

Stress concentration profile determined in a perpendicular to the rib axis showed that the zone with higher stress concentrations was obtained at the radius region as shown in Fig. 3.15. PVs determined at the root of the ribs were utmost 20% higher than PVs determined at TL.  $K_t$  values dropped in direction to the centre of the rib where no stress concentration was observed.



**Figure 3.15** – Stress concentration profile obtained in a perpendicular to the rib axis of D26ho8ro2 model.

As shown in Fig. 3.15, the rib itself does not show high stresses. The radius region was the critical region since it showed the maximum stress concentrations. This is in agreement with the results of [36].

#### Influence of the rib inclination

Fig. 3.16 shows typical  $K_t$  curves obtained along TL. The smallest stresses along PT were obtained at the rib ends. The maximum  $K_t$  value at these locations was 1.2. PVs were similar between the different rib inclinations  $\theta$ . However, the peak positions (PP)s tended to move to the centre of TL with the increase of  $\theta$ ; for  $\theta$  of  $90^\circ$  for

example, PP was at the centre of TL as shown in Fig. 3.16.

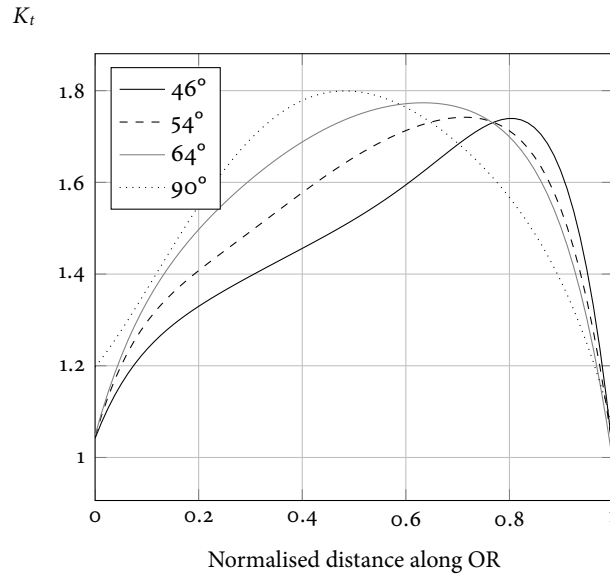


**Figure 3.16** –  $K_t$  curves obtained for different rib inclinations  $\theta$  of D16ho8ro4 and D16ho8ro4 $\theta$ 90 models.

PVs and PPs determined along TL for different  $\theta$  are given in Table 3.5.

Zones along TL with  $K_t$  equal or higher than 95% of PVs were analysed. These zones are referred as peak zones (PZ)s in this paper. PZs of the original models were anti-symmetrically located along TL and they showed similar sizes as given in Fig. 3.17. Fig. 3.18 shows PZ sizes obtained for different  $\theta$ . PZ sizes increased along TL as  $\theta$  increased;  $\theta$  of  $64^\circ$ , for example, showed higher PZ sizes compared to the ribs with inclination of  $46^\circ$  and  $54^\circ$ . However, the increase of  $\theta$  from  $64^\circ$  to  $90^\circ$  had a negligible influence on the PZ sizes.

### Influence of the radius

The increase of  $r$  resulted in the reduction of the PVs of the original models (see Table 3.5). PVs decreased in 14 to 21% with the increase of  $r$  from 0.2 to 0.4 mm and dropped by 15% with the change of  $r$  from 0.4 to 0.8 mm. The maximum PV obtained along TL for the original models was 2.50. In the models with no radius, PVs was utmost 20% higher than PVs of the models with  $r=0.2$  mm.

Fig. 3.19 shows the PPs and PZs obtained along TL with the change of  $r$ . Small variation on the PPs of the original models was obtained with the increase of  $r$ . The increase of  $r$  led to an increase of the PZ sizes: the change of  $r$  from 0.2 to 0.4 mm,

**Table 3.5** – Peak values (PV)s and Peak positions (PP)s determined along the transition line (TL).

Models	Rib inclination $\theta$					
	46°		54°		64°	
	PV	PP	PV	PP	PV	PP
D10h03r02	1.56	0.82	1.61	0.71	1.63	0.64
D10h08r02	1.90	0.82	1.90	0.73	1.89	0.63
D10h08r04	1.59	0.79	1.61	0.73	1.64	0.64
D10h15r02	2.44	0.76	2.36	0.73	2.37	0.67
D10h15r04	2.19	0.74	1.92	0.70	2.13	0.55
D10h08	2.15	0.81	2.27	0.75	2.25	0.65
D16h03r02	1.72	0.82	1.79	0.71	1.83	0.63
D16h08r02	2.09	0.81	2.15	0.76	2.15	0.68
D16h08r04	1.76	0.80	1.78	0.72	1.80	0.63
D16h08r08	1.53	0.79	1.54	0.73	1.56	0.63
D16h15r02	2.79	0.77	2.68	0.72	2.74	0.62
D16h15r04	2.28	0.76	2.18	0.70	2.26	0.53
D16h15r08	1.99	0.74	1.87	0.67	1.97	0.47
D16h08	2.45	0.81	2.48	0.76	2.48	0.68
D16h08r04c04	1.95	0.76	1.81	0.67	1.98	0.35
D16h08r04c12	1.74	0.82	1.75	0.75	1.77	0.68
D26h03r02	1.95	0.80	2.04	0.72	2.09	0.62
D26h08r02	2.46	0.82	2.45	0.75	2.50	0.68
D26h08r04	1.95	0.80	1.98	0.73	1.97	0.61
D26h08r08	1.66	0.80	1.70	0.72	1.71	0.65
D26h15r04	2.53	0.77	2.48	0.71	2.50	0.58
D26h15r08	2.19	0.75	2.07	0.67	2.15	0.52

Notes:

D16h08r04 $\theta$ 90 model: all ribs with the same inclination of 90°;  
PV = 1.85 and PP = 0.5.

for example, resulted to an increase up to 11% on the PZ sizes.

### Influence of the height

The reduction of  $h$  resulted in the decrease of PVs as shown in Table 3.5. The change of  $h$  from  $0.075D$  to  $0.03D$  reduced PVs from 14 to 21%. The maximum PV determined for the models with  $h=0.3D$  was 2.09. Fig. 3.20 shows the PPs and PZs obtained for models with different  $h$ . Small variation on the PPs was observed; PZ sizes increased up to 15% with  $h$  reduction from  $0.075D$  to  $0.03D$ . The increase of  $r$  from 0.2 to 0.4 mm had similar effect on PVs as the change of  $h$  from  $0.075D$  to  $0.03D$ .

The maximum PV of 2.79 was determined between all analysed models (see

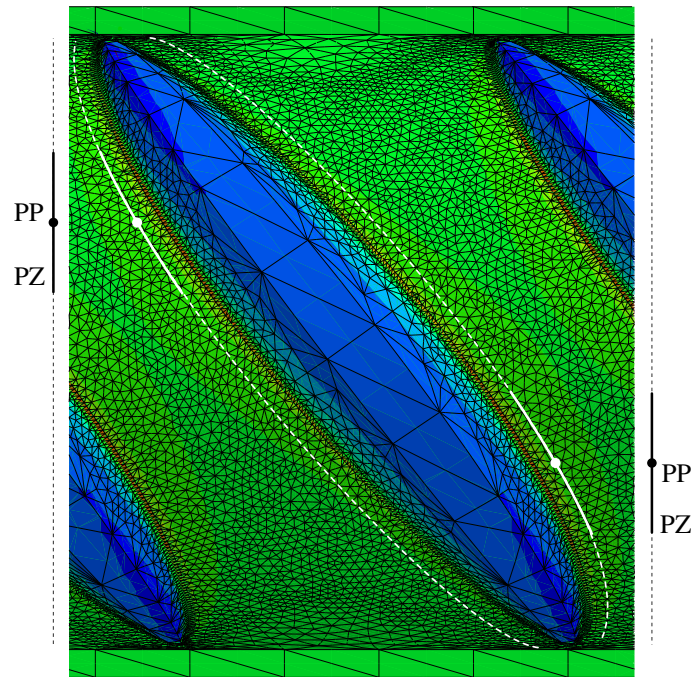


**Figure 3.17** – Example of the peak positions (PP)s and peak zones (PZ)s along the rib of an original model.

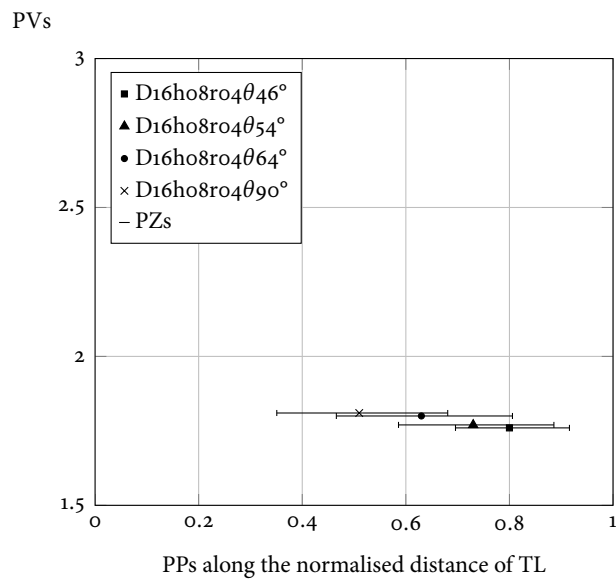


**Figure 3.18** – Influence of the rib inclination  $\theta$  on  $K_t$ .

Table 3.5). This value resulted from a combination of highest  $h=0.15D$  and smallest  $r=0.2$ . Models with  $h=0.15D$  combined with  $r=0.4$  or  $0.8$  mm affected both PVs and

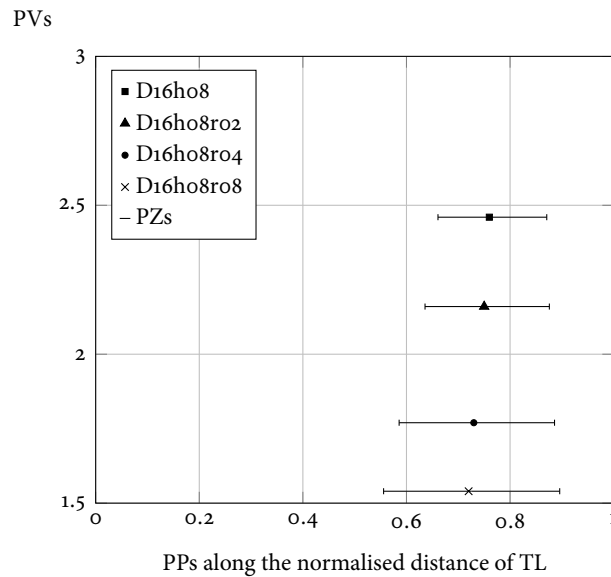


Figure 3.19 – Influence of the rib radius  $r$  on  $K_t$

PPs of the non-uniform ribs. As the flank angle  $\alpha$  was kept constant in all models, the increase of  $h$  was followed by the increase of the rib width  $w$ . Beside, the increase of  $r$  and the different rib inclination  $\theta$  reduced significantly the distance between the non-uniform ribs. As a consequence, it created a region of stress concentrations moving the PPs of the ribs to this zone. The reduction of the distance between non-uniform ribs increased PVs of these ribs. Therefore, these rib geometries should be avoided.

### Influence of the diameter

The increase of  $D$  resulted in the increase of PVs as shown in Table 3.5. PVs of the original the models increased up to 14% as  $D$  changed from 10 to 16 mm and to utmost 18% for  $D$  increasing from 16 to 26 mm.

Fig. 3.21 shows PPs and PZs obtained for the original models with 10, 16 and 26 mm diameters. Small variation on the PPs and PZ sizes was obtained with the change of  $D$  from 10 to 16 mm and from 16 to 26 mm.

### Influence of the rib spacing

Rib spacing  $c$  change had small influence on the PVs and PZ sizes along TL as shown in Fig. 3.22. The  $c$  parameter had smaller influence on the  $K_t$  values and PZ sizes

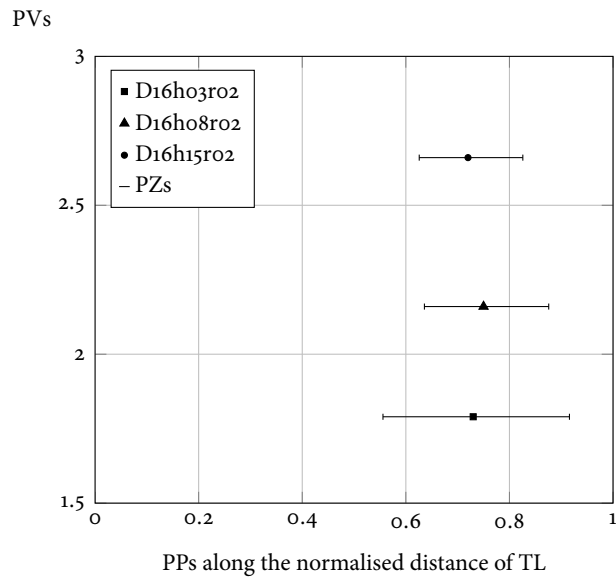


**Figure 3.20** – Influence of the rib height  $h$  on  $K_t$ .

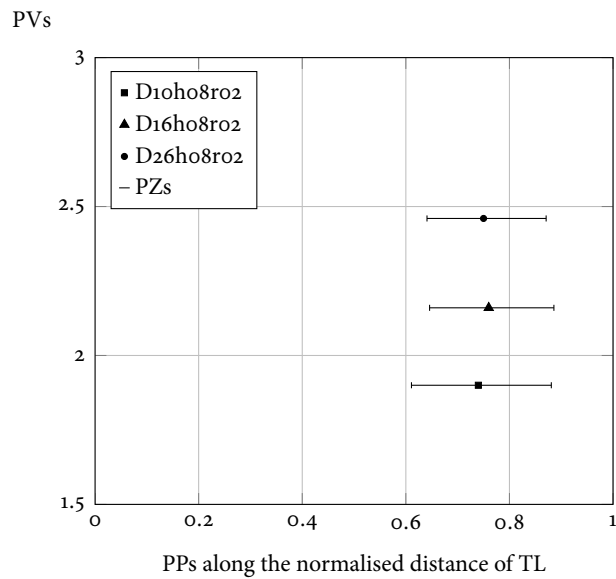


**Figure 3.21** – Influence of the rebar diameter  $D$  on  $K_t$ .

compared to other analysed parameters.

However, the reduction of  $c$  from  $0.6D$  to  $0.4D$  affected the PVS and PPs of the non-uniform ribs (see Table 3.5). Similar case was obtained for models with  $h=0.15D$  combined with  $r=0.4$  or  $0.8$  mm.



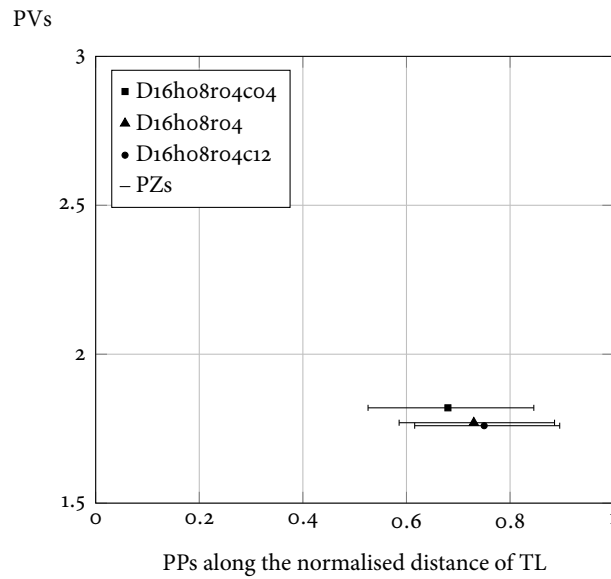


Figure 3.22 – Influence of the rib spacing  $c$  on  $K_t$ .

### 3.8 Conclusions

In this work, characterisation studies of QST rebars included 1) Identification of the microstructure and hardness measurements in the cross section of rebars with different diameters. The average grain size of the core microstructure was quantified and compared to the grain size of QST and HR rebars given in the literature. 1) Residual stresses were experimentally determined on surface and subsurface of QST rebars with 16 mm diameter by Cut Compliance and X-ray diffraction techniques. Results obtained from both techniques were discussed and compared to residual stresses of QST rebars found in the literature. 2) SEM analyses on the rebar surface allowed to identify and quantify imperfections originated in the manufacturing process. 3) A parametric study was developed to analyse the influence of the rib geometry and rebar diameter on the stress concentration factors  $K_t$  along the rib. The findings of this study suggest that:

- The average grain size in the core of QST rebars increase with the increase of diameter. However, the microstructure of QST rebars is finer than the microstructure of hot rolled rebars with higher diameter.
- Random tensile and compressive residual stresses are expected on the surface and subsurface of QST rebars. These stresses are no higher than 20% of their yield strength.

- Surface imperfections originated in the manufacturing process are near the transversal and longitudinal ribs. As imperfections are zones of stress concentration and may affect the performance of rebars in service, they should be avoided.
- The highest stress concentrations arising from the ribbed profile are located at radius region. The main parameters of the rib geometry affecting the maximum  $K_t$ 's are the radius and height; maximum  $K_t$  values at the radius region can be significantly reduced with the increase of the radius and reduction of the height.
- The rib inclination is the main parameter affecting the position of the maximum  $K_t$ 's as well as the critical zone sizes along the rib. The critical zones correspond to the zones where  $K_t$ s are at least 95% of the maximum values. These critical zones are located anti-symmetrically along the rib. As near the rib inclination is to a perpendicular of the rebar axis, the maximum  $K_t$ 's tends to move to the rib centre and the critical zone sizes increase.
- Maximum  $K_t$ 's along the ribs increase with the rebar diameter increasing and its influence in the maximum  $K_t$  is comparable to the changes in the rib radius and height. However, the effect of the diameter on the critical zone size is less significant than those parameters.
- The reduction of the rib spacing should be avoided for non-uniform ribs since it increases the maximum  $K_t$  values.

### 3.9 Acknowledgements

The authors are grateful to Danièle Laub from the Interdisciplinary Centre For Electron Microscopy (CIME) at EPFL for her help with the sample preparation for the microscopic analyses. We are also grateful to Cyril Dénéréaz from the Mechanical Metallurgy Laboratory (LMM) for the hardness measurements.



---


## *Bibliography*

---

- [1] Domone, P., & Illston, J. (2010). *Construction materials: Their nature and behaviour*. CRC Press.
- [2] Basu, P. C., Shyamoni, P., & Roshan, A. D. (2004). Characterisation of steel reinforcement for RC structures: An overview and related issues. *Indian Concrete Journal*, 78(1), 19-30.
- [3] Ray, A., Mukerjee, D., Sen, S. K., Bhattacharya, A., Dhua, S. K., Prasad, M. S., & Sahu, A. K. (1997). Microstructure and properties of thermomechanically strengthened reinforcement bars: A comparative assessment of plain-carbon and low-alloy steel grades. *Journal of Materials Engineering and Performance*, 6(3), 335-343.
- [4] Economopoulos, M., Respen, Y., Lessel, G. & Steffes, G. (1975). Application of the Tempcore process to the fabrication of high yield strength concrete - reinforcing bars. *Metallurgical reports CRM*, (45), 3-19.
- [5] Rehm, G., & Russwurm, D. (1977). Assessment of concrete reinforcing bars made by the Tempcore process. *Metallurgical reports CRM*, (51), 3-16.
- [6] Virmani, Y. P., Wright, W., & Nelson, R. N. (1991). Fatigue testing for Thermex reinforcing bars. *Public Roads*, 55(3), 72-78.
- [7] Simon, P., Economopoulos, M., & Nilles, P. (1984a). Tempcore: A new process for the production of high-quality reinforcing bars. *Iron Steel Engineer*, 61(3), 53-57.
- [8] Simon, P., Economopoulos, M., & Nilles, P. (1984b). Tempcore: An economical process for the production of high quality rebars. *Metallurgical Plant and Technology* 1984b, (3), 80-93.

- [9] Kelestemur, O., Kelestemur, M. H., & Yildiz, S. (2009). Improvement of mechanical properties of reinforcing steel used in the reinforced concrete structures. *Journal of Iron and Steel Research, International*, 16(3), 55-63.
- [10] Totten, G., E. (2006). *Steel heat treatment: Metallurgy and technologies*. CRC Press.
- [11] Zheng, H., & Abel, A. A. (1997). Residual stress effects on the fatigue properties of Tempcore reinforcing steel. *Technology Transfer Series*, 177-182.
- [12] ISO 4948-1 (1982). *Steels - classification - part 1: Classification of steels into unalloyed and alloy steels based on chemical composition*.
- [13] Bhadeshia, H., & Honeycombe, R. (2006). *Steels: Microstructure and properties*. Butterworth - Heinemann, p. 117.
- [14] Russwurm, D., & Martin, H. (1993). *Betonstähle für den Stahlbetonbau: Eigenschaften und Verwendung*. Wiesbaden: Bauverlag, p. 53.
- [15] ASTM E3-11 (2011). *Standard guide for preparation of metallographic specimens*.
- [16] Bramfitt, B. L., & Benschoter, A. O. (2002). *Metallographer's guide: Practices and procedures for iron and steels*, ASM International.
- [17] E112-12 (2012) *Standard test methods for determining average grain size*.
- [18] E562-11 (2011). *Standard test method for determining volume fraction by systematic manual point count*.
- [19] Mukherjee, M., Dutta, C., & Haldar, A. (2012). Prediction of hardness of the tempered martensitic rim of TMT rebars. *Materials Science and Engineering: A*, 543, 35-43.
- [20] Tilly, G. P. (1979). Fatigue of steel reinforcement bars in concrete: A review. *Fatigue & Fracture of Engineering Materials & Structures*, 2(3), 251-268.
- [21] Hanson, J. M., Burton, K. T., & Hognestad, E. (1968). Fatigue tests of reinforcing bars - effect of deformation pattern. *Journal of the PCA Research and Development Laboratories*, 10, 2-13.
- [22] Jhamb, I. C., & Mac Gregor, J. G. (1974). Effect of surface characteristics on fatigue strength of reinforcing steel. *ACI Special Publication*, 41-7, 139-168.

- [23] ISO 6507-1 (2005). Metallic materials - Vickers hardness test-part 1: Test method.
- [24] Zheng, H., & Abel, A. A. (1999). Fatigue properties of reinforcing steel produced by Tempcore process. *Journal of Materials in Civil Engineering*, 11(2), 158-165.
- [25] Tisza M. (2001). *Physical metallurgy for engineers*. ASM International, pp. 280-281.
- [26] Baydogan, M., Uysal, A., Kayali, E. S., & Cimenoglu, H. (2005). 4698 - Investigation on cyclic deformation behaviour of reinforced steel bars. In ICF11, Italy.
- [27] Hanson, J. M., Somes, N. F., Helgason, T., Corley, W. G., & Hognestad, E. (1970). Fatigue strength of high-yield reinforcing bars. National Cooperative Highway Research program (NCHRP). Final report - Project n°4-7. Illinois.
- [28] Schindler, H. J., Bertschinger, P., & Semenov, B. Near-surface stress measurement in 2D and 3D by the cut compliance technique. In *Materials Science Forum*, 404, 515-520.
- [29] Lu, J. (1996). *Handbook of measurement of residual stresses*.
- [30] Withers, P. J., Turski, M., Edwards, L., Bouchard, P. J., & Buttle, D. J. (2008). Recent advances in residual stress measurement. *International Journal of Pressure Vessels and Piping*, 85(3), 118-127.
- [31] Schindler, H. J. (2000). Residual stress measurement in cracked components: Capabilities and limitations of the cut compliance method. In *Materials Science Forum*, 347, 150-155. Transtec Publications, 1999.
- [32] Standard SIA 262 (2003). *Concrete structures*. Swiss Society of Engineers and Architects, Zurich.
- [33] Fitzpatrick, M. E., Fry, A. T., Holdway, P., Kandil, F. A., Shackleton, J., & Suominen, L. (2002). Determination of residual stresses by X-ray diffraction. Measurement good practice guide n°52. National Physical Laboratory, Teddington, Middlesex, UK.

- 
- BIBLIOGRAPHY
- [34] Wimpory, R. C., & Ohms, C. (2010). A step towards a complete uncertainty analysis of residual stress determination using neutron diffraction. In *Materials Science Forum*, 638, 2487-2492.
  - [35] Jhamb, I. C., & MacGregor, J. G. (1974). Stress concentrations caused by reinforcing bar deformations. *ACI Special Publication*, 41-8, 169-182.
  - [36] Zheng, H., & Abel, A. (1998). Stress concentration and fatigue of profiled reinforcing steels. *International Journal of Fatigue*, 20(10), 767-773.
  - [37] EN 10080 (2005) Steel for the reinforcement of concrete, weldable, ribbed reinforcing steel.
  - [38] Abaqus (2012) Analysis user's manual version 6.12, Dassault Systèmes Simulia Corp., Providence, USA.

## Microstructural influence on the scatter in the fatigue life of steel reinforcement bars

— Marina Rocha, Eugen Brühwiler, Alain Nussbaumer

**Abstract:** *Fatigue test results with steel reinforcement bars (rebars) is a stochastic process. Scatter can be influenced by the sensitivity of the short crack growth to the microstructural features, especially near the fatigue limit. This work investigates the scatter inherent to the microscopic conditions near the fatigue limit of ferrite-pearlite and martensite microstructures found in the outer layer of rebars. An adapted Navarro-De Los Rios model within a Monte-Carlo framework is used to simulate the short crack growth in material grains. Grain size variation, grain orientation factor and multiple phases were considered in the model. The results are compared with the scatter found in fatigue tests on hot-rolled-cold worked as well as quenched and tempered rebars. It is shown that microstructural effects explains part of the observed scatter in the fatigue tests.*

**Keywords:** Short fatigue crack growth; Ferrite-pearlite; Tempered martensite; Scatter above the fatigue limit.





## Contents

<b>4.1</b>	<b>Introduction</b>	<b>65</b>
<b>4.2</b>	<b>Reconstruction of parent austenite grains</b>	<b>68</b>
4.2.1	Experimental analysis	68
<b>4.3</b>	<b>Short crack growth model</b>	<b>70</b>
4.3.1	Grain structure	70
4.3.2	Grain orientation	75
4.3.3	Material properties	77
<b>4.4</b>	<b>Results and Discussion</b>	<b>78</b>
<b>4.5</b>	<b>Conclusion</b>	<b>81</b>
<b>4.6</b>	<b>Acknowledgements</b>	<b>82</b>

### 4.1 Introduction

Fatigue life assessment of engineering structures depends on the knowledge of material properties. Fatigue limit is a macroscopic property of the material that is sensitive to microscopic conditions. Since metal fatigue is a random process, fatigue data from testing always exhibit scatter for specimens of the same geometry, under same loading condition, especially near the fatigue limit. Besides, for metallic materials, the crack initiation period often dominates the fatigue life just above this limit. Since fatigue crack initiation is mainly a surface phenomenon, specimen surface roughness, protrusions and microscopic aspects such as grain size, grain orientation, dislocation density can influence the scatter in fatigue lives and fatigue limit stress range. The large scatter observed in fatigue tests lead to high values of confidence intervals (CIs) to get the design S-N curves. Further scatter result from the damage accumulation models used in fatigue life verifications. In most design codes, including those for steel reinforcement bars (rebars), usually considers 95% CIs.

Furthermore, one single design S-N curve regroup rebars produced from hot rolling, cold working and quenching and self-tempering with different surface microstructures, rib patterns and surface roughness, all of which increase the scatter near the fatigue limit and lead to very conservative design values. In order to understand the scatter inherent to microscopic aspects in the fatigue behaviour of rebars, this work proposes a short crack growth model to simulate the initiation period

in ferrite-pearlite and tempered martensite grains found on the surface of different types of rebars.

Fatigue crack initiation period in metallic material consists of cyclic slip, crack nucleation and short crack growth [1]. These cracks can behave significantly different from the (long) crack propagation as described by Paris' law [2,3]. Short cracks can grow faster than corresponding long cracks at the same value of stress intensity factor range,  $\Delta K$ . They can also grow at significant rates for  $\Delta K$  value smaller than the threshold for long cracks [4].

Surface microscopic investigations in steel specimens has shown that short cracks form on slip bands and propagates along them [3]. The short crack propagation stops when the applied stress is below the fatigue limit; when the stress is just above this limit, the crack accelerates and decelerates due to the interactions with microstructural barriers until it reaches a long crack regime with apparent continuous propagation rate. The crack growth rate decreases as approaching the grain or phase boundary; the crack then accelerates when a slip band is initiated in the adjacent grain [2,5].

Navarro and De Los Rios (N-R) [6,7] proposed a short crack growth model where a crack initiates from slip bands. This model is particularly appropriate to study fatigue limit problems which involve microstructurally short cracks. N-R model considers the interaction between crack and microstructural barriers. It assumes that dislocations are constrained to remain on their original plane and pile up when blocked by grain boundaries. They propagate along slip bands extending through successive grains.

N-R model can be considered as a further development of research in [3,8,9]. Bilby et al. [8] were the first to obtain a bounded solution for the dislocation distribution function representing the crack and the plastic zone (slip band ahead of the crack tip). [3,9] showed that the crack tip plastic zone interacts with microstructural barriers, such as grain boundaries, when the crack is of the order of microstructural features. [9] developed the unbounded solution for the dislocation distribution function.

In its original form, N-R model considers infinitesimal dislocations distributed within two zones: the crack itself  $a$  (half crack length) and the plastic zone  $c$  as shown in Fig. 4.1. In this two-zone model, an infinite stress level is sustained by the grain boundary. In [10], the model was extended by considering an additional small zone of length  $r_o \ll D$ , ( $D$  is the, uniform, grain diameter) representing the interface between neighbouring grains or phases (see Fig. 4.1). This model elimi-

nates the singularity of the stress field associated to the distribution of dislocations. In physical terms, the three-zone system was argued to be more realistic since the plastic zone is blocked by the grain boundary i.e., its two boundaries, and it remains blocked until the stress in the third zone i.e., the grain boundary, attains a critical level for dislocations to cross this zone.

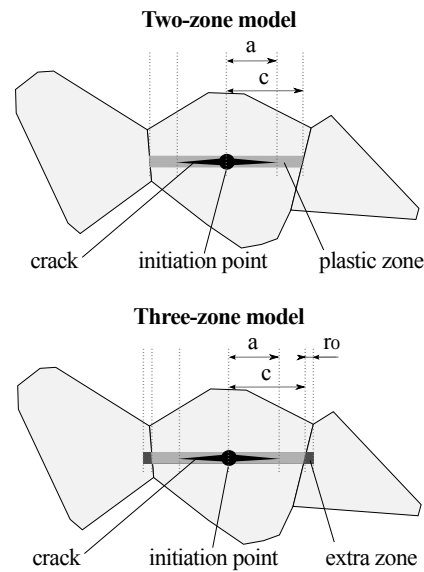


**Figure 4.1** – Two-zone [6], [7] and three-zone [10] models.

N-R model has been extensively used (or extended) to predict the fatigue life-time of metals. In [11], N-R model was applied to predict the short fatigue crack growth behaviour in mild steel. In [12], N-R model was applied for fatigue life prediction of commercially pure aluminium. The model prediction was in good agreement with experimental results. In [13], the effect of textures was investigated in the short fatigue crack growth in Al-Li alloy. An equation for the grain orientation factor was proposed depending on the load axis, slip plane normal and slip direction. N-R model was extended for biaxial fatigue loading case in low and medium Carbon steels; the crack initiation orientation was close to the experimental results [14]. The influence of the grain size variation was introduced in the N-R model by [15] where Voronoi cells were used to represent the grain structure. In [16], a micromechanical model for short crack growth based on successive blocking of monotonic plastic zone and cyclic plastic zone of a crack at grain boundaries was proposed. This model was based on the N-R approach [10]. These models successfully reproduced the short crack growth pattern where the crack decelerates at a grain boundaries and it accelerates when crossing a grain.

This irregular behaviour of short cracks due to the interactions with the microstructure can affect the scatter found near the fatigue limit. Factors such as grain size variation [3], grain orientation [13] and different phases [2] are more prominent at low stress levels and consequently influence the fatigue crack initiation period.

In this study, the influence of the microstructure on the scatter observed in experimental data as obtained above the fatigue limit is investigated using an adapted N-R model within a Monte-Carlo framework. The short crack growth is simulated in ferrite-pearlite (F-P) and tempered martensite (TM) grains found on the outer layer of rebars. The grain structure is represented by Voronoi tessellation. In the F-P model, the two phases, pearlite and ferrite, were modelled separately with the area fraction of each phase being obtained from the literature. On the other hand, the parent austenite grain is considered for short crack growth modelling in TM. The parent grain is experimentally determined using Electron Back Scattered Diffraction (EBSD) and ARPGE software. The scatter obtained in the crack initiation phase is compared to experimental data from the literature.

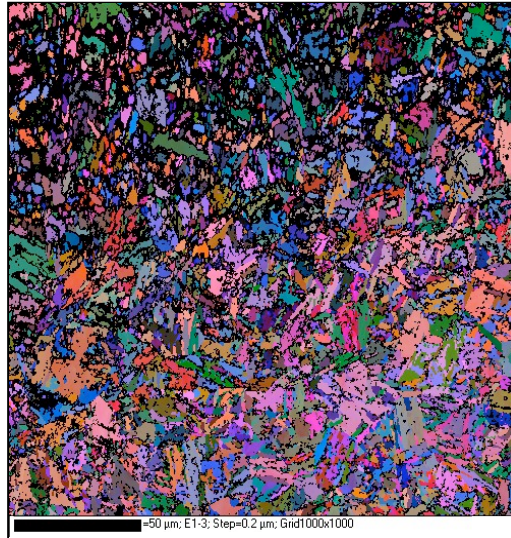
## 4.2 Reconstruction of parent austenite grains

The laths of (daughter) martensite are organized within the parent austenite grains. The austenite grain size represents an essential characteristic of martensite steels; fine austenite grain results in the formation of fine martensite and consequently improvement in the mechanical properties of martensite steels [17]. In this work, slip band and short crack growth is simulated in the austenite grains of TM steel.

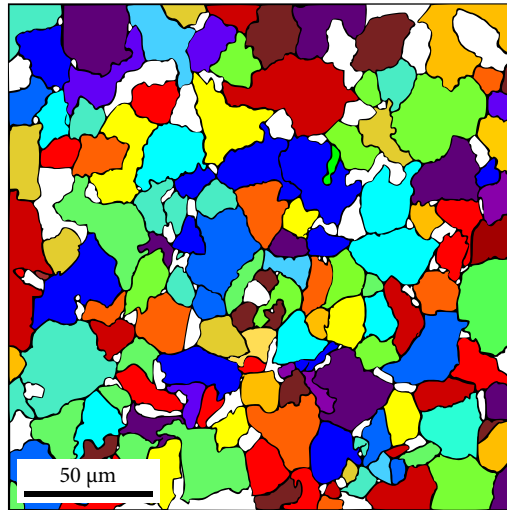
With the martensite transformation, also called displacive transformation, a vestige of the austenite grain boundary remains in the microstructure [18] and it can be revealed by etching [19]. However, it can be time consuming to find a successful etching to correctly identify the austenite grain boundaries. Instead, in [20], parent grains were successfully reconstructed by post-processing of EBSD data on the daughter grains. This technique was applied in this work to reconstruct the parent austenite grains in the cross section of quenched and self-tempered (QST) rebar from EBSD data obtained on martensite laths. The ARPGE software [21] was used for reconstruction of the parent grains.

### 4.2.1 Experimental analysis

EBSD analyses were performed on a polished cross section of QST rebar with 16 mm diameter. The cross section was prepared by mechanical grinding and polishing



(a)



(b)

**Figure 4.2** – Reconstruction of the austenite grains in the QST rebar: (a) Martensite grains obtained from EBSD analyses; (b) Reconstructed austenite grains determined from ARPGE software.

up to  $1\ \mu\text{m}$  followed by polishing with a Vibromet table containing non-crystalline colloidal silica for approximately 3.5 hours. EBSD analyses were then conducted using XL30-FEG Scanning Electron Microscopy (SEM) at 20 KV. The cross section was tilted at  $70^\circ$  in the SEM. EBSD map of the martensite grains was obtained from the surface edge to  $200\ \mu\text{m}$  towards the centre. A map size of  $200 \times 200\ \mu\text{m}$  was considered with a measurement step size of  $0.2\ \mu\text{m}$ .

EBSD map of the martensite laths is given in Fig. 4.2a. The orientation of the martensite grains is coded by colors representing the Euler angles; they are a set of three angles which describe the crystallographic orientation of grains relative to a reference (sample) coordinate system.

The austenite grains reconstructed by the ARPGE software are shown in Fig. 4.2b. The reconstruction was performed in three steps: identification of the martensite grains in the EBSD mapping; nucleation of austenite grains based on a selected orientation relationship (OR); growth of the austenite grains up to a defined tolerance angle [20]. The OR between austenite and martensite was the Greninger-Troiano (GT) relationship [18]. The white areas in the image (see Fig. 4.2b) correspond to the areas that could not be reconstructed by ARPGE. This may result from no indexed pixels in the EBSD map, martensite with ORs that are far from the GT-OR, martensite laths that could belong to two parent austenite grains and for which it was impossible to decide [20]. The color of each austenite grain represents the color of one martensite lath into this grain.

## 4.3 Short crack growth model

The short fatigue crack growth model is adapted from the three-zone micromechanical N-R model [10]. The interaction between crack and grain-phase boundary is characterized. It is assumed that when slip is initiated in a grain, the whole grain undergoes slip being blocked by the grain boundary. Slip propagates to the adjacent grain when the stress ahead of the plastic zone reaches a required value. This stress depends on the position of the crack tip to the grain boundary.

### 4.3.1 Grain structure

In N-R model, all grains are assumed to have equal sizes. In this work, the grain structure with different sizes was represented by Voronoi tessellation. Voronoi has been extensively used to reproduce the grain geometry of polycrystalline materials in short fatigue crack initiation models [15, 22].

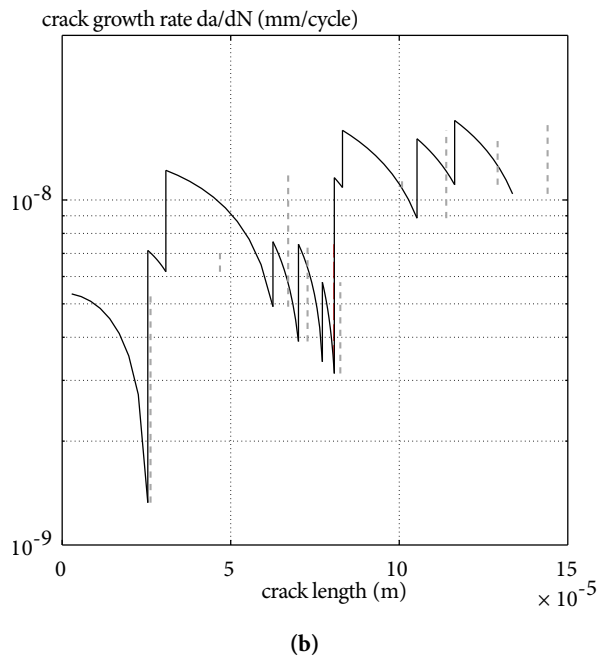
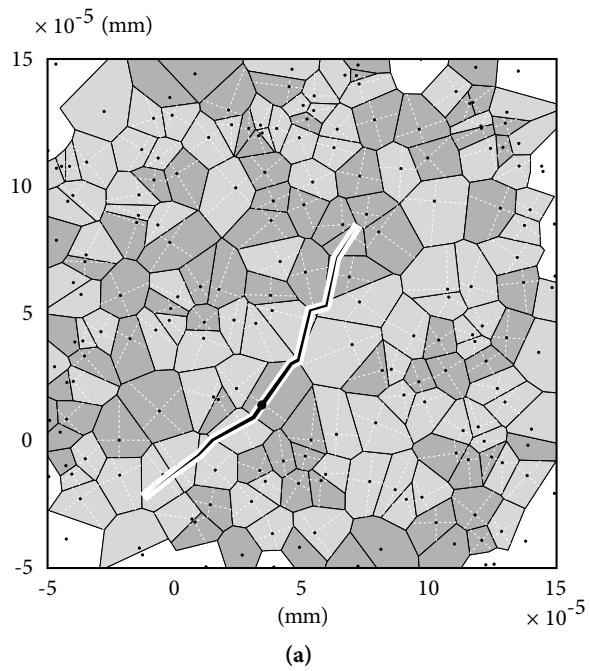


**Figure 4.3** – Example of a simulation result obtained in F-P with a crack length  $2a \approx 8D_m$  at  $N = 2 \times 10^6$  cycles: **(a)** Illustration of a surface short crack growth in ferrite (dark grey) and pearlite (light grey) grains represented by Voronoi cells; **(b)** Short crack growth rate as a function of the crack length.



Fig. 4.3a illustrates a short crack in F-P steel where the two phases, ferrite and pearlite, are modelled separately by Voronoi cells. The crack grows along a preferential slip direction randomly distributed in the model. In TM steel, Voronoi cells represent the parent austenite grains.

Voronoi tessellation is a cell structure generated from a random set of points as shown in Fig. 4.3a. Voronoi tessellation is a good approximation to represent a polycrystalline structure assuming that, in the crystallization process of a metal, all grains start to grow from random points and grow uniformly in all directions. The grains will then collide and a grain boundary will be created. In geometric aspects, the resulting grain structure would be a Voronoi.

In the Voronoi tessellation, the set of points is specified beforehand and each point will be enclosed by an area. Each Voronoi area (or cell) represents one grain. Voronoi tessellation was generated using MATLAB.

### Crack initiation in the first grain

Short fatigue cracks in steel specimen under uniaxial loading initiate along slip planes closer to the plane of maximum shear stress [24]. The angle between the slip plane and the applied load axis is close to  $45^\circ$  (mode II loading). Moreover, crack initiates in relatively coarse grains in steel [2]. Thus, it was assumed in the model that a crack initiates in a large grain along the slip plane closer to the plane of maximum shear stress. The crack always starts from a Voronoi point. To decide in which grain the crack will start, a compromise between slip size and direction was considered. A new length  $l_{crit}$  was calculated for each grain as given in Eq. 4.1:

$$l_{crit} = l \cos 2\theta \quad (4.1)$$

where  $l$  is the length of all slip planes passing through the Voronoi point and  $\theta$  is the angle between the slip plane and the plane of maximum shear stress. The crack initiates in the grain with maximum  $l_{crit}$ .

### Short crack growth

The schematic diagram given in Fig. 4.4 represents a half crack length  $a$  and its plastic zone  $c$  in a polycrystalline material. The crack grows in mode II loading and the applied shear stress component is assumed as  $\Delta\tau = \Delta\sigma/2$ , where  $\Delta\sigma$  is the applied uniaxial cyclic loading. In this model, a single crack is assumed to propagate until it reaches a given length of  $10D_{mean}$  ( $D_{mean}$  is the mean grain diameter) [2,25]

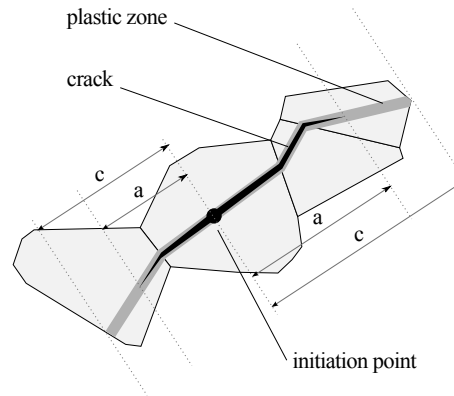


**Figure 4.4** – Schematic diagram of the crack with its plastic zones in the grains.

and the simulation is stopped.  $D_{mean}=20 \mu\text{m}$  as obtained from Fig. 4.2b using the Abram's Three Circle method [23].

The crack growth is calculated for each crack tip separately.

The crack grows at a rate of:

$$\frac{da}{dN} = f\phi \quad (4.2)$$

where  $N$  is the number of cycles,  $f$  is the fraction of dislocations ahead of the crack tip that contributes to the crack growth process and  $\phi$  is the crack tip plastic displacement.

The factor  $f$  varies between 0 and 1 and it depends on the applied stress: the smallest  $f$  values are obtained when the applied stress level approaches the fatigue limit [24]. It represents the degree of irreversibility of slip per cycle. In this work,  $f$  was assumed constant and equal to  $5.64 \times 10^{-4}$  since the scatter is analysed at constant stress amplitude and near the fatigue limit. This value was obtained from fatigue tests with low carbon steels subjected to uniaxial loading [24].

The plastic displacement  $\phi$  can be written as [26]:

$$\phi = \frac{2(1-\nu)\sqrt{1-n^2}\Delta\tau a}{\mu n} \quad (4.3)$$

where  $\nu$  is the Poisson's ratio and  $\mu$  is the shear modulus. The dimensionless parameter  $n = a/c$  defines the position of the crack tip relative to the grain boundary (see Fig. 4.4).

The crack growth rate as a function of the crack length obtained for F-P is given in Fig. 4.3b. The growth rate decreases as the crack approaches the grain boundary and then increases as the plastic zone propagates into the next grain. The dotted lines in Fig. 4.3b represent the plastic zone size at every propagation step in each grain.

The slip propagates from grain  $i$  to the neighbouring grain  $i + 1$  when  $n$  reaches a critical value  $n = n_c$ . This critical value  $n_c$  is given by [10]:

$$n_c^i = \cos \left[ \frac{\pi}{2} \left( \frac{\Delta\tau - \Delta\tau_{Li}}{2\tau_{fr}} \right) \right] \quad (4.4)$$

where  $\tau_{fr}$  is the "friction stress" which represents the resistance of the grain to the dislocation motion in the plastic zone.  $\Delta\tau_{Li}$  is the minimum stress required for slip propagation determined as [15]:

$$\Delta\tau_{Li} = \Delta\tau_{FL} \frac{m_i}{m_1} \sqrt{\frac{d_i}{2c_i}} \quad (4.5)$$

where  $\Delta\tau_{FL}$  is the fatigue limit,  $d_i$  is the mean of the crack length in each grain and  $m_i/m_1$  is the grain orientation ratio.  $\Delta\tau_{FL}$  represents a macroscopic property of the material and  $\Delta\tau_{Li}$  represents a condition for local plastic deformation at the microscopic level. The  $m_i/m_1$  ratio will be discussed in Section 4.3.2. The crack propagation stops if  $\Delta\tau$  is smaller than  $\Delta\tau_{Li}$ .

When a slip band starts in the next grain, the plastic zone spans this entire grain. Thus,  $n_c^i$  decreases to  $n_s^i$  expressed as:

$$n_s^{i+1} = \frac{c}{c_{i+1}} n_c^i \quad (4.6)$$

The number of cycles to propagate the crack in a grain can be obtained by integration of Eq. 5.3 which gives:

$$\Delta N_i = \frac{\mu}{f(1-\nu)\Delta\tau} (\sin^{-1} n_c^i - \sin^{-1} n_s^i) \quad (4.7)$$

The number of cycles  $N_{d1}$  and  $N_{d2}$  spent to propagate each crack tip separately are determined from the sum of  $\Delta N_i$ . The total number of cycles  $N_{Total}$ , when the crack length is equal to  $10D_{mean}$ , is given by:

$$N_{Total} = \max(N_{d1}, N_{d2}) \quad (4.8)$$

### 4.3.2 Grain orientation

An equation for the grain orientation ratio  $m_i/m_1$ , used in N-R model, was proposed by [27] and it is given as:

$$\frac{m_i}{m_1} = 1 + 2.07 \left[ \frac{2}{\pi} \tan^{-1}(0.522(i-1)2) \right]^{1.86} \quad (4.9)$$

where  $m_1$  is the orientation factor of the first grain and  $m_i$  is the orientation factor of successive grains. Eq. 4.9 was developed based on fatigue test results of mild steel and then applied for randomly oriented fcc materials.  $m_i/m_1$  increases progressively as the crack grows over several grains (see Fig. 4.5b) and  $m_{i \rightarrow \infty}$  tends to the average Taylor factor  $\bar{M}_T=3.07$ .

In reality, the short crack growth depends on the individual grain orientations. Since the objective of the present work is to analyse the scatter due to microstructural features including the grain orientation, a new equation  $m_i/m_1$  was proposed where this factor isn't forced to increase continuously with the crack length; it can decrease or increase as the crack propagates through successive grains which are more or less favourably oriented for slip. This allows to consider how the statistical variations of the grain orientation can affect the crack growth.

#### $m_i/m_1$ orientation ratio

The crack initiation in the first grain is governed by the stress required to sustain plastic deformation along the slip direction with the most favourable orientation, which results in the smallest orientation factor. This factor measures the deformation compatibility between the current crack and the slip direction in the adjacent grain. Since the need to maintain the compatibility between adjacent grains in this stage is small, the orientation factor is close to the Sachs factor for single crystal. This factor  $\bar{M}_S$  is equal to 2.24 (Sachs factor) for fcc and body centered cubic (bcc) materials [28].

With further crack propagation over several grains with different orientations (see Fig. 4.5a), the deformation compatibility between all these grains moves the orientation factor value from Sachs to Taylor type. When the crack becomes sufficiently large i.e., insensitive to the material microstructure, the orientation factor reaches a maximum value similar to the Taylor factor,  $m_{i \rightarrow \infty} = \bar{M}_T=3.07$  for randomly oriented fcc and bcc crystals [28].

Theoretically, the grain orientation ratio  $m_i/m_1$ , for  $m_1 = 2.24$  and  $m_{i \rightarrow \infty} = 3.07$ ,

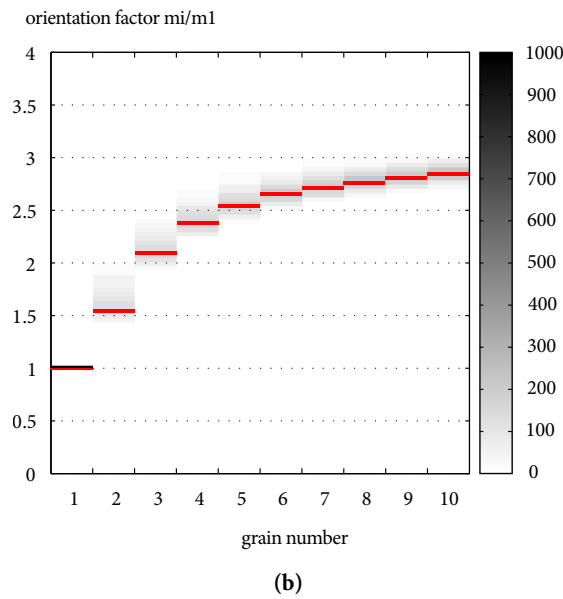
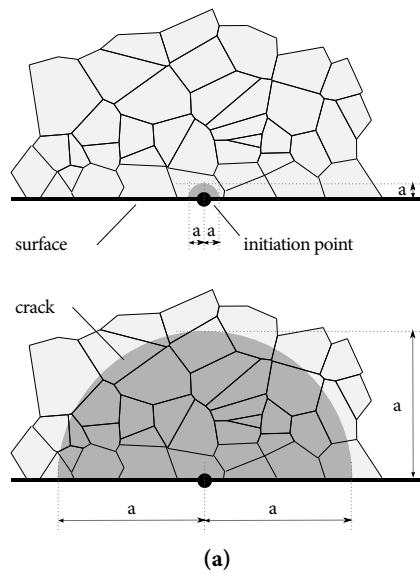


**Figure 4.5** – Illustration of a subsurface crack growth and variation of the grain orientation ratio  $m_i/m_1$ : **(a)** A crack length  $2a$  reaches 7 grains on the surface, the subsurface crack tip extends over  $\mathcal{N} = 14$  grains; **(b)** The graph represents the evolution of  $m_i/m_1$  scatter as the crack grows using Eq. 4.10; To illustrate this scatter, it was computed 1000  $m_i/m_1$  values for each step. The greyscale represents the amount of  $m_i/m_1$  with same values in a region. In the first step,  $m_i/m_1=1$  and there is no dispersion. In the second step, a higher dispersion is obtained compared to the 10th step when the dispersion decreases. The red lines represent the evolution of  $m_i/m_1$  obtained by Eq. 4.9.

varies between 1 and 1.4. However, as given in [29,30],  $m_{i \rightarrow \infty}/m_1$  can tend to a value of approximately 3 for mild steels. [29] suggests that this difference is attributed to crack closure effects; as the crack grows, it progressively increases to a steady peak value for large crack. Other factors such as microcrack initiation at several points and microcrack coalescence may also contribute to the value of 3.

Eq. 4.10 gives  $m_i/m_1$  which simulates the variance for steels with randomly oriented crystals:

$$\frac{m_i}{m_1} = 1 + 2(\Omega_i - 2.3) + 2.07 \left[ \frac{2}{\pi} \tan^{-1}(0.522(i-1)2) \right]^{1.86} \quad (4.10)$$

where  $\Omega_i$ , the average value of the grain orientations, is calculated as:

$$\Omega_i = \frac{1}{\mathfrak{N}} \sum_{j=1}^{\mathfrak{N}} \omega_j \quad (4.11)$$

$\mathfrak{N}$  represents the number of grains which contains the crack tip as shown in Fig.4.5a.

$$\omega_j = \min_{k=1 \text{ to } 12} \left( \frac{1}{(\mathbf{L} \cdot \mathbf{n}_k)(\mathbf{L} \cdot \mathbf{s}_k)} \right) \quad (4.12)$$

where  $\mathbf{L}$ ,  $\mathbf{n}_k$  and  $\mathbf{s}_k$  are unit vectors along the loading axis, slip plane normal and slip direction respectively. The  $k$  values represent the main slip system in bcc crystals: 6 slip planes and 2 slip directions in each plane.

Fig. 4.5b shows the  $m_i/m_1$  behaviour obtained for 1000 simulation runs at each step of the short crack growth. When the crack propagates in the first grain, the grain orientation ratio is 1. As the crack grows in few grains,  $m_i/m_1$  variation increases due to the higher dispersion in grain orientations. As more grains are incorporated to the crack growth, this variation decreases and  $m_i/m_1$  tends to the value of 3 when the crack length  $2a \approx 10D_m$ .

### 4.3.3 Material properties

The parameters used for ferrite, pearlite and martensite in the model are given in Table 4.1.

#### Ferrite and pearlite properties

Fatigue limit  $\Delta\sigma_{FL}$  of ferrite steels, i.e., with very low amount of pearlite, is approximately  $0.6\sigma_u$  [31], where  $\sigma_u$  is the tensile strength. This results in  $\Delta\sigma_{FL}=260$

**Table 4.1** – Material properties used in the model.

Parameters	Ferrite	Pearlite	Martensite
$\tau_{fr}$ (MPa)	70	134	142
$\Delta\sigma_{FL}$ (MPa)	260	385	368
$\mu$ (GPa) [40]	82	82	79
$\nu$ [40]	0.28	0.28	0.29

MPa [32].  $\tau_{fr}$  for ferrite is 70 MPa as given in [33].

Fatigue limit  $\Delta\sigma_{FL}$  of fully pearlite steels is approximately  $0.4\sigma_u$  [31]. The value of 385 MPa was obtained [34] as shown in Table 4.1. The  $\tau_{fr}$  value of 134 MPa is given in [35]. The area fraction of pearlite for hot rolled (HR) rebars was found to vary from approximately 15 to 55% [36, 37]. This variation was considered in the model.

Since in fatigue tests with F-P steels, cracks usually start in the softer ferrite grain [24, 38, 39], the crack was assumed always to start in a ferrite grain in the model.

#### Tempered martensite properties

Fatigue limit  $\Delta\sigma_{FL}$  of TM steels was found to be approximately  $0.6\sigma_u$  [31]. Since  $\sigma_u=613$  MPa for the TM steel studied in this work,  $\Delta\sigma_{FL}$  was then determined as approximately 368 MPa (see Table 4.1). The  $\tau_{fr}$  values given in [41, 42] for TM steels varies from approximately  $0.25$  to  $0.30\sigma_y$  with  $\sigma_y$  being the yield strength.  $\tau_{fr}=142$  MPa was calculated from  $0.275\sigma_y$  with  $\sigma_y=518$  MPa for the studied TM steel.

## 4.4 Results and Discussion

Fig. 4.6 shows the scatter obtained in the F-P model for different area fractions of pearlite i.e., varying approximately between 15 and 55%, as found in HR rebars [36], [37]. The scatter in F-P model is affected by the presence of two phases and different area fractions of ferrite and pearlite. As the crack grows into pearlite from softer ferrite phase, the crack growth rate decreases at phase interface. Since pearlite is a harder microstructure, the boundary between two phases tended to impede the crack propagation. Similar crack behaviour was experimentally observed in fatigue tests with F-P steels [38]. As the area fraction of ferrite varies considerably between HR rebars, the duration of fatigue crack initiation was affected with this area variation and consequently, the scatter at the analysed stress level. Smaller area fraction

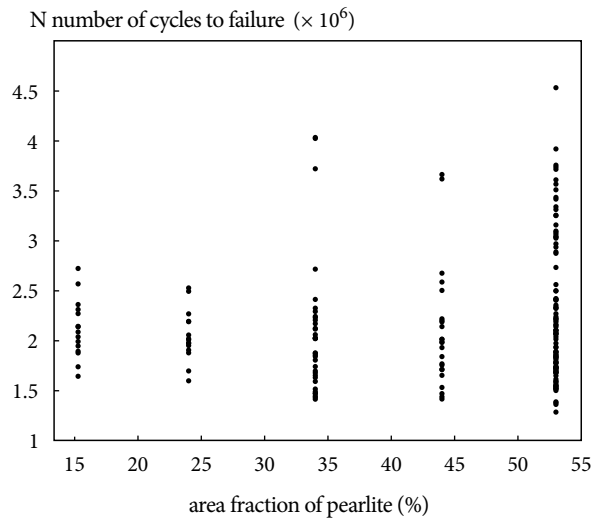


**Figure 4.6** – Scatter obtained for different area fractions % of pearlite in the F-P model.

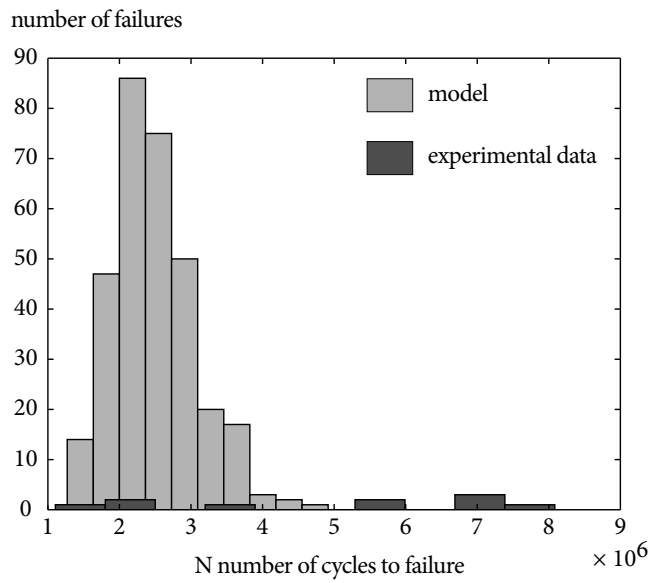
of pearlite, for example, tended to decrease scatter since the crack grows predominantly in one phase i.e., in ferrite grains.

Figs. 4.7a and 4.7b show the scatter determined from simulations of the short crack growth in F-P (with 53% of pearlite) and TM steels. The model results were compared to experimental data including rebars with diameter  $d \leq 16$  mm and tested at stress-ratio between 0 and 0.2 as given in [43–47]. Model and experimental results given in Figs. 4.7a and 4.7b include only failure data points. The model results include the influence of microstructural features on the scatter in the fatigue crack initiation phase. This phase includes short crack propagation to a maximum length of 0.2 mm. The long crack propagation phase will be treated in another paper.

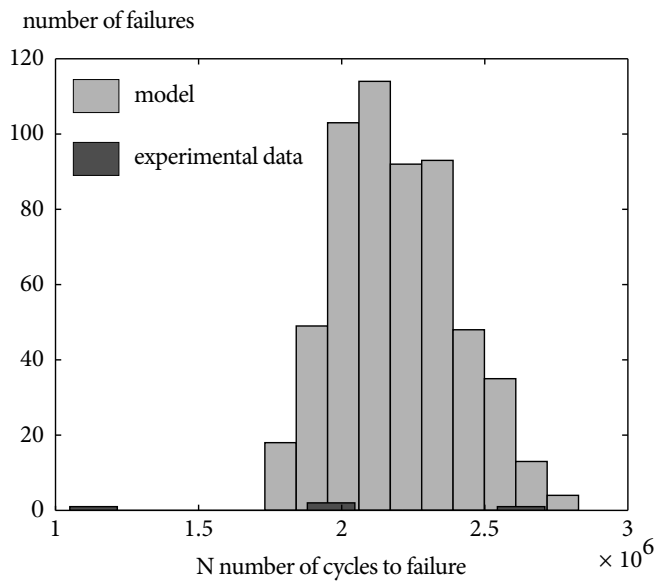
The model data were generated from 1000 simulations run at 24 MPa above the fatigue limit of both F-P and TM steels. The scatter at this stress level was compared to the scatter found in HR-CW and QST rebars with similar local conditions. The value of 24 MPa was considered in the simulations since 1) The smallest  $f$  value experimentally given in [24] was determined for a stress range at 24 MPa above the fatigue limit of the material; 2) There were no or few experimental data for HR-CW and, especially for QST rebars, at lower stress ranges and with the same test conditions as considered in this work.

The experimental data in Fig. 4.7a include HR and CW rebars of low and medium Carbon content with different area fractions of pearlite. Information on the crystallographic texture of HR, CW and QST rebars isn't provided in the literature. Crystal-





(a)



(b)

**Figure 4.7** – Distribution of failures points obtained in the model and experimental data: (a) For F-P model with an area fraction of 53% of pearlite and HR-CW rebars [43,44]; (b) For TM model and QST rebars [45-47].

lographic texture is defined as the grain (crystal) orientation in a specimen. In [48], nearly random texture was found on the surface of hot rolled low-alloyed steels with bcc structure; during hot rolling, the steel undergoes several passes where the texture is randomized by dynamic recrystallization and phase transformation from austenite to ferrite. Randomly oriented grains were then assumed for F-P and TM in the model as a first approximation.

Fig. 4.7b shows the scatter of failure data obtained from the model and QST rebar test results. With the model, higher scatter was obtained in F-P compared to TM which is in agreement to what has been observed in fatigue tests with HR, CW and QST rebars. In [49], for example, QST rebars showed smaller scatter compared to HR and CW rebars. In [45], small scatter was observed in fatigue tests with QST rebars near the fatigue limit. The fatigue behaviour of these rebars was considered essentially as a function of the surface layer of martensite.

Moreover, as shown in Figs. 4.7a and 4.7b, the scatter determined in both F-P and TM is smaller than the scatter observed in experimental data; it represents about 50% of the scatter from fatigue tests. This difference between model and experimental results may be influenced by stress concentrators on the rebar surface, such as roughness and the presence of the ribs, giving rise to local plastic deformation and affecting fatigue crack propagation. [50], for example, suggests that scatter near the fatigue limit of QST rebars may result from variations in stress concentrations arising from ribs as well as surface microstructural features.

## 4.5 Conclusion

N-R model including grain structure with different sizes and grain orientation variations was used to simulate the propagation of a single fatigue short crack in ferrite-pearlite and tempered martensite steels within a Monte-Carlo framework. The scatter determined above but near the fatigue limit was compared to the scatter found on experimental data of rebars. Grain size variation using Voronoi tessellation, randomly oriented grains and different phases were considered in the analyses. This work suggests that:

Martensitic microstructure contributes to the scatter reduction in rebars at stress range levels above the fatigue limit compared to ferrite-pearlite. The grain and phase boundaries as well as different area fractions of ferrite-pearlite affects the short crack growth rate and thus increase the scatter in the fatigue crack initiation period.

The microstructure on the rebar surface is responsible for about half of the scat-

ter found in fatigue tests with rebars used as reference. Since fatigue crack initiation is mainly a surface phenomena, it is likely that surface roughness and ribs may also contribute to the dispersion in the tests.

For further studies, it is recommended to consider:

- More experimental data, especially on QST rebars, is needed near the fatigue limit. Few data were found in the literature with similar test conditions as considered in this work.
- The crystallographic orientation of hot rolled, cold worked and quenched and self-tempered rebars, considered in this work, should be confirmed. Random texture was assumed in the model based on texture analyses on hot rolled bcc steels found in the literature.
- For future simulations, it is suggested to use the formulation proposed by Vallellano et al. [51] for unequal grain sizes. N-R model used in this paper is strictly applicable to symmetric conditions including equal grain sizes. Beside,
- In fatigue tests with steel, multiple short cracks can grow simultaneously and form a main crack that propagates until failure. However, in this work, it was assumed that only a single crack initiates and grows until the end of initiation life, defined as a crack size of 10 grains. Therefore, no macrocrack growth and crack coalescence, which can occur in reality, were considered in the model, although many initiation spots can occur at the different ribs and only the worst combination leads to a dominating crack and failure.

## 4.6 Acknowledgements

We are grateful to Dr. Emmanuelle Courjault from the Computational Materials Laboratory (LSMX) at EPFL for the EBSD analysis. We are also grateful also to Dr. Cayron from the Nanocharacterisation group of LITEN at CEA-Grenoble for the parent austenite reconstruction.

---

## *Bibliography*

---

- [1] Schijve, J. (2001). *Fatigue of structures and materials*. Dordrecht: Kluwer Academic, p. 9.
- [2] Tokaji, K., & Ogawa, T. (1992). The growth behaviour of microstructurally small fatigue cracks in metals. *Short fatigue cracks, ESIS*, 13, 85-99.
- [3] Taira, S., Tanaka, K., & Hoshina, M. (1979). Grain size effect on crack nucleation and growth in long-life fatigue of low-carbon steel. *ASTM STP*, 675, 135-173.
- [4] Milne, I., Ritchie, R. O., & Karahaloo, B. L. (2003). *Comprehensive structural integrity: Cyclic loading and fatigue*. Elsevier, 4, 129-154.
- [5] Ray, K. K., Narasaiah, N., & Sivakumar, R. (2004). Studies on short fatigue crack growth behavior of a plain carbon steel using a new specimen configuration. *Materials Science and Engineering: A*, 372(1), 81-90.
- [6] Navarro, A., & Rios, E. (1987). A model for short fatigue crack propagation with an interpretation of the short-long crack transition. *Fatigue & Fracture of Engineering Materials & Structures*, 10(2), 169-186.
- [7] Navarro, A., & De Los Rios, E. R. (1988). Short and long fatigue crack growth: A unified model. *Philosophical Magazine A*, 57(1), 15-36.
- [8] Bilby, B. A., Cottrell, A. H., & Swinden, K. H. (1963). The spread of plastic yield from a notch. *Proceedings of the Royal Society of London. Series A. Mathematical and Physical Sciences*, 272(1350), 304-314.
- [9] Taira, S., Tanaka, K., & Nakai, Y. (1978). A model of crack-tip slip band blocked by grain boundary. *Mechanics Research Communications*, 5(6), 375-381.

- [10] Navarro, A., & De Los Rios, E. R. (1992). Fatigue crack growth modelling by successive blocking of dislocations. *Proceedings of the Royal Society of London. Series A: Mathematical and Physical Sciences*, 437(1900), 375-390.
- [11] De Los Rios, E. R., & Navarro, A. (1990). Considerations of grain orientation and work hardening on short-fatigue-crack modelling. *Philosophical Magazine A*, 61(3), 435-449.
- [12] Turnbull, A., & De Los Rios, E. R. (1995). Predicting fatigue life in commercially pure aluminium using a short crack growth model. *Fatigue & Fracture of Engineering Materials & Structures*, 18(12), 1469-1481.
- [13] Wilkinson, A. J. (2001). Modelling the effects of texture on the statistics of stage I fatigue crack growth. *Philosophical Magazine A*, 81(4), 841-855.
- [14] Chaves, V., Navarro, A., Madrigal, C., & Vallellano, C. (2014). Calculating crack initiation directions for in-phase biaxial fatigue loading. *International Journal of Fatigue*, 58, 166-171.
- [15] Andersson, J. (2005). The influence of grain size variation on metal fatigue. *International Journal of Fatigue*, 27(8), 847-852.
- [16] Vallellano, C., Vazquez, J., Navarro, A., & Dominguez, J. (2009). A micromechanical model for small fatigue crack growth: An approach based on two threshold conditions. *Fatigue & Fracture of Engineering Materials & Structures*, 32(6), 515-524.
- [17] Davis, J. R. (2002). *Surface hardening of steels: Understanding the basics*. ASM international.
- [18] Bhadeshia, H., & Honeycombe, R. (2006). *Steels: Microstructure and properties*. Butterworth-Heinemann, pp. 97-98.
- [19] Bramfitt, B. L., & Benschoter, A. O. (2002). *Metallographer's guide: Practices and procedures for iron and steels*, ASM International.
- [20] Cayron, C., Artaud, B., & Briottet, L. (2006). Reconstruction of parent grains from EBSD data. *Materials Characterization*, 57(4), 386-401.
- [21] Cayron, C. (2007). ARPGE: a computer program to automatically reconstruct the parent grains from electron backscatter diffraction data. *Journal of Applied Crystallography*, 40(6), 1183-1188.

- [22] Brückner-Foit, A., & Huang, X. (2006). Numerical simulation of micro-crack initiation of martensitic steel under fatigue loading. *International Journal of Fatigue*, 28(9), 963-971.
- [23] E112-12. (2012) Standard test methods for determining average grain size.
- [24] Hussain, K., De Los Rios, E. R., & Navarro, A. (1993). A two-stage micromechanics model for short fatigue cracks. *Engineering Fracture Mechanics*, 44(3), 425-436.
- [25] Tokaji, K., Ogawa, T., Harada, Y., & Ando, Z. (1986). Limitations of linear elastic fracture mechanics in respect of small fatigue cracks and microstructure. *Fatigue & Fracture of Engineering Materials & Structures*, 9(1), 1-14.
- [26] Navarro, A., & Rios, E. R. (1988). A microstructurally short fatigue crack growth equation. *Fatigue & Fracture of Engineering Materials & Structures*, 11(5), 383-396.
- [27] De Los Rios, E. R., Xin, X. J., & Navarro, A. (1994). Modelling microstructurally sensitive fatigue short crack growth. *Proceedings of the Royal Society of London. Series A: Mathematical and Physical Sciences*, 447(1929), 111-134.
- [28] Shetty, M. (2013). *Dislocations and mechanical behaviour of materials*. PHI Learning Pvt.
- [29] Vallengano, C., Navarro, A., García-Lomas, F. J., & Domínguez, J. (2008). On the estimation of microstructural effects in the near-threshold fatigue of small cracks. *The Journal of Strain Analysis for Engineering Design*, 43(5), 337-347.
- [30] Kuroda, M., & Marrow, T. J. (2008). Modelling the effects of surface finish on fatigue limit in austenitic stainless steels. *Fatigue & Fracture of Engineering Materials & Structures*, 31(7), 581-598.
- [31] Boyer, H. E. (Ed.). (1985). *Atlas of fatigue curves*. ASM International, p. 31.
- [32] Tokaji, K., Ogawa, T., & Aoki, T. (1990). Small fatigue crack growth in a low carbon steel under tension-compression and pulsating-tension loading. *Fatigue & Fracture of Engineering Materials & Structures*, 13(1), 31-39.
- [33] Gladman, T., McIvor, I. D., & Pickering, E. B. (1972). Some aspects of the structure — property relationships in high-carbon ferrite-pearlite steels. *Journal of the Iron and Steel Institute*, 210, 916-930.

- [34] Dollar, M., Bernstein, I. M., & Thompson, A. W. (1988). Influence of deformation substructure on flow and fracture of fully pearlitic steel. *Acta Metallurgica*, 36(2), 311-320.
- [35] Elwazri, A. M., Wanjara, P., & Yue, S. (2005). The effect of microstructural characteristics of pearlite on the mechanical properties of hypereutectoid steel. *Materials Science and Engineering: A*, 404(1), 91-98.
- [36] Jhamb, I. C., & Mac Gregor, J. G. (1974). Effect of surface characteristics on fatigue strength of reinforcing steel. *ACI Special Publication*, 41-7, 139-168.
- [37] Kelestemur, O., Kelestemur, M. H., & Yildiz, S. (2009). Improvement of mechanical properties of reinforcing steel used in the reinforced concrete structures. *Journal of Iron and Steel Research, International*, 16(3), 55-63.
- [38] Tokaji, K., Ogawa, T., & Osako, S. (1988). The growth of microstructurally small fatigue cracks in a ferritic-pearlitic steel. *Fatigue & Fracture of Engineering Materials & Structures*, 11(5), 331-342.
- [39] Tokaji, K., Ogawa, T., & Harada, Y. (1986). The growth of small fatigue cracks in a low carbon steel; the effect of microstructure and limitations of linear elastic fracture mechanics. *Fatigue & Fracture of Engineering Materials & Structures*, 9(3), 205-217.
- [40] Kim, S. A., & Johnson, W. L. (2007). Elastic constants and internal friction of martensitic steel, ferritic-pearlitic steel, and  $\alpha$ -iron. *Materials Science and Engineering: A*, 452, p. 636.
- [41] Daigne, J., Guttman, M., & Naylor, J. P. (1982). The influence of lath boundaries and carbide distribution on the yield strength of 0.4% C tempered martensitic steels. *Materials Science and Engineering*, 56(1), 1-10.
- [42] Malik, L., & Lund, J. A. (1972). A study of strengthening mechanisms in tempered martensite from a medium carbon steel. *Metallurgical Transactions*, 3(6), 1403-1406.
- [43] Tilly, G. P. (1979). Fatigue of steel reinforcement bars in concrete: a review. *Fatigue & Fracture of Engineering Materials & Structures*, 2(3), 251-268.
- [44] Tilly, G. P. (1984). Fatigue testing and performance of steel reinforcement bars. *Matériaux et Construction*, 17(1), 43-49.

- [45] Zheng, H., & Abel, A. A. (1999). Fatigue properties of reinforcing steel produced by Tempcore process. *Journal of Materials in Civil Engineering*, 11(2), 158-165.
- [46] Donnell, M. J., Spencer, W., & Abel, A. (1986). Fatigue of Tempcore reinforcing bars - the effect of galvanizing. In *Australasian Conference on the Mechanics of Structures and Materials*, 10th, 1986, Adelaide, Australia (Volume 2).
- [47] Rocha, M., Michel, S., Brühwiler, E., & Nussbaumer A. Very high cycle fatigue tests of quenched and self-tempered steel reinforcement bars.
- [48] Raabe, D., & Lücke, K. (1992). Texture and microstructure of hot rolled steel. *Scripta Metallurgica et Materialia*, 26(8), 1221-1226.
- [49] Fehlmann P. (2012). Zur Ermüdung von Stahlbetonbrücken. ETH thesis, n° 20231, Zürich, pp. 46-47.
- [50] Zheng, H., & Abel, A. (1998). Stress concentration and fatigue of profiled reinforcing steels. *International Journal of Fatigue*, 20(10), 767-773.
- [51] Vallellano, C., Navarro, A., & Domínguez, J. (2002). Compact formulation for modelling cracks in infinite solids using distributed dislocations. *Philosophical magazine A*, 82(1), 81-92.





BIBLIOGRAPHY

## Fatigue behaviour prediction of steel reinforcement bars using an adapted Navarro and De Los Rios model

— Marina Rocha, Eugen Brühwiler, Alain Nussbaumer

**Abstract:** *Fatigue cracks tend to initiate on the rebar surface and therefore, the surface conditions may control their fatigue behaviour. This study investigates the influence of surface microstructure and roughness dispersion on the scatter and fatigue life of hot rolled (HR)-cold worked (CW) and quenched and self-tempered (QST) rebars. The stochastic nature of the fatigue life is mainly affected by the scatter of short cracks in the crack initiation phase. A model adapted from Navarro and De Los Rios was developed to predict the crack initiation, including short crack growth, and long crack propagation phases. The stress concentration factor determined near the ribs was considered as a constant parameter. The model results were compared to experimental data from the literature.*

**Keywords:** Steel reinforcement bars; Crack growth model; Surface conditions; Scatter; Fatigue behaviour prediction.



## Contents

<b>5.1</b>	<b>Introduction</b>	<b>91</b>
<b>5.2</b>	<b>Crack growth model</b>	<b>92</b>
5.2.1	Threshold for short crack growth	94
5.2.2	$f$ function	95
<b>5.3</b>	<b>Surface roughness</b>	<b>95</b>
5.3.1	3D surface roughness profile	96
5.3.2	Fatigue stress concentration factor	98
<b>5.4</b>	<b>Stress concentration factor-rib geometry</b>	<b>99</b>
<b>5.5</b>	<b>Results and discussion</b>	<b>100</b>
<b>5.6</b>	<b>Conclusion</b>	<b>102</b>

### 5.1 Introduction

Fatigue life of structural metallic components until failure can be split into initiation and propagation periods. Initiation is generally defined as the smallest crack that can be detected by non-destructive inspection technique. Propagation follows and in a cracked component, Paris' law is usually applied for fatigue life assessment describing the growth rate from the detected initial-crack. In reinforced concrete elements, where crack detection is impracticable on the embedded steel reinforcement bars (rebars), S-N curve-method is used for fatigue life prediction. However, this method doesn't provide any information on the presence, or not, of fatigue cracks. Paris' law is only applied when a more detailed investigation is required with a long or conservative initial crack size being assumed in the calculations.

Fatigue strength of metallic materials may be controlled by the short crack growth behaviour as a consequence of the strength offered by the barriers, such as grain-phase boundaries, to the plastic slip. Short cracks can behave significantly different from long cracks predicted by Paris' law [1]. These cracks may propagate during a large fraction of the component life and therefore, Paris' law would fail to predict their fatigue life.

Fatigue cracks tend to initiate at stress raisers on the material surface. As a consequence, the conditions of the surface layer such as roughness and geometrical features is significant for the fatigue behaviour of the material. These stress raisers

are introduced in the fabrication process and they can be, in some cases, essential to a component perform its function.

Surface conditions affect primarily the crack initiation period, especially near the fatigue limit. Initiation, in this case, includes crack nucleation and short crack growth controlled by material barriers. Nucleation can be dependent on local surface irregularities which vary from specimen to specimen and can affect the duration of the crack initiation period. As a consequence, more scatter is found at high number of stress cycles [2].

The stress concentration on a surface irregularity (notch) is usually quantified in terms of stress concentration factor  $K$ . As  $K$  increases, the stress required to initiate a crack at the notch decreases. It has been observed that the short crack growth rate at the notch root of steels, for example, can increase with the increase of  $K$  values although these cracks can arrest or become non-propagating at the notch root after overcoming few barriers [3, 4]. This suggests that the initiation of the crack itself isn't the key point in the fatigue behaviour of notched steels but rather the capacity of the (short) crack to propagate over successive microstructural barriers.

In this work, the fatigue behaviour of hot rolled (HR), cold worked (CW) and quenched and self-tempered (QST) rebars is investigated using an adapted Navarro and De Los Rios (N-R) model as given in [2]. The model includes the influence of the microstructure as well as the  $K$  dispersion obtained from surface roughness analysis. The  $K$  value determined for the rib geometry at the critical zone i.e., from where fatigue cracks usually initiate, is considered as a constant. The results are compared to experimental data for HR-CW and QST rebars.

## 5.2 Crack growth model

The algorithm used in this work is adapted from the N-R model described in [2] for plain specimens and represented in Fig. 5.1. The present model includes the roughness dispersion determined on the rebar surface as well as the long crack propagation phase to the N-R model [2] to investigate the fatigue behaviour of HR-CW and QST rebars.

As shown in Fig. 5.1, the crack initiation phase consists of a stochastic process which includes the dispersion inherent to:

- grain size variation;
- grain orientation ratio (for randomly oriented grains);

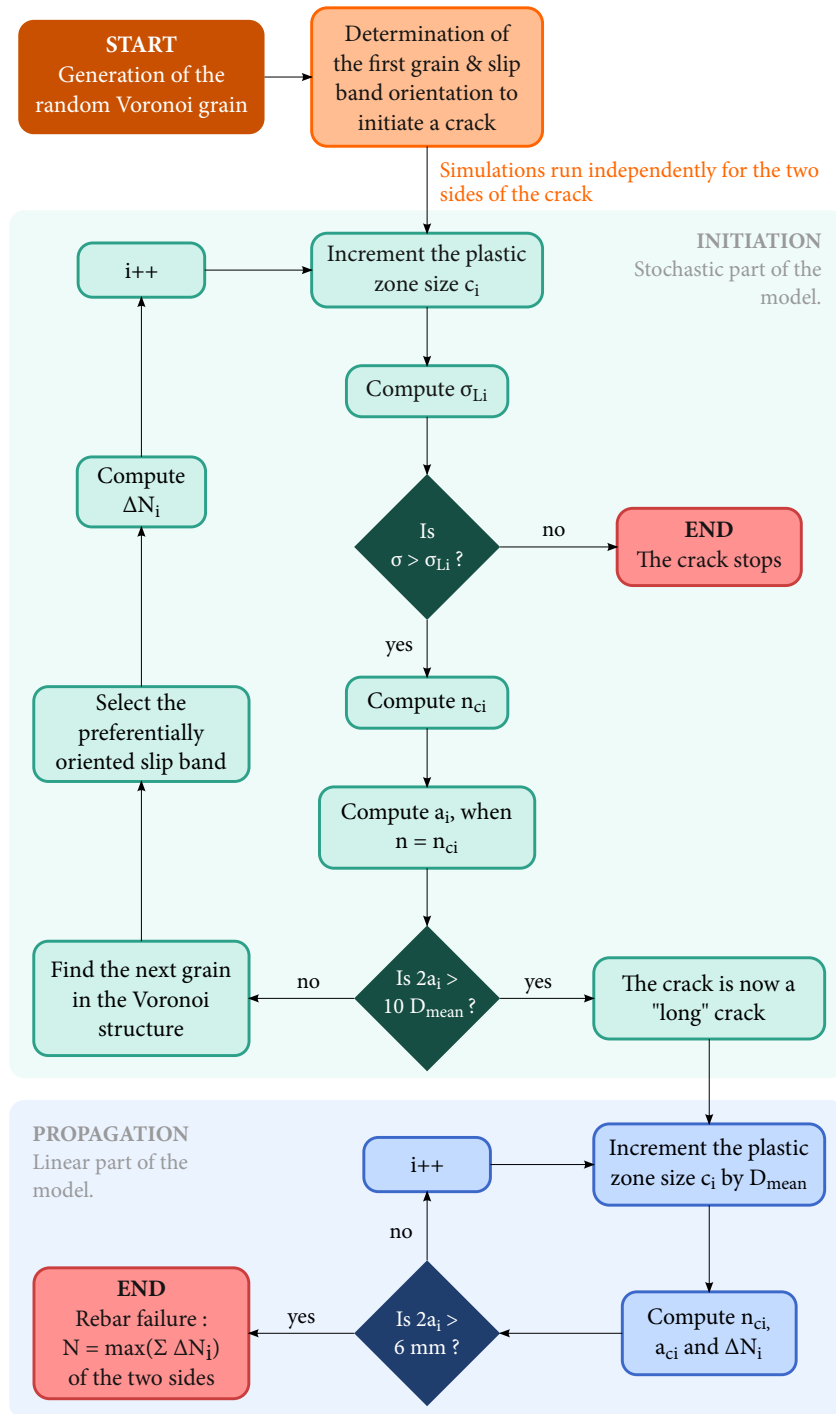


Figure 5.1 – Flowchart of the adapted N-R model used in this work.

- different phases (ferrite-pearlite and martensite);
- stress concentration factors determined from surface roughness analysis.

In the long crack propagation phase, there is no dispersion of the microstructural features and therefore, it is assumed equal grain sizes and consequently equal increments of the plastic zone. The plastic zone size is negligible compared to the crack size.

### 5.2.1 Threshold for short crack growth

The short crack growth model for plain specimens [2] defines the condition to activate a plastic slip in terms of applied stress level and crack size; short cracks are unable to overcome microstructural barriers, such as grain-phase boundaries, at stress levels below the fatigue limit  $\Delta\tau_{FL}$ . This interpretation is in agreement to what has been observed by [3,5].

The applied stress  $\Delta\tau_{Li}$  required to propagate a short crack over  $i$  grains is given by [2]:

$$\Delta\tau_{Li} = \Delta\tau_{FL} \frac{m_i}{m_1} \sqrt{\frac{d_i}{2c_i}} \quad (5.1)$$

where  $\Delta\tau_{FL}$  is the fatigue limit of the plain specimen,  $d_i$  is the mean of the crack length in each grain,  $c_i$  is the position of the plastic zone and  $m_i/m_1$  is the grain orientation ratio.

When irregularities (notches) are present on the specimen surface, the crack and its plastic zone growth are controlled by the resistance offered by the grain boundary as it occurs in plain specimens. However, the main difference in the short crack growth behaviour between plain and notched cases is the stress gradient related to the notch: the driving stress can vary significantly as the crack confronts each grain boundary. Depending on the applied stress level and the severity of the stress gradient, a short crack may grow over few grains and then stop as the stress level decreases. The crack propagates to the next grain only if the plastic slip is activated beyond the grain boundary.

The applied stress  $\Delta\tau_{Li}^{notch}$  required for the crack to overcome the  $i$ -th barrier in a notched specimen is given as [6]:

$$\Delta\tau_{Li}^{notch} = \Delta\tau_{Li} K_f \quad (5.2)$$

where  $K_f$  is the fatigue stress concentration factor.  $K_f$  values determined from sur-

face roughness analysis on QST rebar is discussed in Section 5.3.2.

### 5.2.2 $f$ function

The crack propagation rate  $da/dN$  in the N-R model depends on the  $f$  function and it is given by:

$$\frac{da}{dN} = f\phi \quad (5.3)$$

where  $f$  represents the fraction of dislocations ahead of the crack tip that contributes to the crack growth process.  $N$  is the number of cycles and  $\phi$  is the crack tip plastic displacement. Since  $f$  varies as a function of the applied stress (it decreases as the applied stress level decreases) and the fatigue behaviour of rebars in this work is analysed at different stress levels,  $f$  functions were then proposed for ferrite, pearlite and martensite depending on the applied stress.

In the N-R model,  $f$  is constant at each stress level and is always obtained experimentally. In this work, three equations for the different phases were deduced on the experimental data with low Carbon steel under uniaxial loading as given in [7]. Depending on the fatigue limit of each phase, it was then assumed the same growth rate as found in the literature.

$f$  functions determined for ferrite, pearlite and martensite are given in Eqs. 5.4, 5.5 and 5.6 respectively:

$$f = 4.89 \times 10^{-16} \Delta\tau^{5.49} \quad (5.4)$$

$$f = 1.93 \times 10^{-20} \Delta\tau^{7.03} \quad (5.5)$$

$$f = 8.30 \times 10^{-20} \Delta\tau^{6.81} \quad (5.6)$$

## 5.3 Surface roughness

Surface roughness is usually associated with the geometric topography of material surface. It depends greatly on the production technique where each fabrication process generates its own characteristic surface. Surface roughness manifests as a sequence of micronotches from where slip bands can emerge. The stress concentration arising from these micronotches may accelerate the fatigue crack nucleation



and lead to early short crack growth. In rebars, these micronotches are on the free surface and mainly concentrated near the ribs (see Fig. 5.2).

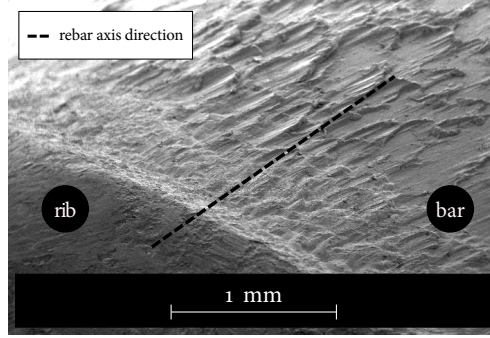


Figure 5.2 – Roughness on the surface of a QST rebar near the rib.

### 5.3.1 3D surface roughness profile

A photometric stereo technique applied to XL30-FEG Scanning Electron Microscopy (SEM) was used to reconstruct the 3D surface roughness profile of the QST rebar with diameter of 16 mm. An area of  $1500 \times 1500 \mu\text{m}$ , close to a transversal rib, was considered in the analysis. Four images were captured from the same area. The 3D surface reconstruction was then obtained by post-processing of all images based on photometric stereo technique. Fig. 5.3 shows the 3D surface roughness profile reconstructed by photometric stereo technique using SEM images.

The effect of the surface roughness on the fatigue strength of rebars can be obtained as a function of  $R_a$ ,  $R_y$  and  $R_z$  parameters. They were obtained from the roughness profile height distribution ( $z$ ) recorded over a length ( $L$ ) and calculated as [8]:

$$R_a = \frac{1}{L} \int_0^L |z| dx \quad (5.7)$$

where  $R_a$  is the average deviation in surface height from the roughness profile mean line.

$$R_y = |z_{max} - z_{min}| \quad (5.8)$$

$R_y$  is the maximum peak-to-valley height roughness over the evaluated length.

$$R_z = \frac{1}{5} \left( \sum_{r=1}^5 (z_r)_{max} + \sum_{s=1}^5 |(z_s)_{min}| \right) \quad (5.9)$$

$R_z$  is the ten-point roughness i.e., the average height from the five highest peaks

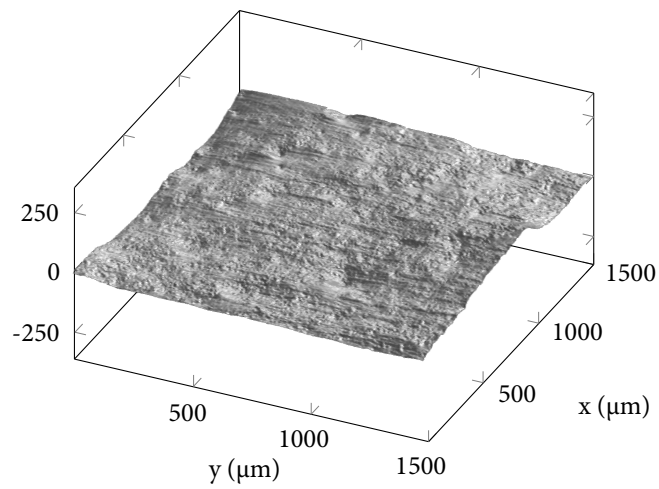


**Figure 5.3** – 3D profile of the surface roughness of the QST rebar obtained by photometric stereo technique.

and five lowest valleys. Fig. 5.4 illustrates a surface roughness profile determined for the QST rebar over a length  $L=1500 \mu\text{m}$ . The dash line represents the mean of the roughness profile. The circles correspond to the five highest peaks and five lowest valleys considered in the  $R_z$  calculations.

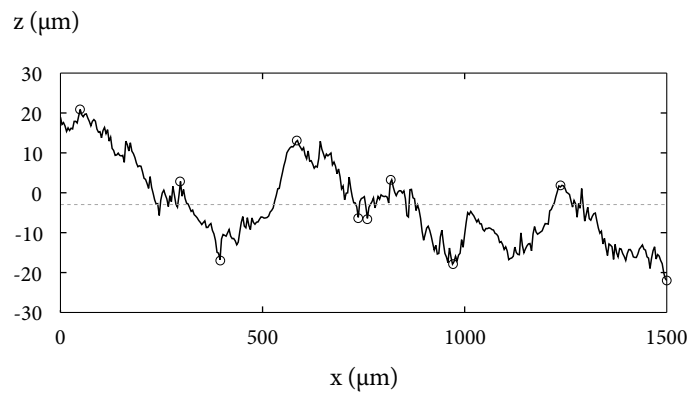


**Figure 5.4** – Illustration of a surface roughness profile obtained for the QST rebar and the surface roughness parameters.

### 5.3.2 Fatigue stress concentration factor

The fatigue stress concentration factor  $K_f$ , imposed by the surface roughness and considered in the model, was calculated as [8]:

$$K_f = 1 + q \left[ n \left( \frac{R_a}{\bar{\rho}} \right) \left( \frac{R_y}{R_z} \right) - 1 \right] \quad (5.10)$$

where  $q$  is the notch sensitivity,  $n=2$  for uniform tension stress and  $\bar{\rho}$  is the effective profile valley radius. It represents the average radius obtained from the dominant profile valleys. The parameter  $q$  is determined as:

$$q = \frac{1}{(1 + \gamma/\bar{\rho})} \quad (5.11)$$

where  $\gamma$  is a material constant and defined as a function of the ultimate tensile strength  $\sigma_u$  for steels [8]:

$$\gamma = 0.025 \left( \frac{2070 \text{ MPa}}{\sigma_u} \right)^{1.8} \quad (5.12)$$

Since there are no studies in the literature on the surface roughness profile of rebars, the  $K_f$  values determined in this work for the QST rebar were applied in the model for HR-CW rebars. The mean  $\sigma_u$  of QST rebars [9] was then used in the calculations of  $K_f$ . For more accurate results, it is suggested to determine the roughness profile of HR-CW rebars and other QST rebars.

The  $K_f$  values, calculated according to Eq. 5.10, were determined from the 3D surface roughness profile given in Fig. 5.3. The  $K_f$  dispersion is shown in Fig. 5.5 with a mean value of 1.3.

The surface roughness of rebars is affected by the introduction of the ribs during the fabrication process; a higher surface roughness is observed near the transversal ribs (see Fig. 5.2). The material properties considered in the model are based on a literature review and they include implicitly unknown surface roughness  $K_f$  greater than 1. The use of a mean  $K_f$  value equal to 1.3 in the model could therefore underestimate the fatigue life predictions. For this reason, it is proposed to replace the mean  $K_f = 1.3$  by 1, but keeping the scatter. The distribution of the  $K_f$  values, given in Fig. 5.5, was approximated to a normal law with a mean value of 1 and a standard deviation of 0.1.

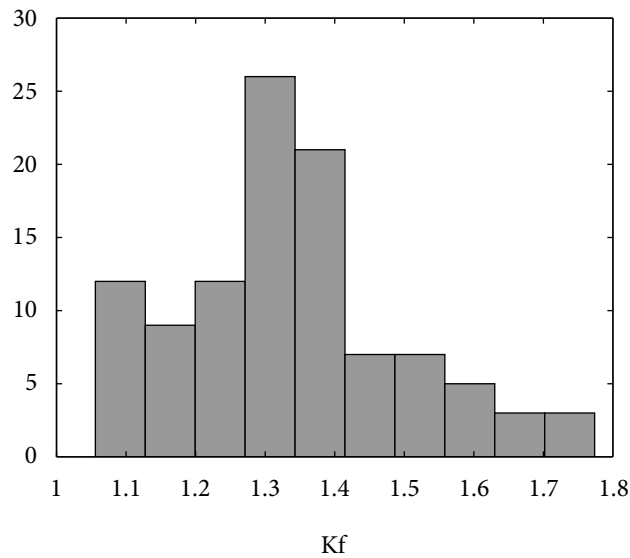


**Figure 5.5** – Dispersion determined for the stress concentration fatigue factor  $K_f$  from the surface roughness profile obtained for the QST rebar.

#### 5.4 Stress concentration factor-rib geometry

Fatigue cracks in rebars usually initiate at the transversal rib base region (a zone between the weld toe radius and the rebar cylinder) [9, 10]. This critical region, illustrated in Fig. 5.6, is located along the ribs and it shows high stress concentration factors  $K_t$  values on the rebar surface [11].

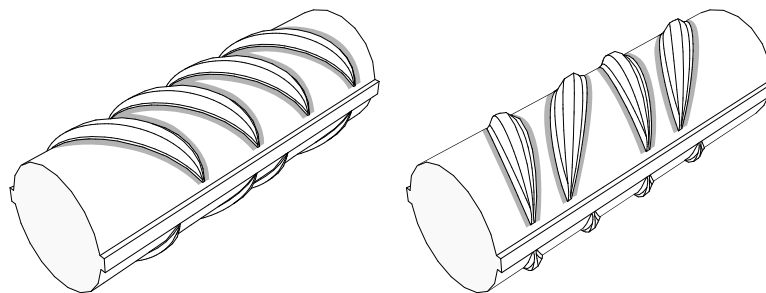


**Figure 5.6** – Illustration of the critical zone along the ribs considered in this work.

The rib geometry details and the respective stress concentration factors are mostly unknown for the experimental data considered in this paper. However, these data, especially for QST rebars, consist mainly of specimens with similar rib patterns. Moreover, an average  $K_t = 1.6$  can be expected on the zone along the transversal

ribs [11] where fatigue cracks can initiate. For this reason, the effect of the rib geometry was considered by a constant  $1/K_t$  factor multiplied by each stress range level in the model for HR-CW and QST rebars. A similar approach is given in [12].

## 5.5 Results and discussion

The influence of microstructure, surface roughness ( $K_f$ ) and rib geometry ( $K_t$ ) on the scatter and fatigue behaviour of HR-CW and QST rebars was analysed in this work. A total of 1000 simulations were run for different stress range levels. The material properties considered in this model are given in [2]. Ferrite-pearlite (F-P) and tempered martensite (TM) refers to the models for HR-CW and QST rebars, respectively.

The model included both crack initiation and propagation phases. The initiation phase is a stochastic process which includes the growth of microstructurally short cracks. Short cracks are allowed to grow to a maximum length of  $2a$  equal to 10 grains from where the macro crack propagation phase starts [13] (see Fig. 5.1). A short crack propagates if  $\Delta\tau_{Li}^{notch}$  is greater than  $\Delta\tau$ . If this condition is not satisfied, the short crack stops to propagate and a run-out result is obtained in the model. Run-out result is, therefore, a non-propagating micro crack in an analysed region near the rib; if the short crack growth stops, it will no longer propagates. Since the simulations were run to utmost 100 million cycles, run-out results obtained at any number of cycles in the simulations represent run-outs at 100 million cycles as well.

The propagation phase in the model shows a macro crack growth where the influence of microstructural features such as grain-phase boundaries and grain orientation ratio is negligible. For this reason, similar grain sizes were considered with constant increments of the plastic zone  $c_i=D_{mean}$ . In fatigue testing of rebars with  $d=16$  mm, when a surface crack length  $2a$  of approximately 8 mm was detected, a rapid failure was in process [9]. Since rebars with  $d \leq 16$  mm are also considered in the experimental data, the fatigue behaviour prediction would be overestimated for a crack length of 8 mm. For this reason, rebar failure was assumed, in all cases, for a surface crack length  $2a=6$  mm in the model.

Figs. 5.7 to 5.10 show the F-P and TM model results obtained for the crack initiation and propagation phases compared to experimental data. Experimental data is always represented in black and model results is represented in other colors. These data consist of HR-CW and QST rebars with diameter  $d \leq 16$  mm [9,14–17].

Figs. 5.7 and 5.9 show the model data points obtained for the crack initiation phase predicted for HR-CW and QST rebars, respectively. The green marks represent the number of cycles for a crack to overcome the first grain boundary at an applied stress range level. The blue marks correspond to the fatigue life of a short crack that propagated over 10 grains. Since the average grain size considered in the model for HR-CW and QST rebars is about  $20 \mu\text{m}$  [2, 18], the crack length at the end of the initiation phase is approximately 0.2 mm.

The model results given in Figs. 5.7 to 5.10 show that a large fraction of the fatigue life of HR-CW and QST rebars is occupied by the crack initiation phase. This phase consists of the short crack growth to a maximum length of 0.2 mm and it covers approximately  $80 (\pm 10) \%$  and  $60 (\pm 10) \%$  near the fatigue limit of HR-CW and QST rebars, respectively. Paris' law is, therefore, not appropriate for fatigue life predictions of rebars since it misses a significant part of the fatigue life prediction.

The difference between experimental and model data at high stress range levels (see Fig. 5.7) may be explained by the different pearlite area fractions that can be found in HR-CW rebars; their area fractions can vary between 15 and 55% while in the model a pearlite fraction of 53% was considered as given in [18]. Moreover, the higher scatter obtained in the initiation phase, especially for the crack to overcome the first grain boundary, is likely influenced by the presence of two different phases: the stress required to propagate in a pearlite grain, for example, is greater than the stress to overcome a (softer) ferrite grain [2].

The scatter trend obtained in the F-P and TM models, (see Figs. 5.7 to 5.10) was similar to the scatter obtained from experimental results, with an increase of scatter as the applied stress approaches the fatigue limit.

Figs. 5.11 and 5.12 shows the dispersion of the analysed parameters including only failure data points. To analyse the effect of a parameter in the model, the dispersion inherent to the other parameters was kept constant. The black points in Figs. 5.11 and 5.12 represent the influence of each parameter independently and the light grey points represent the dispersion of all the other parameters together. F-P and TM model results show that the influence of  $m_i/m_1$  and grain size variation have similar effect on the scatter (see Figs. 5.11 and 5.12). Microstructure and roughness show approximately the same influence, near the fatigue limit, in both F-P and TM models; each parameter affects in about 50% the scatter at this region.

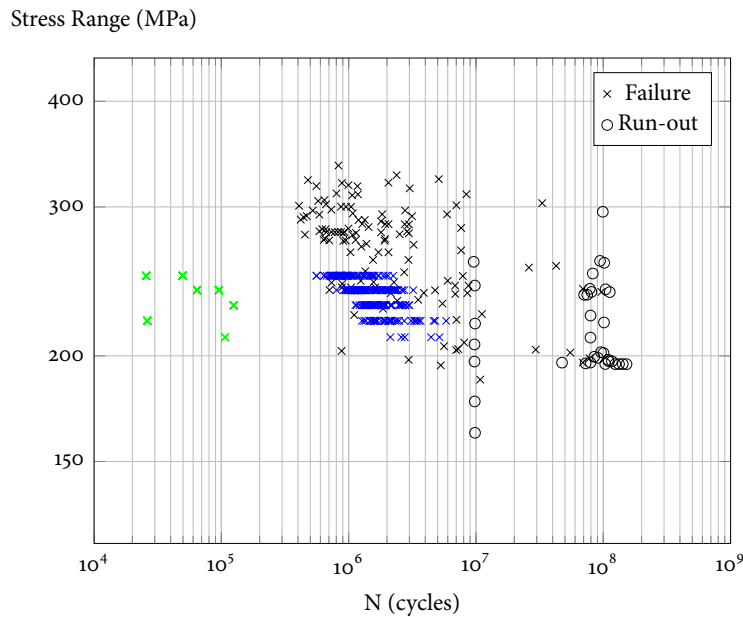


**Figure 5.7** – Data points including the crack initiation phase (green marks: fatigue crack size = 1 grain; blue marks: fatigue crack size = 0.2 mm) in the F-P model and experimental data (black marks) of HR-CW rebars with diameter  $D \leq 16$  mm [14, 15].

## 5.6 Conclusion

The fatigue behaviour of HR-CW and QST rebars was predicted using an adapted N-R short crack growth model which includes stochastic crack initiation and linear propagation phases. The model takes into account the influence of the surface microstructure (grain orientation, grain size variation and phase) and roughness on the crack growth. The stress concentration factor from the rib geometry was considered as a constant parameter: it covers a critical region along the ribs which mostly show similar patterns. Based on the work presented in this paper, the following conclusions can be drawn:

- The main aspects influencing the fatigue behaviour of rebars, used as reference, were likely treated in this study using the F-P model and the TM models, since the scatter and fatigue behaviour predictions obtained from the models were similar to the experimental results. However, since fatigue test results from the literature include rebars with different rib patterns as well as residual stress at/near surface, the variation of these parameters may also influence their fatigue behaviour.

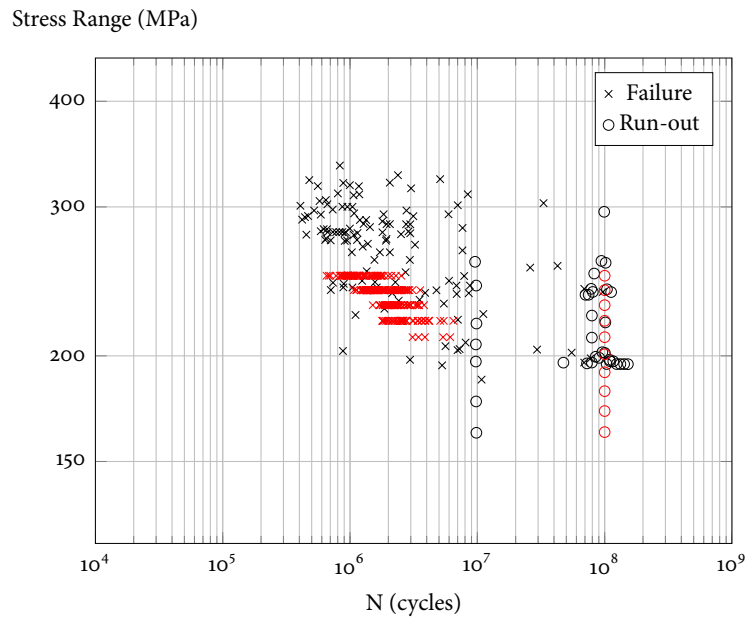


**Figure 5.8** – Data points including the crack propagation phase (red marks) in the F-P model and experimental data (black marks) of HR-CW rebars with diameter  $D \leq 16$  mm [14, 15].

- The fatigue life of HR-CW and QST rebars is largely occupied by the crack initiation phase. This phase consists of a crack which grows to a maximum length of 10 grains (or approximately 0.2 mm) in the model. Crack initiation covers, in general, 80 and 60% of the fatigue life near (but above) the fatigue limit of HR-CW and QST rebars, respectively. Paris' law is, therefore, not appropriate to model fatigue of rebars since it misses most of the behaviour.
- The model shows that the influence of surface microstructure and roughness, on the scatter near the fatigue limit of HR-CW and QST rebars, is about 50% separately. TM model presents less scatter compared to F-P model and it shows that QST rebars have a better fatigue resistance and a higher fatigue strength than HR-CW rebars.



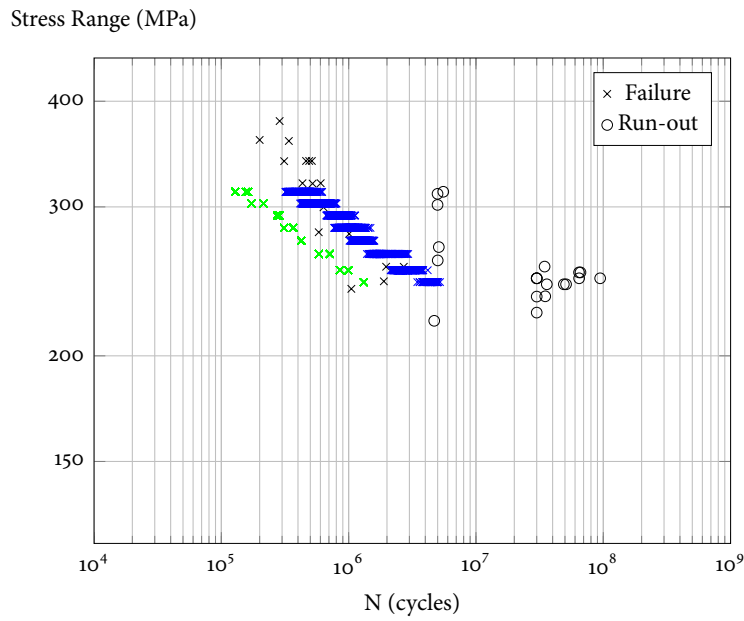


**Figure 5.9** – Data points including the crack initiation phase (green marks: fatigue crack size = 1 grain; blue marks: fatigue crack size = 0.2 mm) in the TM model and experimental data (black marks) of QST rebars with diameter  $D \leq 16$  mm [9, 16, 17].

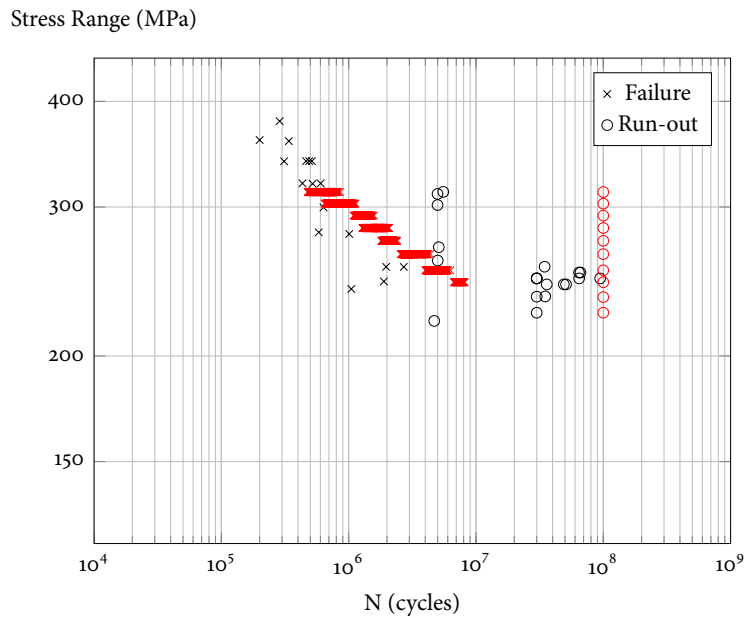


**Figure 5.10** – Data points including the crack propagation phase (red marks) in the TM model and experimental data (black marks) of QST rebars with diameter  $D \leq 16$  mm [9, 16, 17].

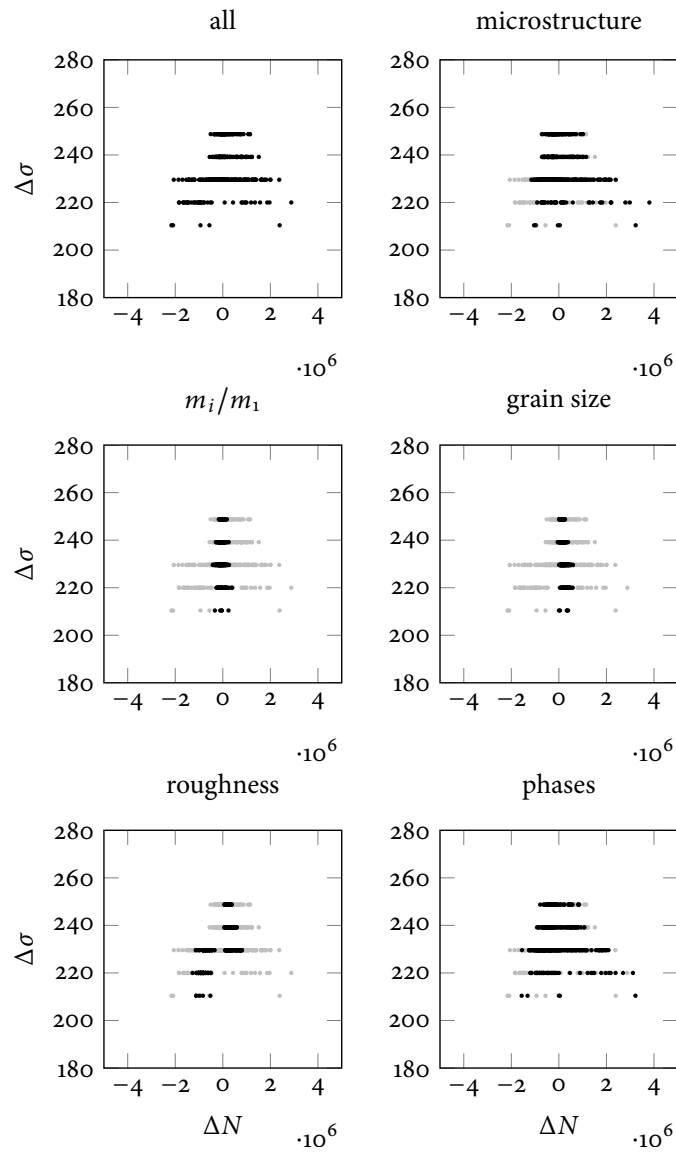


**Figure 5.11** – Influence of the - 1) Microstructure and roughness together (all); 2) Microstructure, including grain orientation ratio  $m_i/m_1$ , grain size variation, phases (ferrite-pearlite); 3) Each parameter of the microstructure separately and 4) Surface roughness - on the scatter obtained in the F-P model.

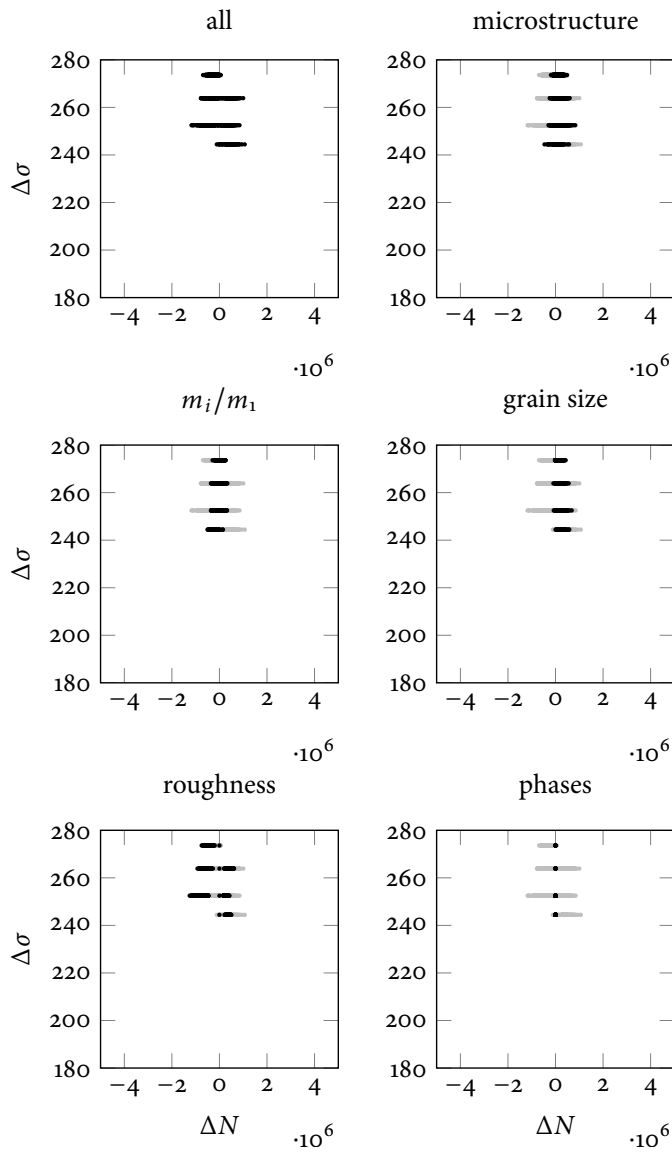


**Figure 5.12** – Influence of the - 1) Microstructure and roughness together (all); 2) Microstructure, including grain orientation ratio  $m_i/m_1$ , grain size variation, phases (martensite); 3) Each parameter of the microstructure separately and 4) Surface roughness - on the scatter obtained in the TM model.

---

## Bibliography

---

- [1] Milne, I., Ritchie, R. O., & Karimhaloo, B. L. (2003). *Comprehensive structural integrity: Cyclic loading and fatigue*. Elsevier.
- [2] Rocha, M., Brühwiler, E., & Nussbaumer A. Microstructural influence on the scatter in the fatigue life of steel reinforcement bars.
- [3] Frost, N. E., & Dugdale, D. S. (1957). Fatigue tests on notched mild steel plates with measurements of fatigue cracks. *Journal of the Mechanics & Physics of Solids*, 5(3), 182-192.
- [4] Yates, J. R., & Brown, M. W. (1987). Prediction of the length of non propagating fatigue cracks. *Fatigue & Fracture of Engineering Materials & Structures*, 10(3), 187-201.
- [5] Taira, S., Tanaka, K., & Hoshina, M. (1979). Grain size effect on crack nucleation and growth in long-life fatigue of low-carbon steel. *ASTM STP*, 675, 135-173.
- [6] Vallengano, C., Navarro, A., & Dominguez, J. (2000). Fatigue crack growth threshold conditions at notches-Part I: Theory. *Fatigue & Fracture of Engineering Materials & Structures*, 23(2), 113-122.
- [7] Hussain, K., De Los Rios, E. R., & Navarro, A. (1993). A two-stage micromechanics model for short fatigue cracks. *Engineering Fracture Mechanics*, 44(3), 425-436.
- [8] Arola, D., & Williams, C. L. (2002). Estimating the fatigue stress concentration factor of machined surfaces. *International Journal of Fatigue*, 24(9), 923-930.
- [9] Rocha, M., Michel, S., Brühwiler, E., & Nussbaumer A. Very high cycle fatigue tests of quenched and self-tempered steel reinforcement bars.

- [10] Hanson, J. M., Burton, K. T., & Hognestad, E. (1968). Fatigue tests of reinforcing bars - effect of deformation pattern. *Journal of the PCA Research and Development Laboratories*, 10, 2-13.
- [11] Rocha, M., Brühwiler, E., & Nussbaumer A. Material and geometrical characterisation of quenched and self-tempered steel reinforcement bars.
- [12] Schijve, J. (2001). *Fatigue of structures and materials*. Dordrecht: Kluwer Academic.
- [13] Tokaji, K., & Ogawa, T. (1992). The growth behaviour of microstructurally small fatigue cracks in metals. *Short fatigue cracks, ESIS*, 13, 85-99.
- [14] Tilly, G. P. (1979). Fatigue of steel reinforcement bars in concrete: a review. *Fatigue & Fracture of Engineering Materials & Structures*, 2(3), 251-268.
- [15] Tilly, G. P. (1984). Fatigue testing and performance of steel reinforcement bars. *Matériaux et Construction*, 17(1), 43-49.
- [16] Donnell, M. J., Spencer, W., & Abel, A. (1986). Fatigue of Tempcore reinforcing bars - the effect of galvanizing. In *Australasian Conference on the Mechanics of Structures and Materials*, 10th, 1986, Adelaide, Australia (Volume 2).
- [17] Zheng, H., & Abel, A. A. (1999). Fatigue properties of reinforcing steel produced by Tempcore process. *Journal of Materials in Civil Engineering*, 11(2), 158-165.
- [18] Jhamb, I. C., & MacGregor, J. G. (1974). Stress concentrations caused by reinforcing bar deformations. *ACI Special Publication*, 41-8, 169-182.

## 6.1 Introduction

This thesis applies concepts of the mechanics of materials and material engineering to define micro and macro structural aspects affecting the fatigue strength of different type of steel reinforcement bars (rebars). It provides advancements in the structural engineering methods used for fatigue life prediction. This research includes fatigue tests at very high number of stress cycles, micro-macro structural characterisation of rebars and an analytical model which predicts the main parameters influencing the fatigue behaviour of rebars.

## 6.2 Response to research questions

The main thesis contribution and findings to the research questions raised in Section 1.1 are concluded in this sub-chapter.

### 6.2.1 Fatigue testing

Experimental test data are used as reference to predict the fatigue behaviour of rebars in concrete structures. Axial tests of rebars alone have the advantage to be performed at very high number of stress cycles, i.e., greater than 10 million, at reduced time – and consequently costs – compared to fatigue tests with rebars embedded in concrete. However, axial fatigue tests are very sensitive to the grip arrangement which can lead to a rebar failure which isn't characteristic of the proper fatigue searched behaviour. This research shows that conical grip is the most effective method preventing premature failure of the rebar inside the grip area. QST rebars mostly survived to a number of cycles exceeding 30 million at stress range levels of approximately 50% of their mean yield strength.

The method used for fatigue crack detection on these survival rebars, based on the application of the liquid penetrant testing (LPT) with an abrupt monitored frequency change (representative of fractured rebars), was ineffective. Survival rebars don't show any abrupt frequency change; indeed, the frequency reaches a stabilization regime from about 1 million cycles on and kept nearly constant during the whole test. Moreover, LPT is a conservative method that can only detect rather large surface cracks of at least 5 mm length.

Surface imperfections were the determinant factor that led to the fracture of rebars, at similar stress ranges as applied for survival rebars. These imperfections are produced during the manufacturing process and located near the transversal ribs, in the zone of highest stress concentrations. Precisions regarding these surface imperfections are given in the next section.

### 6.2.2 Micro-macro structural characterisation

Conditions of the surface layer are most significant for the fatigue behaviour of rebars since fatigue cracks tend to initiate on the surface. This study provides new information on micro and macro surface aspects of QST rebars including experimental analyses of surface residual stresses and imperfections. The influence of geometric parameters on the stress concentration factors  $K_t$  at the rebar surface was investigated by 3D Finite Element (FE) analyses. A parametric study using 3D FE models allowed to determine the influence of rib inclination and rebar size on the  $K_t$  values of the critical zones. There were no references with similar studies of the surface residual stress, imperfections and 3D FE analysis of the geometric  $K_t$  in the literature.

In this research, the microstructure of QST rebars was identified under Optical Microscopy and quantified for different rebar diameters. The analyses showed that the average grain size tends to increase with the increase of the rebar diameter.

Macroscopic residual stresses (type I) were experimentally determined on surface and subsurface of QST rebars by X-ray diffraction and Cut Compliance techniques. Residual stresses were found to be random tensile and compressive stresses with values no higher than 20% of their yield strength.

Surface imperfections and roughness, analysed under Scanning Electron Microscopy (SEM), are mainly located near the transversal ribs. The imperfections can be of different type:

- Marks near the transversal ribs;

- Marks with semi-circular shape near the transversal ribs;
- Cracks near the marks with some cracks perpendicular to the rebar axis. Cracks were also found perpendicular to the longitudinal ribs.

These imperfections are introduced in the rolling mill when the ribs are formed and they may also result from the water quenching process.

This research shows how the rib geometry and rebar diameter affects  $K_t$  values on the rebar surface. The highest  $K_t$  are located at the rib radius zone. The maximum  $K_t$  values at this zone are mainly affected by the rib radius and height.

The highest  $K_t$  values determined along the rib base increase with increasing rebar. The influence of the rebar diameter on these  $K_t$  values is comparable to the changes in the rib radius and height. The maximum  $K_t$  for QST rebars geometry with diameters of 10 and 26 mm are approximately 1.6 and 2.5, respectively. The effect of the rebar diameter on the size of the critical zone is less significant than the influence of rib radius and height.

The rib inclination is the main parameter affecting the position of the maximum  $K_t$  and size of the critical zone along the rib. The critical zones (defined as zones where  $K_t$  are at least 95% of the maximum values) are located anti-symmetrically along the rib. However, the position of the maximum  $K_t$  tends to move to the rib centre and the size of the critical zone increases if the rib inclination becomes more and more perpendicular to the rebar axis.

### 6.2.3 Analytical model-part I

The scatter present in fatigue test results of rebars can be influenced by the sensitivity of the short crack growth to the microstructural features. This thesis proposes an adapted Navarro and De Los Rios (N-R) model within a Monte-Carlo framework to investigate the scatter above and near the fatigue limit on HR, CW and QST rebars. The N-R model, adapted in this work, incorporates the dispersion of the grain orientation ratio  $m_i/m_1$ , grain size variation and two phases (ferrite and pearlite) in the case of HR-CW rebars. A  $m_i/m_1$  equation is developed to take into account crack closure effects and the variation of the grain orientations. Although N-R model has been extensively used for fatigue life prediction of metals, there are no references in the literature where the dispersion of microstructural features have been considered to analyse scatter in fatigue. Moreover, there are no references where a short crack growth model have been applied to study the scatter found in fatigue testing of rebars.



The developed approach shows that surface martensite contributes to reduce the scatter in fatigue tests with rebars compared to ferrite-pearlite microstructure found on the surface of HR-CW rebars. Surface microstructure affects to about 50% the scatter present in the fatigue tests for both HR-CW and QST rebars.

#### 6.2.4 Analytical model-part II

The adapted N-R model in Section 6.2.3 is modified to include:

- the surface roughness effect in order to explain the difference in the scatter found in the analyses with the surface microstructure;
- a linear crack propagation phase where the effect of microstructural features is negligible in the crack growth.

The stress concentration factor from the rib geometry is considered as a constant parameter. This approach allows more realistic comparisons between model and experimental data. The model predicts the fatigue behaviour of HR-CW and QST rebars including fatigue crack initiation (cyclic slip, nucleation and short crack growth) and propagation (macro crack) phases.

This model shows fatigue behaviour predictions similar to test results for HR-CW and QST rebars. The main finding is that the fatigue life of rebars is largely occupied by the crack initiation phase during which the application of Paris' law is infeasible.

This modelling demonstrates that QST rebars have a better fatigue resistance and a higher fatigue strength than HR-CW rebars. The standard S-N curves [1], used for safety verification, are nowadays classified according to the rebar size but there is no distinction between the fatigue strength of HR-CW and QST rebars. This approach is conservative and it is recommended to classify S-N curves according to the rebar type and size.

Fatigue cracks tend to initiate at the zone close to the ribs [2], [3], where the highest stress concentrations are present. The stress concentrations resulting from the rib geometry combined with the surface roughness near the ribs lead to a significant reduction on the fatigue strength of rebars. As a consequence, this finding suggests the use of plain rebars with surface martensite microstructure for fatigue relevant structures.

## 6.3 Future work

### 6.3.1 Fatigue crack detection

One of the greatest challenges in fatigue testing of rebars is the detection of cracks or microcracks, during or after the tests, in particular run-out tests. The methods used for crack detection are not efficient and therefore investigations are required in this area. One possible solution is to investigate the use of nanoparticles, in low surface tension solution, with further X-ray micro computed tomography analyses.

### 6.3.2 Grain orientation ratio

In this study, the equation proposed for the grain orientation ratio  $m_i/m_1$  was developed for randomly oriented grains. However, it is possible that HR, CW and QST rebars may show a preferential crystallographic orientation in the rolling direction. To provide more accurate microstructural information for the short crack growth modelling, the crystallographic texture of HR, CW and QST rebars could be determined by X-ray diffraction technique. Further research is needed on the effect of R-ratio in the fatigue behaviour of rebars. As given in [4], the  $m_i/m_1$  factor is affected by crack closure which partially governs the material resistance to fatigue damage. However, experimental data in the literature is still rather scarce for R-ratio greater than 0.2. The crack closure effect could be included in the  $m_i/m_1$  equation in the N-R model as proposed in this thesis.

### 6.3.3 Surface roughness

Further work is required in generating more information on the surface roughness profile near and between the ribs. This information could provide more accuracy on the effect of the surface roughness on the scatter present in fatigue tests and improve the fatigue behaviour prediction.

### 6.3.4 Fatigue behaviour modelling-other methods

For further modelling of fatigue behaviour, it is suggested to use the formulation proposed by Vallellano et al. [5] for non-symmetric conditions. Finite element (FE) modelling could be another promising method for a more detailed investigation on the stress field at each step of the short crack propagation, including the effect of local microresidual stresses, into and at the grain boundary. FE method has also the advantage to allow for the study of crack coalescence since the stress distribution of

the grains, of an analysed area, would not be uniform and micro cracks could start simultaneously at different grains.

The effect of variable amplitude loading could be studied by detailed modelling in parallel with lab tests to give a better understanding on the fatigue behaviour of rebars under the condition representative for structures subjected to fatigue.

---

## *Bibliography*

---

- [1] Model code 2010-final draft, fib, Bulletin N°65, Vol.1.
- [2] Hanson, J. M., Burton, K. T., & Hognestad, E. (1968). Fatigue tests of reinforcing bars - effect of deformation pattern. *Journal of the PCA Research and Development Laboratories*, 10, 2-13.
- [3] Rocha, M., Michel, S., Brühwiler, E., & Nussbaumer A. Very high cycle fatigue tests of quenched and self-tempered steel reinforcement bars.
- [4] Vallellano, C., Navarro, A., García-Lomas, F. J., & Domínguez, J. (2008). On the estimation of microstructural effects in the near-threshold fatigue of small cracks. *The Journal of Strain Analysis for Engineering Design*, 43(5), 337-347.
- [5] Vallellano, C., Navarro, A., & Domínguez, J. (2002). Compact formulation for modelling cracks in infinite solids using distributed dislocations. *Philosophical magazine A*, 82(1), 81-92.



BIBLIOGRAPHY

APPENDIX A

*Stress-Strain curve*

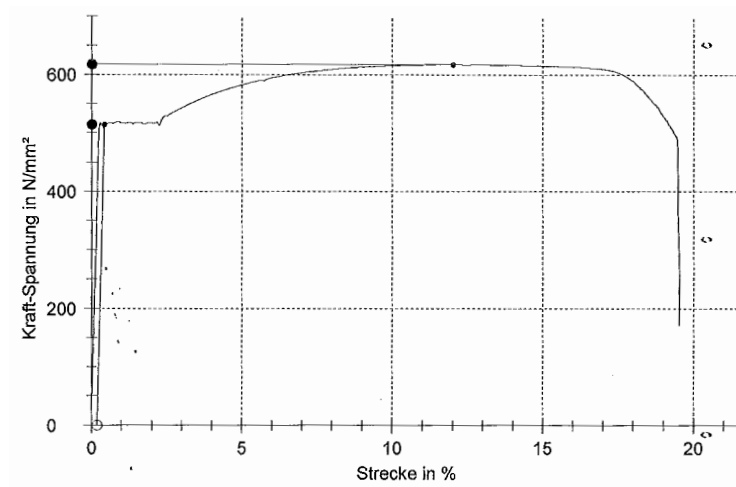


Figure A.1 – Stress × Strain curve of a QST rebar analysed in this thesis.



**APPENDIX A STRESS-STRAIN CURVE**

APPENDIX B  
*Rebar  $K_t$*

Appendix A presents 3D Finite Element Models of the rebar geometry considered in the parametric study. The graphs given in this Appendix shows the evolution of the stress concentration factor,  $K_t$ , determined for the paths illustrated in Fig. B.1. Finite Element analyses were performed with Abaqus/CAE 6.12.

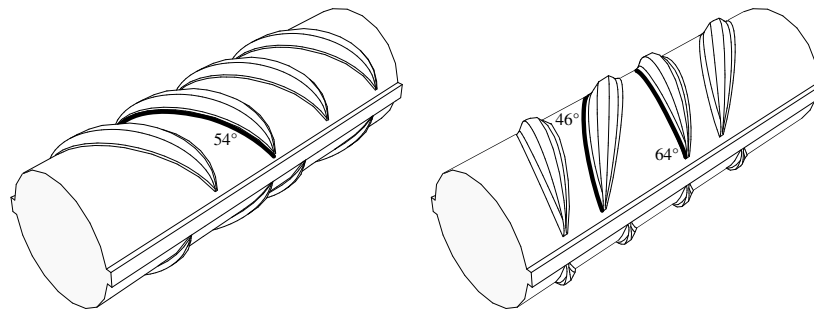


**Figure B.1** – Paths (darker lines) where  $K_t$  evolution was determined.



## B.1 D10h03r02

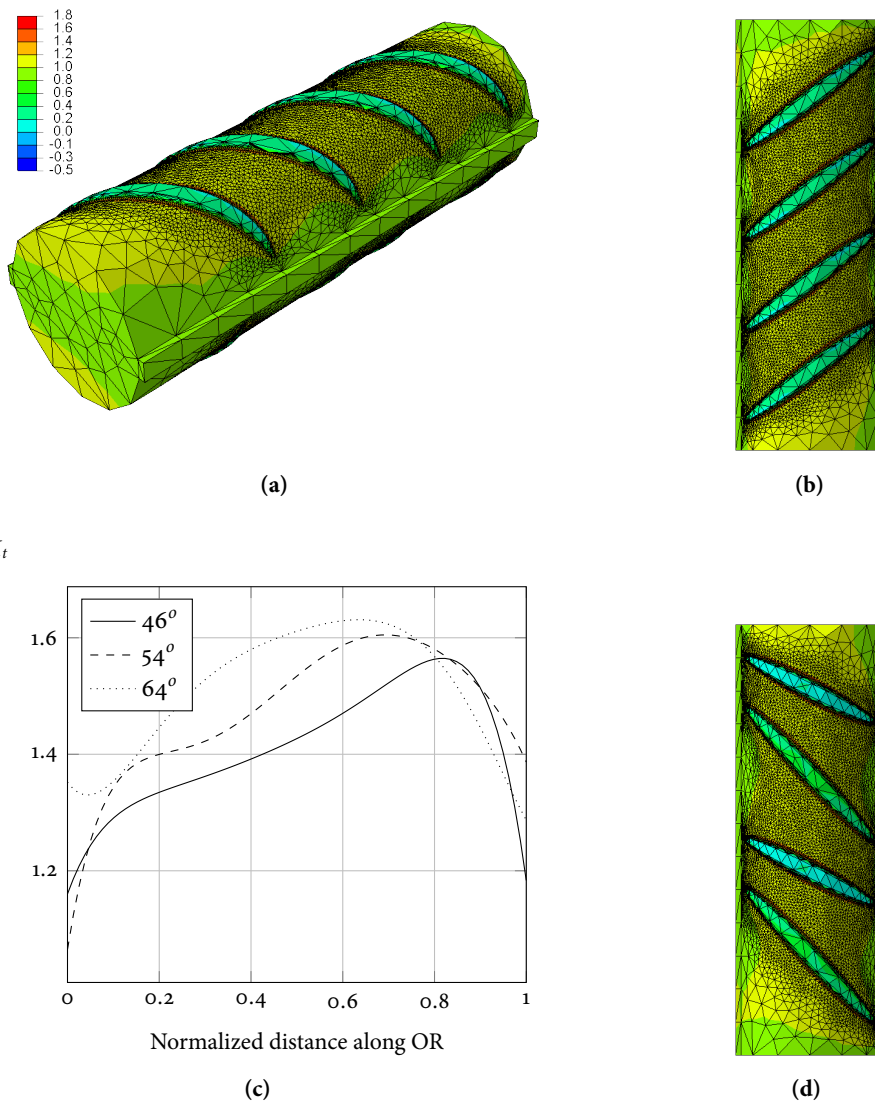
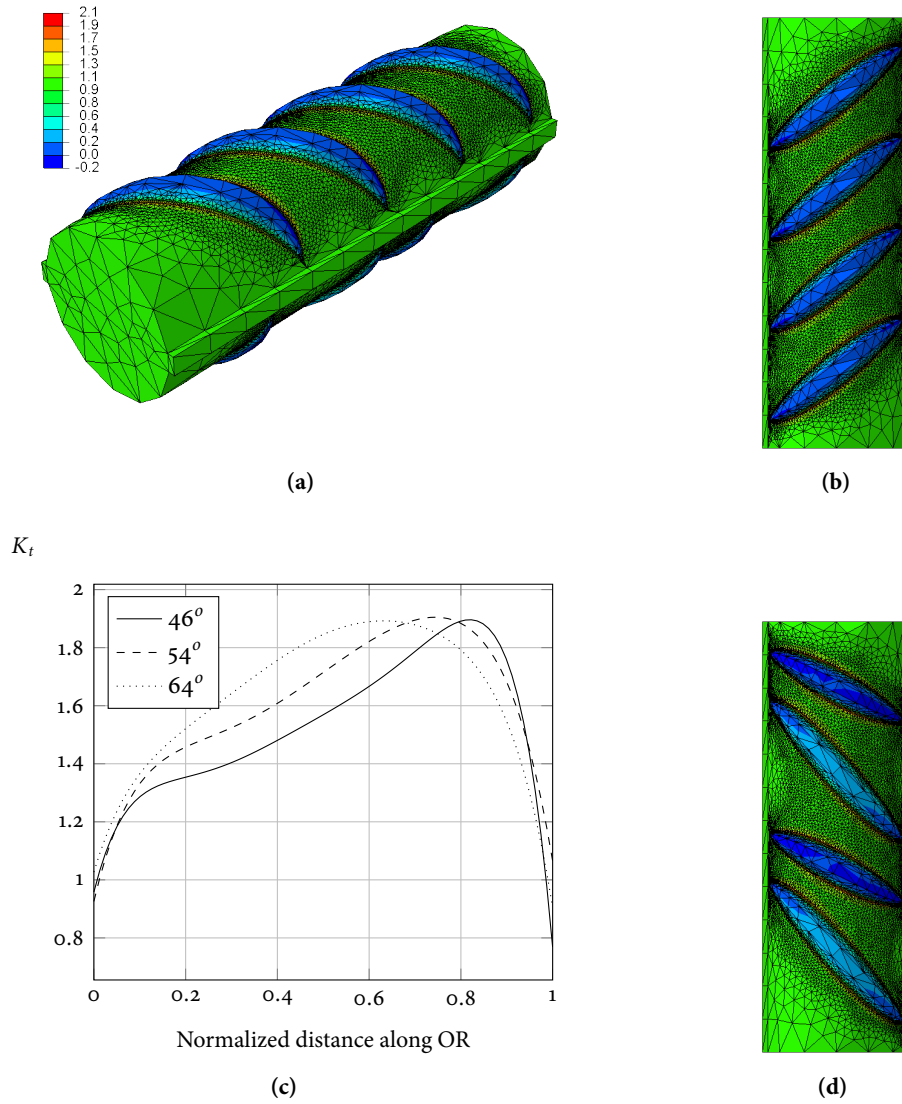


Figure B.2 – D10h03r02 model: (a) 3D FE mesh (b) Top view (c)  $K_t$  plot (d) Bottom view.

## B.2 D10h08r02



**Figure B.3** – D10h08r02 model: (a) 3D FE mesh (b) Top view (c)  $K_t$  plot (d) Bottom view.

### B.3 D10h08r04

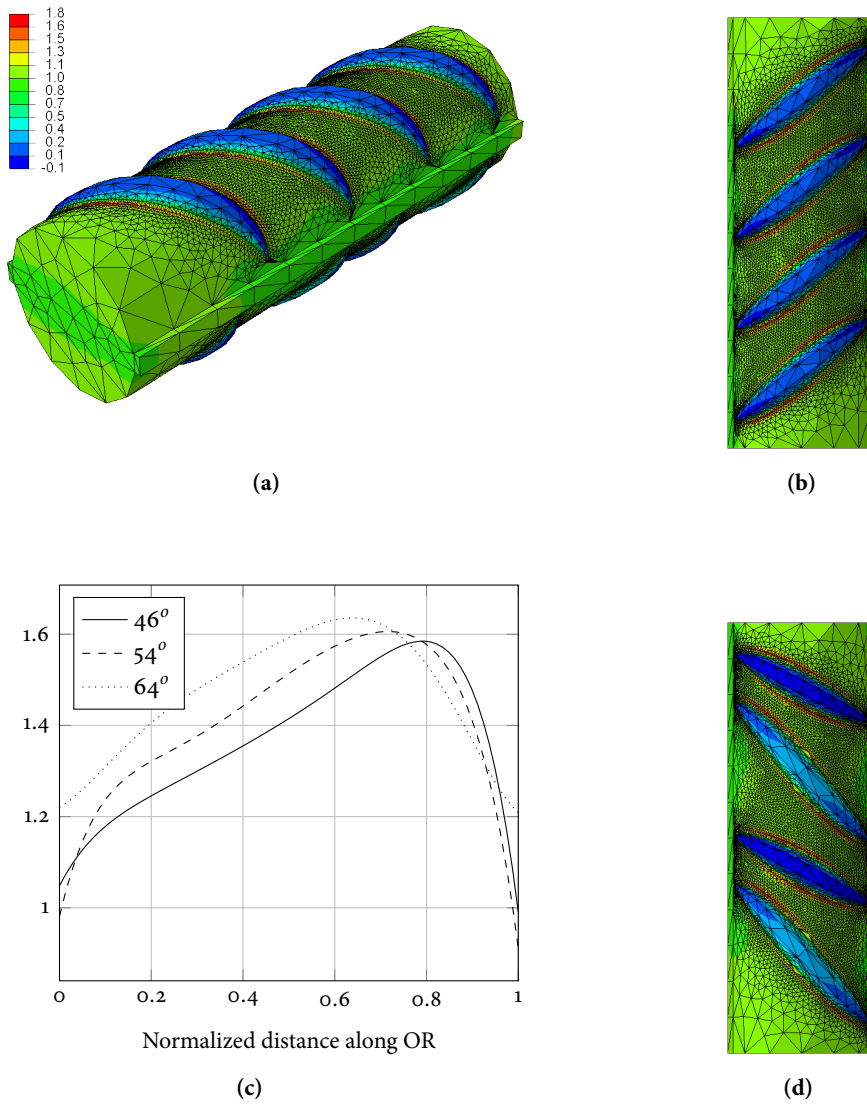


Figure B.4 – D10h08r04 model: (a) 3D FE mesh (b) Top view (c)  $K_t$  plot (d) Bottom view.

## B.4 D10h15r04

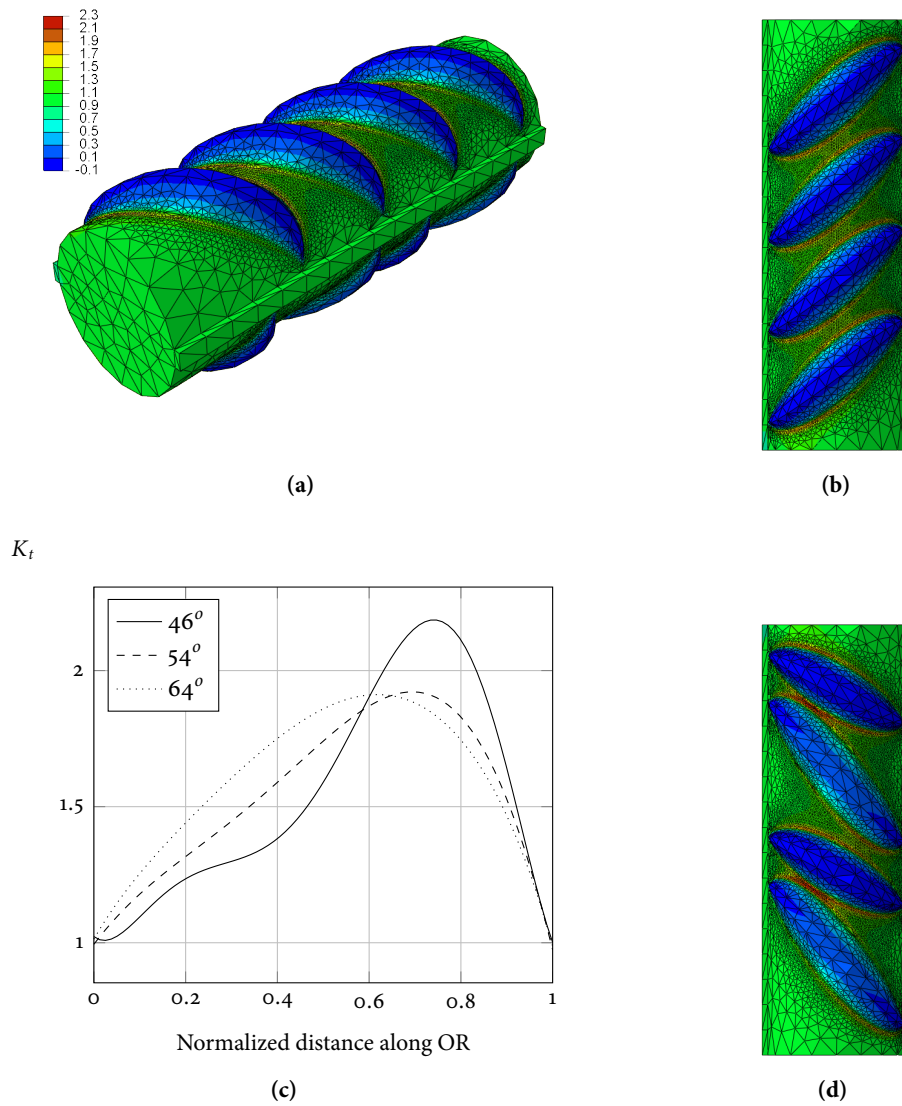
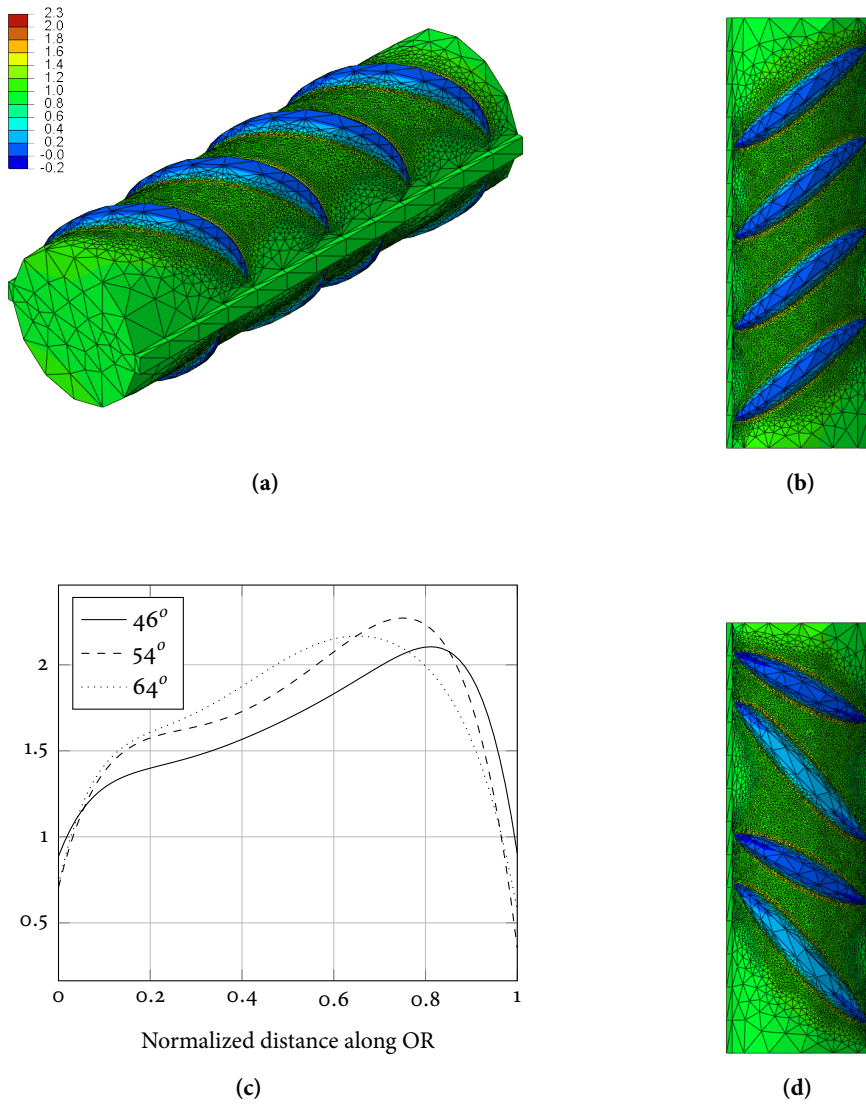


Figure B.5 – D10h15r04 model: (a) 3D FE mesh (b) Top view (c)  $K_t$  plot (d) Bottom view.

## B.5 D10h08



**Figure B.6** – D10h08 model: (a) 3D FE mesh (b) Top view (c)  $K_t$  plot (d) Bottom view.

## B.6 D16ho3ro2

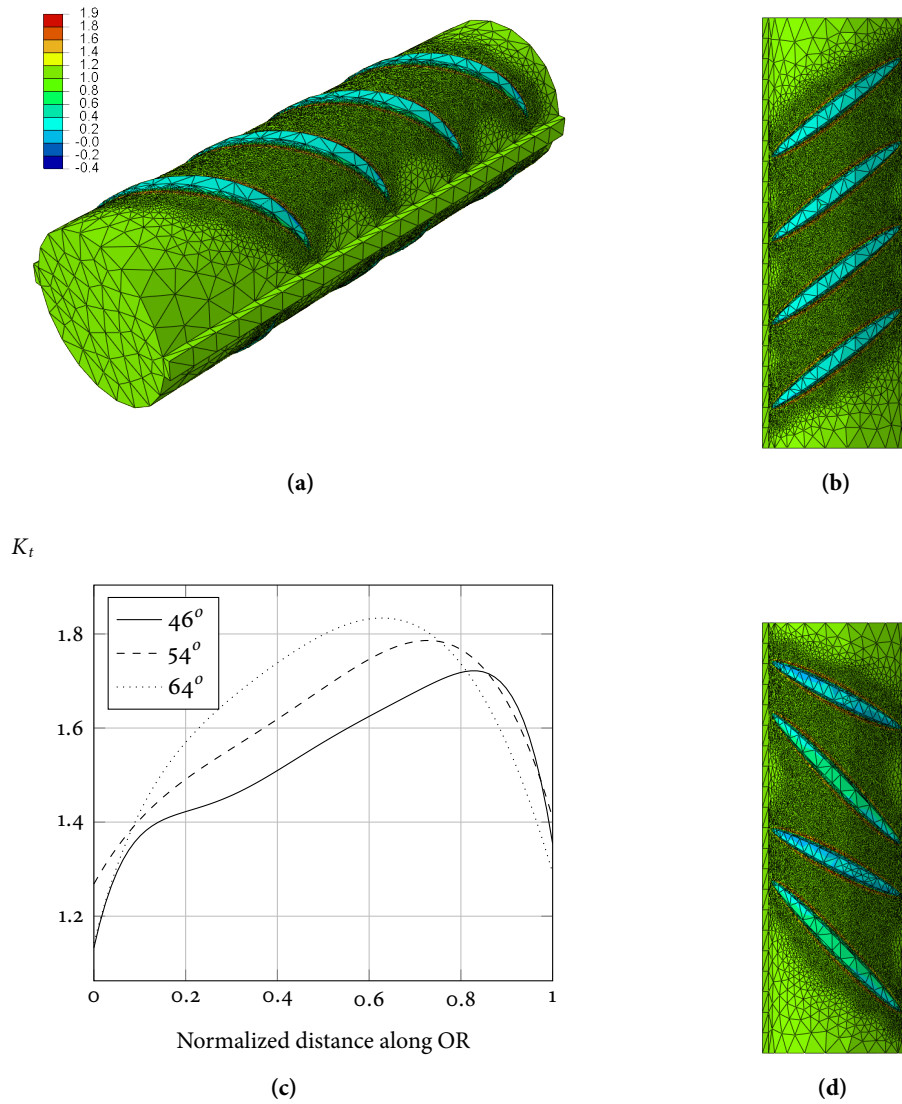
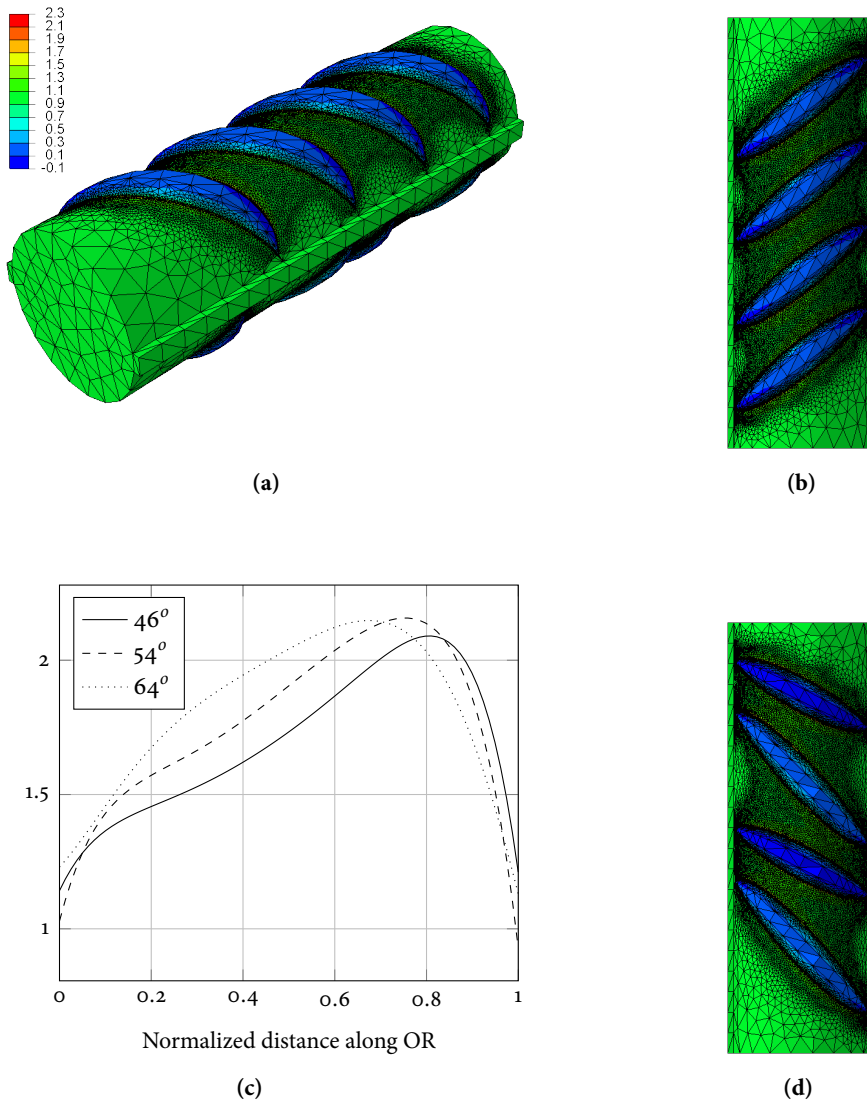


Figure B.7 – D16ho3ro2 model: (a) 3D FE mesh (b) Top view (c)  $K_t$  plot (d) Bottom view.

## B.7 D16ho8ro2



**Figure B.8** – D16ho8ro2 model: (a) 3D FE mesh (b) Top view (c)  $K_t$  plot (d) Bottom view.

## B.8 D16ho8ro4

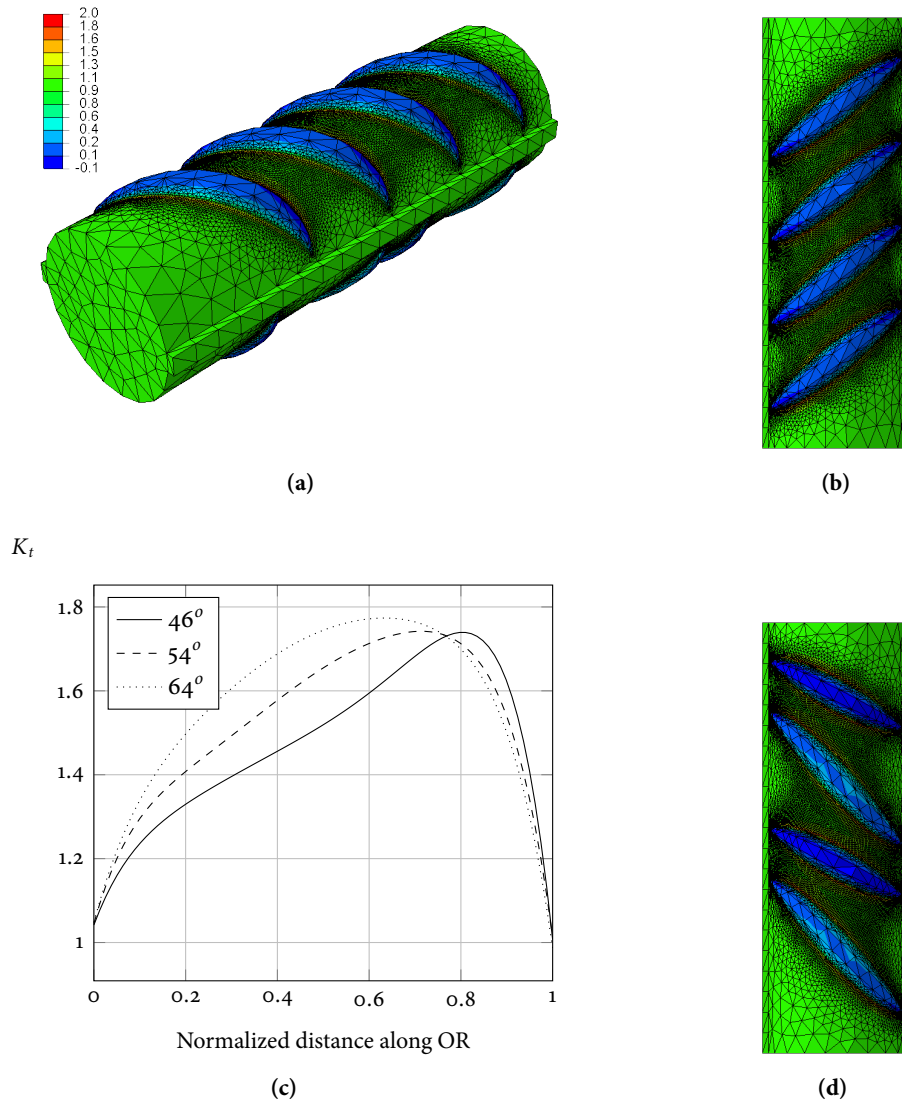


**Figure B.9** – D16ho8ro4 model: (a) 3D FE mesh (b) Top view (c)  $K_t$  plot (d) Bottom view.



## B.9 D16ho8ro8

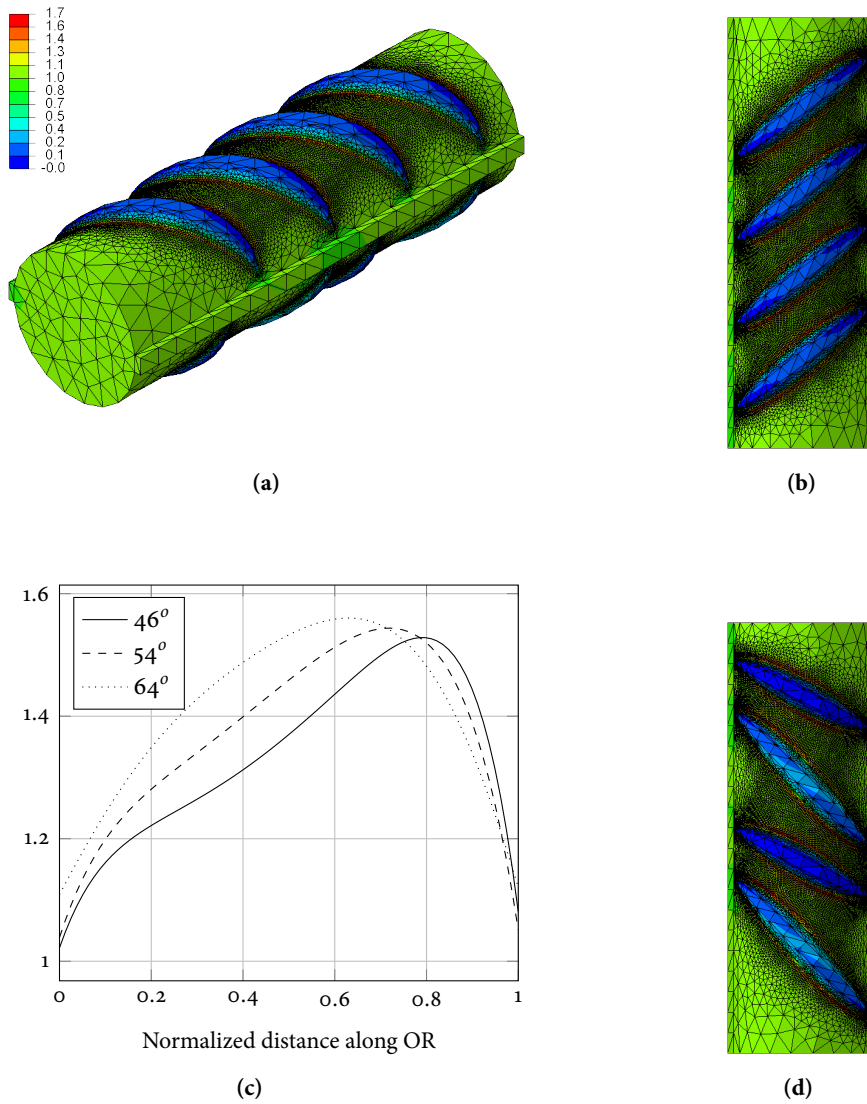


**Figure B.10** – D16ho8ro8 model: (a) 3D FE mesh (b) Top view (c)  $K_t$  plot (d) Bottom view.

## B.10 D16ho8

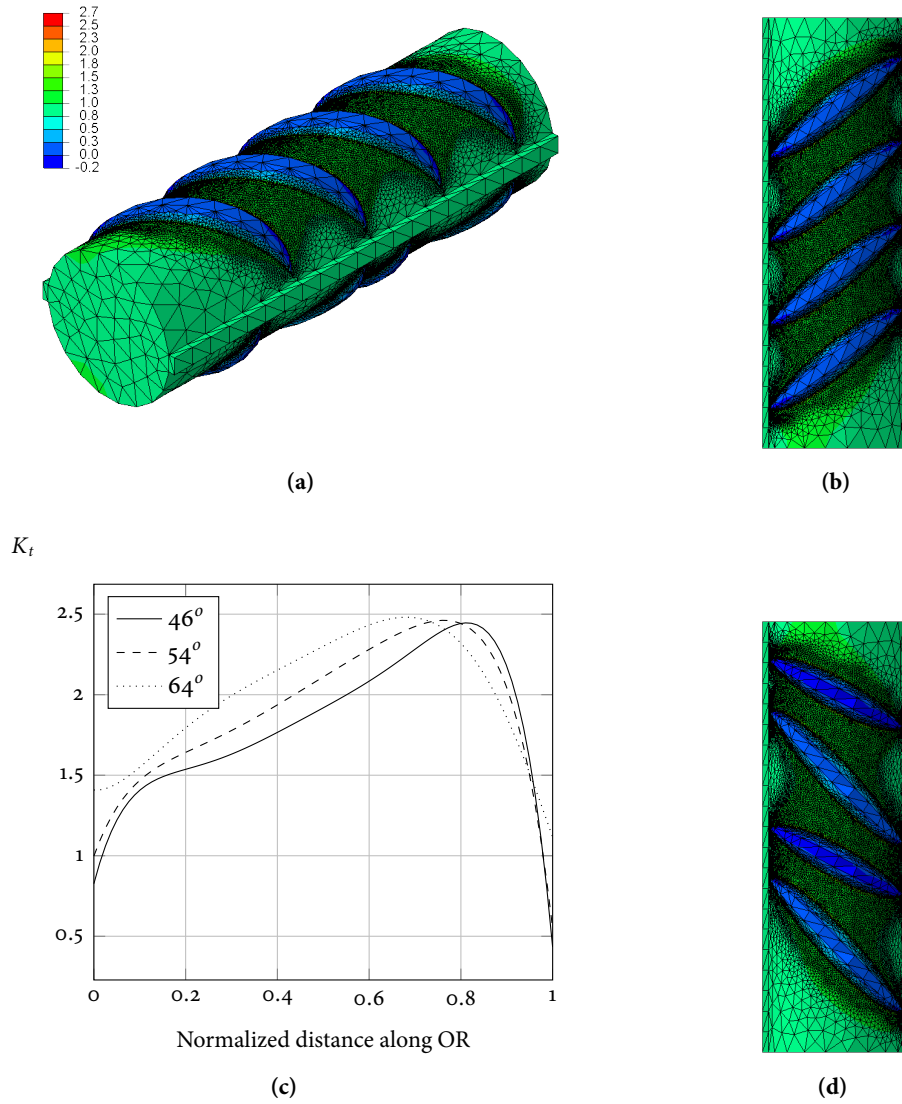
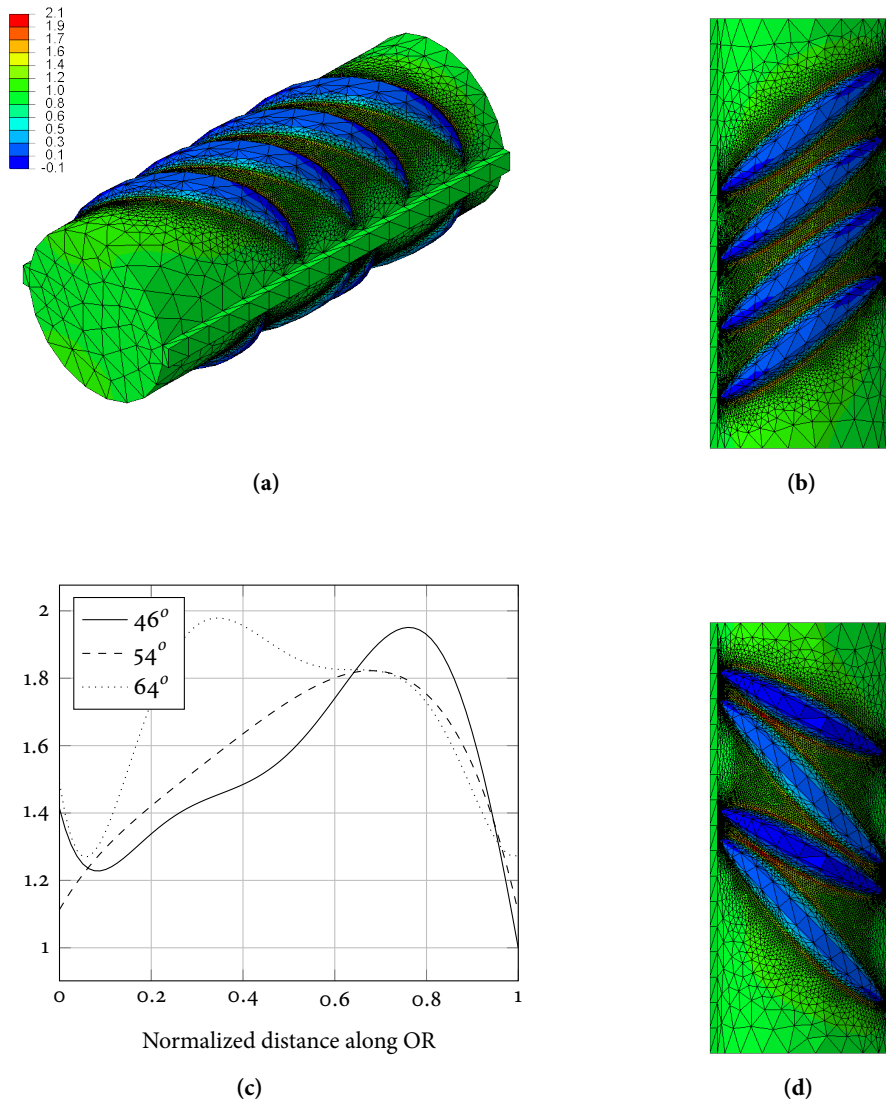


Figure B.11 – D16ho8 model: (a) 3D FE mesh (b) Top view (c)  $K_t$  plot (d) Bottom view.

## B.11 D16ho8ro4co4



**Figure B.12** – D16ho8ro4co4 model: (a) 3D FE mesh (b) Top view (c)  $K_t$  plot (d) Bottom view.

## B.12 D16ho8ro4c12

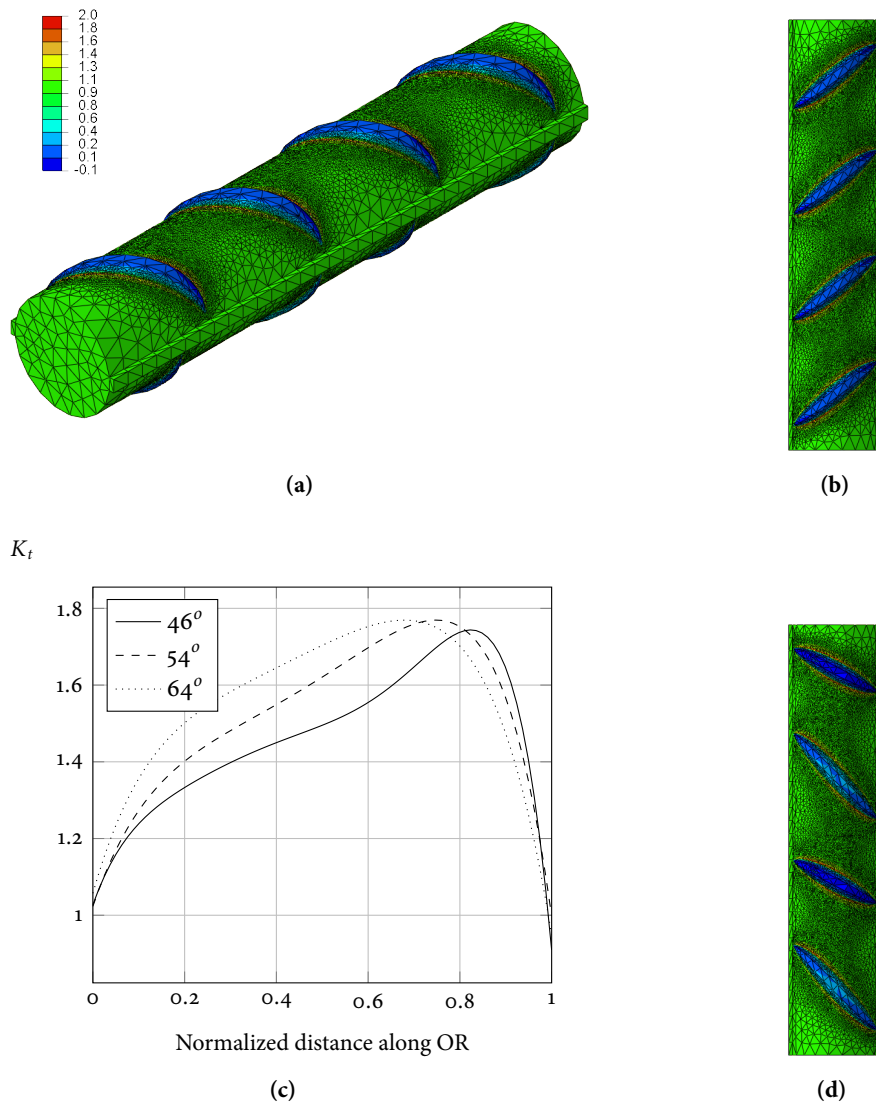


**Figure B.13** – D16ho8ro4c12 model: (a) 3D FE mesh (b) Top view (c)  $K_t$  plot (d) Bottom view.

## B.13 D26ho3ro2

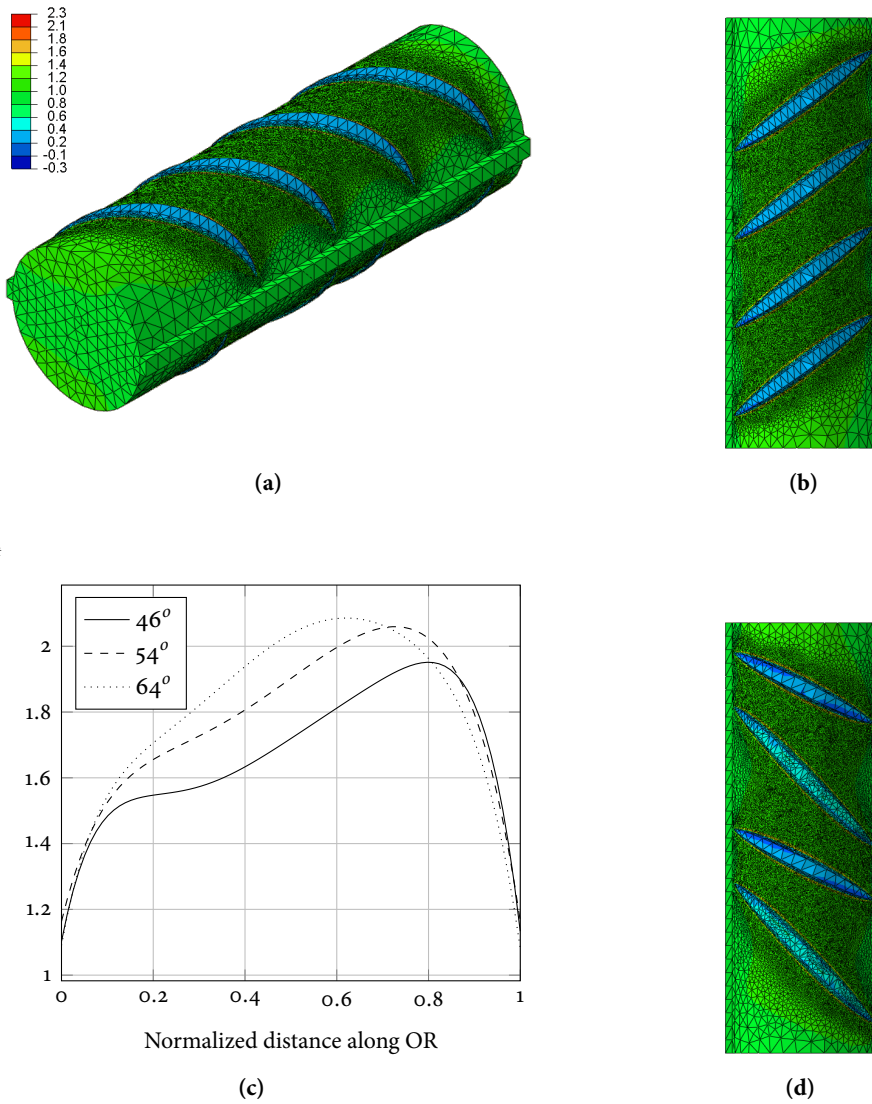


Figure B.14 – D26ho3ro2 model: (a) 3D FE mesh (b) Top view (c)  $K_t$  plot (d) Bottom view.

## B.14 D26ho8ro2

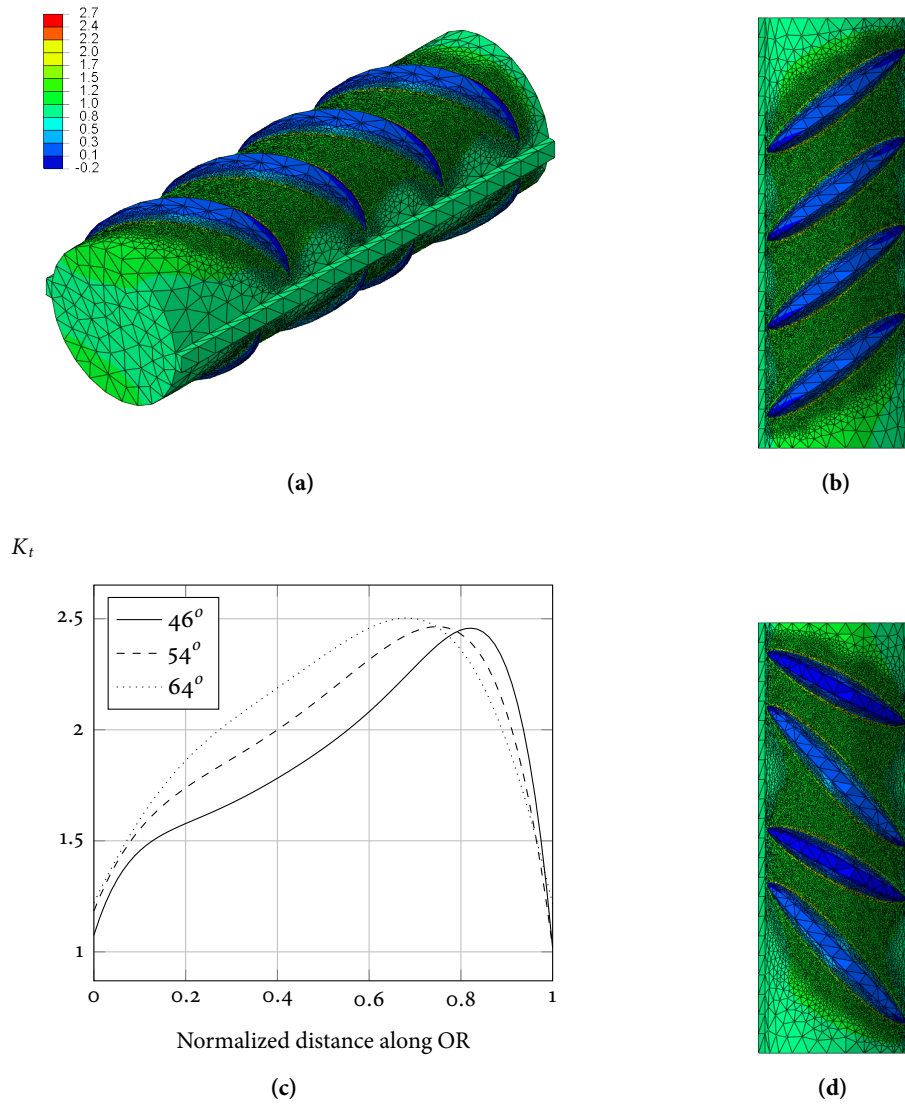


Figure B.15 – D26ho8ro2 model: (a) 3D FE mesh (b) Top view (c)  $K_t$  plot (d) Bottom view.

## B.15 D26ho8ro4

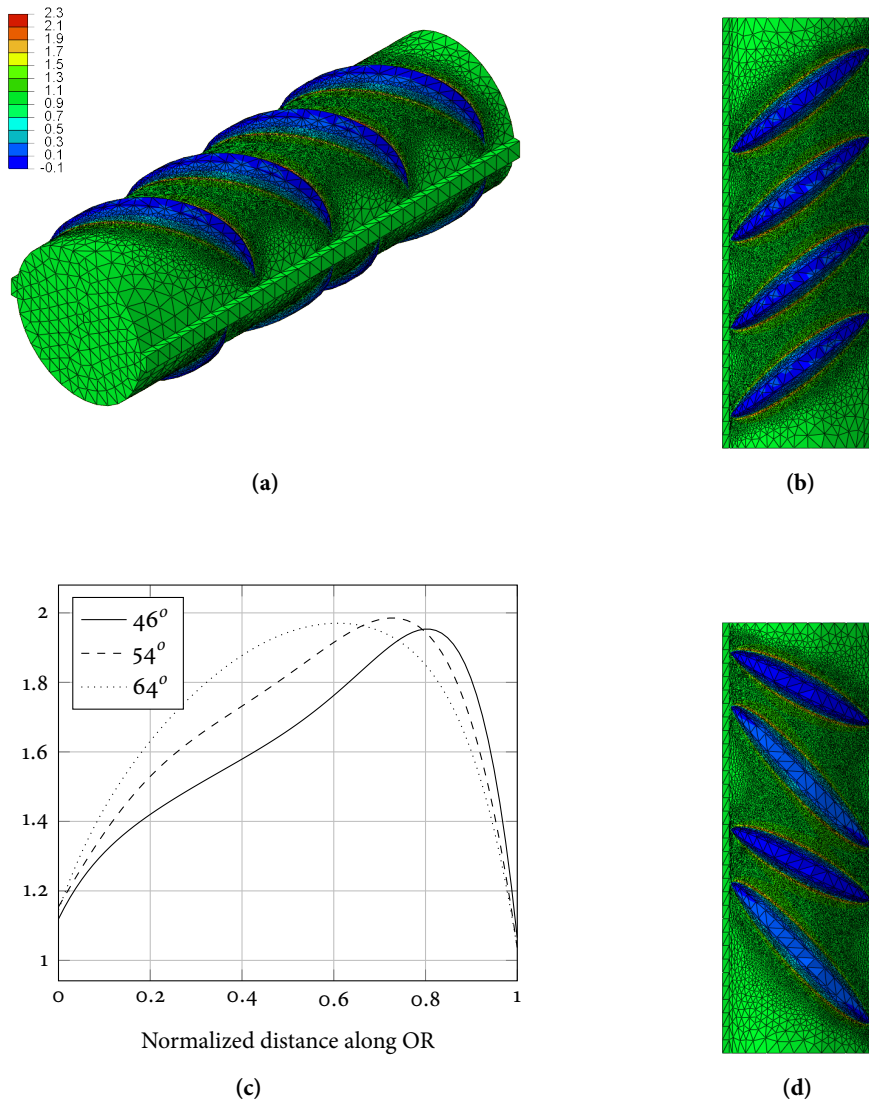


Figure B.16 – D26ho8ro4 model: (a) 3D FE mesh (b) Top view (c)  $K_t$  plot (d) Bottom view.

## B.16 D26h15r04

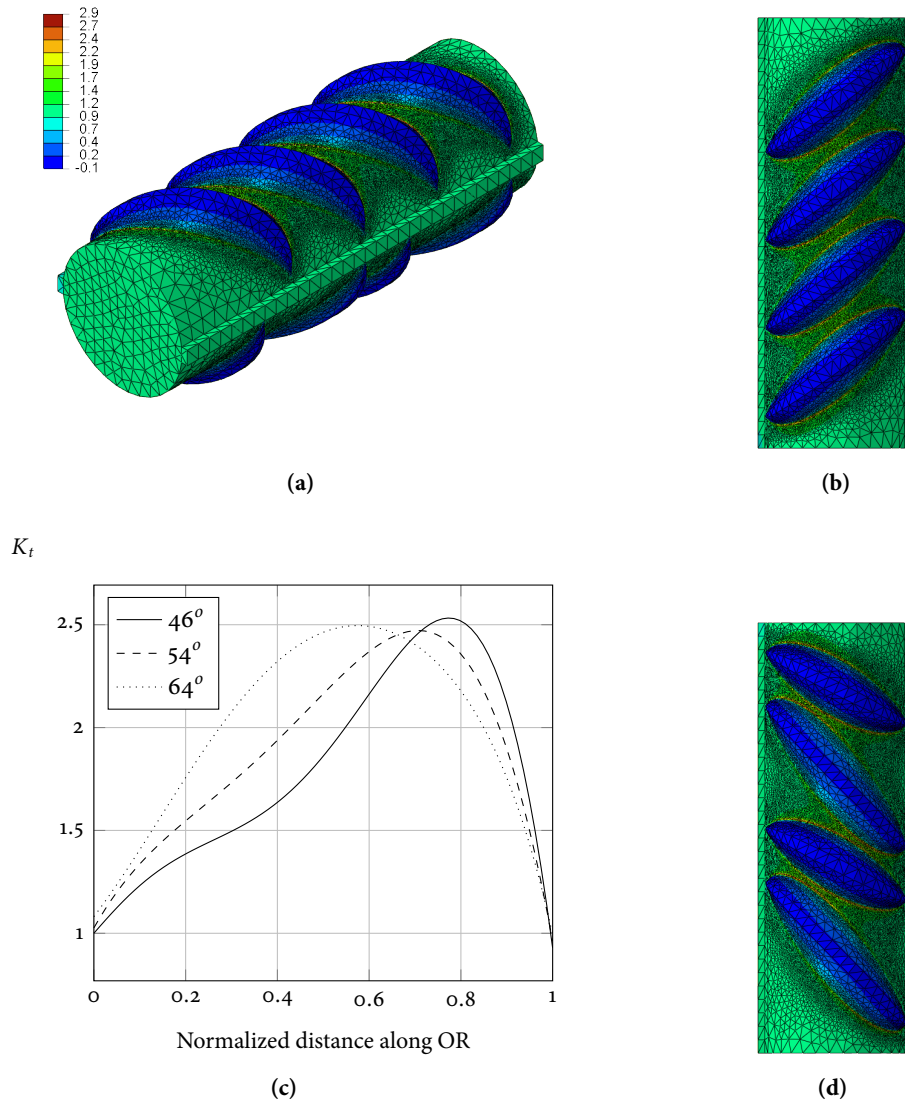


Figure B.17 – D26h15r04 model: (a) 3D FE mesh (b) Top view (c)  $K_t$  plot (d) Bottom view.



## B.17 D26h15r08

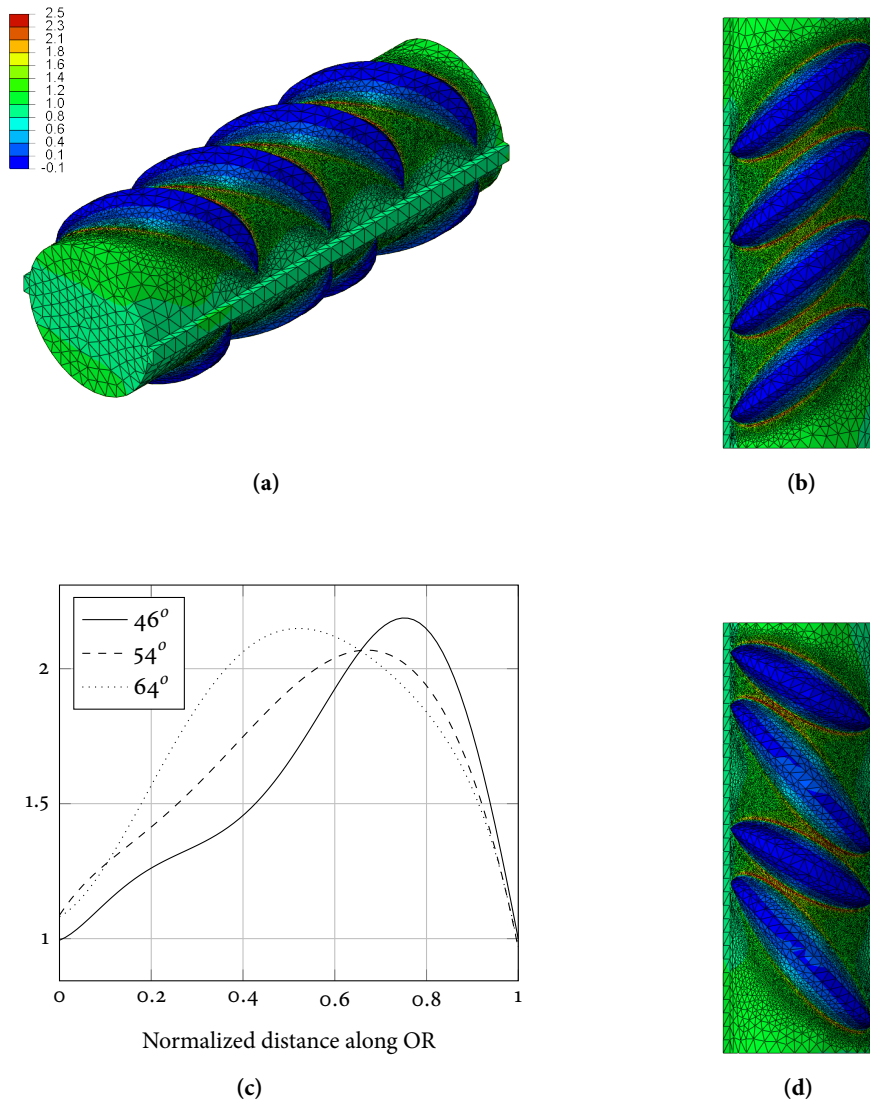
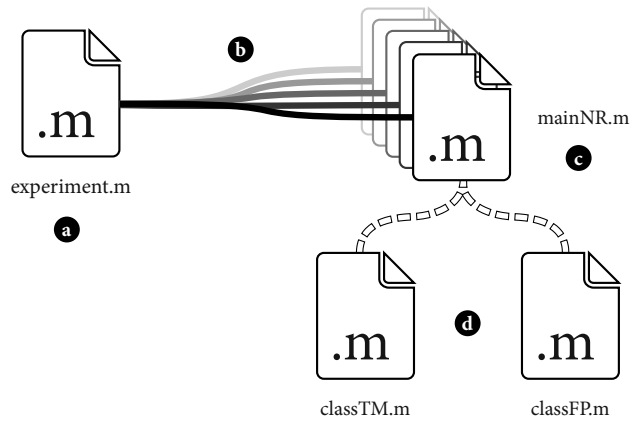


Figure B.18 – D26h15r08 model: (a) 3D FE mesh (b) Top view (c)  $K_t$  plot (d) Bottom view.

**Contents**

C.1	File <code>experiment.m</code> . . . . .	138
C.2	File <code>mainNR.m</code> . . . . .	140
C.3	File <code>classTM.m</code> . . . . .	159
C.4	File <code>classFP.m</code> . . . . .	167

Appendix B presents the algorithm developed for the analytical model used in the analyses given in Chapters 4 and 5.



**Figure C.1** – Model files: (a) file containing the input function to run an experiment; (b) the process will occur simultaneously in parallel on each core; (c) file containing all the function for the Voronoi structure and the propagation algorithm; (d) two files containing a class with properties for each of the two steels: TM & FP.

## C.1 File experiment.m

```
1 % experiment.m file
2 % this is the main input function
3 % Examples:
4 %   experiment(10,400,[180:200],1);
5 %   experiment(10,400,linspace(180,200,1),1);
6
7 function matrix = experiment( N, points, applied.stress, is_martensite )
8
9     matlabpool local;
10
11     number_of_tests = N*numel(applied.stress);
12     matrix = zeros(8,number_of_tests);
13
14     value_time1 = clock;
15
16     value_ten = applied.stress(1);
17     parfor i = 1:3*3
18         mainNR( {value_ten,points}, is_martensite );
19     end
20
21     value_time2 = clock;
22     print_estimation_time(number_of_tests,value_time1,value_time2);
23
24     tic
25
26     % parallel for loop (each step is an experiment)
27     parfor i = 1:number_of_tests
28         current_stress = return_stress(applied.stress,i,N);
29
30         [mem,~] = mainNR( {current_stress,points} , is_martensite );
31
32         matrix(:,i) = [current_stress rot90(mem)];
33     end
34
35     figure;
36     scatter(log10(matrix(2,:)),matrix(1,:),20);
37
38     figure;
39     %plot run-outs by applied stress
40     B=matrix(1:2,:);
41     B=(B==100000000);
42     %get N values
43     Ns=matrix(B);
44     %get S values
45     m1=B(2,:);
46     m2=zeros(7,length(B(2,:)));
47     matrix.select=cat(1,m1,m2);
48     Ss=matrix( matrix.select==1 );
```

```

49     %plot S-N curve
50     hist(cat(1,rot90(Ss)));
51
52     toc
53
54     matrix = rot90(matrix);
55
56     matlabpool close;
57 end
58
59 function result = return_stress(app,i,N)
60     result = app(ceil(i/N));
61 end
62
63 function print_estimation_time(number_of_tests,value_time1,value_time2)
64     init = value_time1(5)*60 + value_time1(6);
65     stop = value_time2(5)*60 + value_time2(6);
66
67     time_int = (stop - init)/(3*3);
68     total = floor(time_int*number_of_tests);
69
70     value_time3 = value_time2;
71     value_time3(4) = floor(total/3600)+value_time3(4);
72     value_time3(5) = floor(mod(total,3600)/60+value_time3(5));
73     value_time3(6) = floor(mod(mod(total,3600),60)+value_time3(6));
74
75     if value_time3(6) >= 60
76         value_time3(5) = value_time3(5) + floor(value_time3(6)/60);
77         value_time3(6) = mod(value_time3(6),60);
78     end
79
80     if value_time3(5) >= 60
81         value_time3(4) = value_time3(4) + floor(value_time3(5)/60);
82         value_time3(5) = mod(value_time3(5),60);
83     end
84
85     if value_time3(4) >= 24
86         value_time3(4) = mod(value_time3(4),24);
87     end
88
89     disp(['-> It will take ',num2str(total),' seconds, for ...
90         ',num2str(number_of_tests),' essays.']);
91     disp(['-> from ',num2str(value_time2(4)), ':', ...
92         num2str(value_time2(5)), ':', num2str(floor(value_time2(6))), ...
93         ' to ', num2str(value_time3(4)), ':', num2str(value_time3(5)), ...
94         ':', num2str(floor(value_time3(6)))]);
95 end

```

## C.2 File mainNR.m

```
1 % mainNR.m file
2 % this is the main input function
3 % Examples:
4 % [NumberCycles, Structure] = mainNR({49, 1000});
5 % and to use an already made "Structure":
6 % [NumberCycles, Structure] = mainNR(Structure);
7
8 function [result_navarro, structure_data] = mainNR( varargin, ...
9           is_martensite )
10
11 %constants
12 global calculus_error;
13 global print_slipbands_during_propagation;
14 global plot_result;
15 global load_orientation;
16 global global_dmean;
17 global number_of_grains_to_break;
18 global propagation_model;
19 global scale_structure;
20
21 result_navarro = zeros(7,1);
22
23 load_orientation = 0;
24 calculus_error = 1.0e-10;
25
26 plot_result = false;
27 print_slipbands_during_propagation = false;
28 number_of_grains_to_break = 10;
29 global_dmean = [0 0];
30 scale_structure = 1;
31
32 linear_propagation=true;
33 second_grain_limit=300;
34
35 %experiment statistics
36 statistics_matrix=ones(2,15,4);
37
38 %tic
39
40 if length(varargin) == 2
41     applied_stress = varargin{1}; point_number = varargin{2};
42     %create the grain structure
43     [V, C, points, sb, maxgrainx, maxgrainy, maxfirstsb] = ...
44         create_structure(point_number);
45 elseif length(varargin) == 11
46     applied_stress = varargin{1}; point_number = varargin{2}; V = ...
47         varargin{3}; C = varargin{4}; points = varargin{5}; sb = ...
48         varargin{6}; maxgrainx = varargin{7}; maxgrainy = varargin{8}; ...
```

```

        maxgrain = varargin{9}; maxfirstsb = varargin{10}; global_dmean ...
        = varargin{11};
45 else
46     return;
47 end
48
49 if is_martensite==1
50     propagation_model = classTM(applied_stress, load_orientation);
51 else
52     propagation_model = classFP(applied_stress, load_orientation);
53 end
54
55 PL_Structure = containers.Map({ - 1, 1}, {struct('grain_id', maxgrain, ...
        'slipband_id', maxfirstsb, 'init_point', points(maxgrain, :), ...
        'end_point', [maxgrainx(1) maxgrainy(1)], 'length', ...
        distance_segment(points(maxgrain, 1), points(maxgrain, 2), ...
        maxgrainx(1), maxgrainy(1)), 'total_length', ...
        distance_segment(points(maxgrain, 1), points(maxgrain, 2), ...
        maxgrainx(1), maxgrainy(1)), 'angle', ...
        get_angle_with_coordinates(points(maxgrain, 1), points(maxgrain, ...
        2), maxgrainx(1), maxgrainy(1)), 'is_border', false), ...
        struct('grain_id', maxgrain, 'slipband_id', maxfirstsb, ...
        'init_point', points(maxgrain, :), 'end_point', [maxgrainx(2) ...
        maxgrainy(2)], 'length', distance_segment(points(maxgrain, 1), ...
        points(maxgrain, 2), maxgrainx(2), maxgrainy(2)), 'total_length', ...
        distance_segment(points(maxgrain, 1), points(maxgrain, 2), ...
        maxgrainx(2), maxgrainy(2)), 'angle', ...
        get_angle_with_coordinates(points(maxgrain, 1), points(maxgrain, ...
        2), maxgrainx(2), maxgrainy(2)), 'is_border', false)});
56 Crack_Structure = containers.Map({0}, {struct('c', 0, 'd_mean', 0, ...
        'nc', 0, 'ac', 0, 'ns', 0, 'dN', 0, 'N', 0, 'is_blocked', false)});
57
58 if plot_result
59     if length(get(0, 'children'))>1
60         figure(2);
61         clf;
62         figure(1);
63         clf;
64     end
65     plot_structure(V, C, points);
66     %plot initial point
67     plot(PL_Structure(1).init_point(1), PL_Structure(1).init_point(2), ...
        '*', 'Color', 'black', 'linewidth', 4);%, 'LineStyle', 'on');
68     %plot slipbands(V, C, points, sb);
69 end
70
71 side_ok = [true true];
72 current_a = [0 0];
73 current_plastified_grain_step = [0 0];
74 lastminDaDN = - 1;
75
76 d_mean_stop = global_dmean(1, 1);

```

```

77
78 while sum(current_a) < number_of_grains_to_break*d.mean_step && ...
    (side_ok(1, 1) == true || side_ok(1, 2) == true)
79
80 if (Crack_Structure(current_plastified_grain_step(1, 1)).N <= ...
    Crack_Structure(current_plastified_grain_step(1, 2)).N && ...
    (side_ok(1, 1) == true && side_ok(1, 2) == true)) || ...
    (side_ok(1, 1) == true && side_ok(1, 2) == false)
81     index = 1;
82     current_plastified_grain_step(1, index) = ...
        current_plastified_grain_step(1, index)+1;
83 else
84     index = 2;
85     current_plastified_grain_step(1, index) = ...
        current_plastified_grain_step(1, index)-1;
86 end
87
88 if plot_result
89     plot_plastic_zone(current_plastified_grain_step(1, index), ...
        PL_Structure);
90 end
91
92 PL_Structure = preferential_line(V, C, sb, PL_Structure, ...
    current_plastified_grain_step(1, index));
93 [propagation_model, Crack_Structure, side_ok_res, matrix_disp] = ...
    propagation_model.is_propagating(current_plastified_grain_step(1, ...
    index), current_plastified_grain_step(1, mod(index, 2)+1), ...
    side_ok, Crack_Structure, PL_Structure);
94
95 %statistics
96 statistics_matrix(index, abs(current_plastified_grain_step(1, ...
    index)), :) = matrix_disp;
97
98 if plot_result
99     disp(['PLASTIC ZONE: ', ...
        num2str(current_plastified_grain_step(1, index))]);
100     disp(PL_Structure(current_plastified_grain_step(1, index)));
101     disp(['CRACK INCREMENT: ', ...
        num2str(current_plastified_grain_step(1, index))]);
102     disp(Crack_Structure(current_plastified_grain_step(1, index)));
103 end
104
105 %when dN<=0, don't compute the dadN function
106 if plot_result && side_ok(1, index) == true && ...
    Crack_Structure(current_plastified_grain_step(1, index)).dN<=0
107     side_ok(1, index) = false;
108     if index == 1;
109         current_plastified_grain_step(1, index) = ...
            current_plastified_grain_step(1, index)-1;
110     else
111         current_plastified_grain_step(1, index) = ...
            current_plastified_grain_step(1, index)+1;

```

```

112         end
113     end
114
115     if ((Crack_Structure(current_plastified_grain_step(1, 1)).N<= ...
        Crack_Structure(current_plastified_grain_step(1, 2)).N) && ...
        (side_ok(1, 1) == true && side_ok(1, 2) == true)) || ~...
        (side_ok(1, 1) == true && side_ok(1, 2) == true)
116         current_a(1, 1) = ...
            Crack_Structure(current_plastified_grain_step(1, 1)).ac;
117     end
118     if ((Crack_Structure(current_plastified_grain_step(1, 2)).N<= ...
        Crack_Structure(current_plastified_grain_step(1, 1)).N) && ...
        (side_ok(1, 1) == true && side_ok(1, 2) == true)) || ~...
        (side_ok(1, 2) == true && side_ok(1, 1) == true)
119         current_a(1, 2) = ...
            Crack_Structure(current_plastified_grain_step(1, 2)).ac;
120     end
121
122     if plot_result && abs(current_plastified_grain_step(1, 1))>0 && ...
        abs(current_plastified_grain_step(1, 2))>0
123         lastminDaDN = plotdadN(current_plastified_grain_step, ...
            Crack_Structure, PL_Structure, lastminDaDN);
124     end
125
126     %update here for the next step only (when the fracture stops or
127     %arrives at the border
128     side_ok = side_ok_res;
129     if plot_result && side_ok(1, index) == false
130         disp(['The crack stops at step ', ...
            num2str(current_plastified_grain_step(1, index))]);
131     end
132     if PL_Structure(current_plastified_grain_step(1, index)).is_border ...
        == true
133         side_ok(1, index) = false;
134         if plot_result
135             disp(['The crack arrives at the border at step ', ...
                num2str(current_plastified_grain_step(1, index))]);
136         end
137     end
138
139     if plot_result && abs(current_plastified_grain_step(1, 1))>0 && ...
        abs(current_plastified_grain_step(1, 2))>0
140         d_mean_stop = (abs(current_plastified_grain_step(1, ...
            1))*Crack_Structure(current_plastified_grain_step(1, ...
            1)).d_mean+abs(current_plastified_grain_step(1, ...
            2))*Crack_Structure(current_plastified_grain_step(1, ...
            2)).d_mean)/(abs(current_plastified_grain_step(1, ...
            1))+abs(current_plastified_grain_step(1, 2)));
141     end
142
143     %store the value when the first grain breaks
144     if abs(current_plastified_grain_step(1, 1))==1 && ...

```



```

    abs(current_plastified_grain_step(1, 2))==1
145     result_navarro(2) = ...
        max([Crack_Structure(current_plastified_grain_step(1, ...
            1)).dN Crack_Structure(current_plastified_grain_step(1, ...
            2)).dN]);
146     end
147 end
148
149 if PL_Structure(current_plastified_grain_step(1, 1)).is_border
150     side_ok(1, 1) = true;
151 elseif PL_Structure(current_plastified_grain_step(1, 2)).is_border
152     side_ok(1, 2) = true;
153 end
154
155 Ntotal = max([Crack_Structure(current_plastified_grain_step(1, 1)).N ...
    Crack_Structure(current_plastified_grain_step(1, 2)).N]);
156
157 if side_ok(1, 1) == true || side_ok(1, 2) == true
158     if plot_result
159         disp(['Propagation part: it breaks at N_propa = ', ...
            num2str(Ntotal, '%10.5e\n')]);
160     end
161 else
162     Ntotal = 10^8;
163     if plot_result
164         disp(['Propagation part: the cracks stops before N = ', ...
            num2str(Ntotal, '%10.5e\n')]);
165     end
166 end
167
168 %statistics
169 result_navarro(1) = Ntotal;
170 result_navarro(3) = Ntotal;
171 if(Crack_Structure(current_plastified_grain_step(1, ...
    1)).N>Crack_Structure(current_plastified_grain_step(1, 2)).N)
172     stat_mat=statistics_matrix(1,1:abs(current_plastified_grain_step(1, ...
        1)),:);
173     stat_mat=reshape(stat_mat,[abs(current_plastified_grain_step(1, ...
        1)) 4]);
174 else
175     stat_mat=statistics_matrix(2,1:abs(current_plastified_grain_step(1, ...
        2)),:);
176     stat_mat=reshape(stat_mat,[abs(current_plastified_grain_step(1, ...
        2)) 4]);
177 end
178 result_navarro(4)=sum(stat_mat(:,1));
179 result_navarro(5)=sum(stat_mat(:,2));
180 result_navarro(6)=sum(stat_mat(:,3));
181 result_navarro(7)=sum(stat_mat(:,4));
182
183 structure_data = {applied_stress, point_number, V, C, points, sb, ...
    maxgrainx, maxgrainy, maxgrain, maxfirstsb, global_dmean};

```

```

184 %toc
185
186 %linear propagation
187 if linear_propagation==true && (side_ok(1, 1) == true || side_ok(1, 2) ...
    == true)
188     c=[Crack.Structure(current_plastified_grain_step(1, 1)).c ...
        Crack.Structure(current_plastified_grain_step(1, 2)).c];
189     nc=[Crack.Structure(current_plastified_grain_step(1, 1)).nc ...
        Crack.Structure(current_plastified_grain_step(1, 2)).nc];
190     ns=[0 0];
191     dN=[0 0];
192     while abs(current_plastified_grain_step(1, ...
        1))+abs(current_plastified_grain_step(1, ...
        2))<second_grain_limit && (side_ok(1, 1) == true || side_ok(1, ...
        2) == true)
193
194         for t=[-1 1]
195             index_side = 1+(1-sign(t))/2;
196             if side_ok(1, index_side) == true
197                 ns(index_side)=c(index_side)/(c(index_side) + ...
                    d_mean_stop)*nc(index_side);
198                 c(index_side)=c(index_side)+d_mean_stop;
199                 current_plastified_grain_step(1, index_side) = ...
                    current_plastified_grain_step(1, index_side)+t;
200                 [dnRes,ncRes] = propagation_model.compute_long_crack( ...
                    current_plastified_grain_step(1, index_side), c( ...
                    index_side), d_mean_stop, ns(index_side));
201                 dN(index_side)=dN(index_side)+dnRes;
202                 nc(index_side)=ncRes;
203
204                 if plot_result
205                     disp(['CRACK INCREMENT: ', ...
                        num2str(current_plastified_grain_step(1, ...
                        index_side))]);
206                 end
207             end
208         end
209
210     end
211     result_navarro(1)=result_navarro(1)+max(dN);
212
213     if plot_result
214         disp(['Linear part: N_linear = ', num2str(max(dN), '%10.5e\n')]);
215     end
216
217 end
218
219 end
220
221 function plot_plastic_zone(k, PL.Structure)
222 if ~isempty(get(0, 'children'))
223     figure(1);

```

```

224 else
225     figure('Name', 'Grain structure');
226 end
227
228 %for step 1 or - 1, the plastic zone is all the grain.
229 if abs(k) == 1
230     plot([PL.Structure(1).end_point(1) PL.Structure(-1).end_point(1)], ...
          [PL.Structure(1).end_point(2) PL.Structure(-1).end_point(2)], ...
          'Color', [0 0 0], 'linewidth', 4);%, 'LineSmoothing', 'on');
231 else
232     plot([PL.Structure(k).init_point(1) PL.Structure(k).end_point(1)], ...
          [PL.Structure(k).init_point(2) PL.Structure(k).end_point(2)], ...
          'Color', [0 0 0], 'linewidth', 4);%, 'LineSmoothing', 'on');
233 end
234 end
235
236 function plot_crack(a_p, a_m, PL.Structure)
237 if ~isempty(get(0, 'children'))
238     figure(1);
239 else
240     figure('Name', 'Grain structure');
241 end
242
243 for i = [1 -1]
244     current_length = 0;
245     if i == 1
246         a = a_p;
247         grain_id = 1;
248     else
249         a = a_m;
250         grain_id = - 1;
251     end
252     if numel(a)>1
253         while current_length<a(2)
254             new_length = current_length+PL.Structure(grain_id).length;
255             if a(1)<= new_length
256                 if a(1)>= current_length && a(1)<new_length
257                     prop_coef = (a(1) - ...
                                   current_length)/PL.Structure(grain_id).length;
258                     points1 = [( PL.Structure(grain_id).end_point(1) - ...
                                   PL.Structure(grain_id).init_point(1) ...
                                   )*prop_coef + ...
                                   PL.Structure(grain_id).init_point(1) ( ...
                                   PL.Structure(grain_id).end_point(2) - ...
                                   PL.Structure(grain_id).init_point(2) ...
                                   )*prop_coef + ...
                                   PL.Structure(grain_id).init_point(2)];
259                 else
260                     points1 = PL.Structure(grain_id).init_point;
261                 end
262                 if a(2)>= current_length && a(2)<new_length
263                     prop_coef = (a(2) - ...

```

```

                current_length)/PL.Structure(grain_id).length;
264         points2 = [( PL.Structure(grain_id).end_point(1) - ...
                    PL.Structure(grain_id).init_point(1) ...
                    )*prop_coef + ...
                    PL.Structure(grain_id).init_point(1) ( ...
                    PL.Structure(grain_id).end_point(2) - ...
                    PL.Structure(grain_id).init_point(2) ...
                    )*prop_coef + ...
                    PL.Structure(grain_id).init_point(2)];
265         else
266             points2 = PL.Structure(grain_id).end_point;
267         end
268         if sign(i) == - 1, color = 'red'; else color = 'blue'; ...
            end;
269         plot([points1(1) points2(1)], [points1(2) points2(2)], ...
                'Color', 'white');
270     end
271     current_length = current_length+PL.Structure(grain_id).length;
272     grain_id = grain_id+1*i;
273     end
274 end
275 end
276 end
277
278 function mindaN = plotdadN(steps, Crack.Structure, PL.Structure, mindaN)
279
280 global propagation_model;
281
282 if length(get(0, 'children'))>1
283     figure(2);
284 else
285     figure('Name', 'da/dN');
286 end
287
288 offset_alone = 0;%when the loop is only k
289
290 minX = [0 0];
291 maxX = [0 0];
292
293 if Crack.Structure(steps(1, 1)).N >= Crack.Structure(steps(1, 2)).N
294     k = steps(1, 1);l = steps(1, 2);
295 else
296     k = steps(1, 2);l = steps(1, 1);
297 end
298
299 %lap length computations
300 if Crack.Structure(k - sign(k)).N > Crack.Structure(l).N
301     loop = k;
302     %when a crack stops, fill the gap
303     if Crack.Structure(k - 2*sign(k)).N <= Crack.Structure(l).N
304         [propagation_model, minX(1)] = ...
            propagation_model.crack_position_by_dN(Crack.Structure(l).N ...

```

```

- Crack_Structure(k - 2*sign(k)).N , Crack_Structure(k - ...
sign(k)).ns, Crack_Structure(k - sign(k)).c, k - sign(k), ...
l, Crack_Structure, PL_Structure);
305 else
306     minX(1) = Crack_Structure(k - sign(k)).ac;
307 end
308     maxX(1) = Crack_Structure(k).ac;
309     offset_alone = Crack_Structure(l).ac;
310 else
311     loop = [k l];
312     if Crack_Structure(k - sign(k)).N >= Crack_Structure(l - sign(l)).N
313         minX(1) = Crack_Structure(k - sign(k)).ac;
314         maxX(2) = Crack_Structure(l).ac;
315         %compute minX for l, when N = N(k - 1)
316         [propagation_model, minX(2)] = ...
            propagation_model.crack_position_by_dN(Crack_Structure(k - ...
            sign(k)).N - Crack_Structure(l - sign(l)).N , ...
            Crack_Structure(l).ns, Crack_Structure(l).c, l, k - ...
            sign(k), Crack_Structure, PL_Structure);
317         %compute maxX for k, when N = N(l)
318         [propagation_model, maxX(1)] = ...
            propagation_model.crack_position_by_dN(Crack_Structure(l).N ...
            - Crack_Structure(k - sign(k)).N , Crack_Structure(k).ns, ...
            Crack_Structure(k).c, k, l, Crack_Structure, PL_Structure);
319     else %all l - N segments are inside the k - N segment
320         minX(2) = Crack_Structure(l - sign(l)).ac;
321         maxX(2) = Crack_Structure(l).ac;
322         [propagation_model, minX(1)] = ...
            propagation_model.crack_position_by_dN(Crack_Structure(l - ...
            sign(l)).N - Crack_Structure(k - sign(k)).N , ...
            Crack_Structure(k).ns, Crack_Structure(k).c, k, l - ...
            sign(l), Crack_Structure, PL_Structure);
323         [propagation_model, maxX(1)] = ...
            propagation_model.crack_position_by_dN(Crack_Structure(l).N ...
            - Crack_Structure(k - sign(k)).N , Crack_Structure(k).ns, ...
            Crack_Structure(k).c, k, l, Crack_Structure, PL_Structure);
324     end
325 end
326
327     numb_int_points = 10;
328     X = [1:numb_int_points];
329     Y = zeros(numb_int_points, 1);
330     if size(loop) == 1
331         if sign(k) == 1, color = 'blue'; else color = 'red'; end;
332     else
333         if sign(k) == 1, color = 'red'; else color = 'blue'; end;
334     end
335
336     factorToMeterByCycle = 10^-3; %because unity in Mpa (N/mm2)
337
338     if sum(maxX) ~= 0
339         for p = 1:numel(loop)

```

```

340     i = loop(p);
341     step = (maxX(p) - minX(p))/(numb_int_points - 1);
342     for j = 1:numb_int_points
343         a = minX(p)+(j - 1)*step;
344         [propagation_model, newdadn] = propagation_model.dadN(a, ...
345             a/Crack_Structure(i).c, k, l, Crack_Structure, ...
346             PL_Structure);
347         Y(j) = Y(j)+newdadn;
348     end
349     plot(sum(minX)+(sum(maxX) - sum(minX))/(numb_int_points - 1)*(X - ...
350         1) +offset_alone, (Y*factorToMeterByCycle), 'black');
351 end
352 if mindaDN>0
353     plot([sum(minX)+offset_alone sum(minX)+offset_alone], ([mindaDN ...
354         Y(1)]*factorToMeterByCycle), 'black');
355 end
356 %grain boundaries
357 hold on;
358 X2 = (([Crack_Structure(k).c+Crack_Structure(l).c ...
359     Crack_Structure(k).c+Crack_Structure(l).c]));
360 Y2 = ([min(Y) max(Y)]*factorToMeterByCycle);
361 plot(X2, Y2, '--', 'Color', color);
362 %plot crack
363 if sign(k) == 1
364     plot_crack([minX(1) maxX(1)], [minX(2) maxX(2)], PL_Structure);
365 else
366     plot_crack([minX(2) maxX(2)], [minX(1) maxX(1)], PL_Structure);
367 end
368 mindaDN = min(Y);
369 end
370 %create the voronoi structure
371 function [V, C, points, sb, first_slip_band_x, first_slip_band_y, ...
372     init_grain_id, maxfirstsb_angle_index] = ...
373     create_structure(point_number)
374 points = zeros(point_number, 2);
375 maxfirstsb_angle_index = -1;
376 %here to change the grain structure
377 for a = 1:point_number
378     %pointx(a) = random('norm', 0.5, 0.2);
379     %random
380     points(a, 1) = random('unif', -0.5, 1.5);
381     points(a, 2) = random('unif', -0.5, 1.5);
382     %hexa
383     %offset = mod(floor(a/sqrt(point_number)), 2)/sqrt(point_number);

```

```

385     %points(a, 2) = 2.0*floor(a/sqrt(point_number))/sqrt(point_number) ...
        - 0.5+1/sqrt(point_number);
386     %points(a, 1) = 2.0*mod(a, sqrt(point_number))/sqrt(point_number) ...
        - 0.5+offset;
387     %square
388     %points(a, 1) = 2.0*floor(a/sqrt(point_number))/sqrt(point_number) ...
        - 0.5;
389     %points(a, 2) = 2.0*mod(a, sqrt(point_number))/sqrt(point_number) ...
        - 0.5;
390     %web
391     %points(a, 1) = 2.0*floor(a/sqrt(point_number))/sqrt(point_number) ...
        - ...
        0.5+2.0*floor(a/sqrt(point_number))/sqrt(point_number)/2.0*mod(a, ...
        sqrt(point_number));
392     %points(a, 2) = 2.0*mod(a, sqrt(point_number))/sqrt(point_number) ...
        - 0.5;
393 end
394
395 global scale_structure;
396 %scale_structure = 10^ - 3;
397 points = points*scale_structure;
398
399 [V, C] = voronoin(points);
400
401 %sb = slip bands
402 %psb = first slip band
403 number_of_slip_band = 3;
404 sb = zeros(point_number, number_of_slip_band);
405 for a = 1:point_number
406     %psb = 0;
407     psb = random('unif', 0.0, pi/number_of_slip_band);
408     for k = 1:number_of_slip_band
409         sb(a, k) = psb+(k - 1)*pi/number_of_slip_band;
410     end
411 end
412
413 maxlc = 0;
414 init_grain_id = 0;
415
416 first_slip_band_x = 0;
417 first_slip_band_y = 0;
418
419 for grain = 1:point_number
420     if points(grain, 1)>0 && points(grain, 2)>0 && points(grain, ...
421         1)<1*scale_structure && points(grain, 2)<1*scale_structure
422         [grainx, grainy, sb_index, sb_angle] = find_slip_band( V, C, ...
423             grain, sb(grain, :), points(grain, 1), points(grain, 2), ...
424             [], 0 );
425         if numel(grainx)>1
426             sb_length = distance_segment(grainx(1), grainy(1), ...
427                 grainx(2), grainy(2));

```

```

425
426         %compute lc
427         lc = abs(sb.length*cos(2*(pi/4 - (sb(grain, sb_index)))));
428
429         if lc>maxlc
430             maxlc = lc;
431             init_grain_id = grain;
432             first_slip_band_x = grainx;
433             first_slip_band_y = grainy;
434             maxfirstsb_angle_index = sb_index;
435         end
436     end
437 end
438 end
439
440 %compute the global grain mean size here
441 global global_dmean;
442 global_dmean(1, 1) = global_dmean(1, 1)/global_dmean(1, 2);
443
444 end
445
446 %plot the voronoi structure
447 function plot_structure(V, C, points)
448
449     %global scale_structure;
450     scale_structure = 1;
451
452     if length(get(0, 'children'))>1
453         figure(1);
454     else
455         figure('Name', 'Grain structure');
456     end
457
458     for a = 1:length(points(:, 1))
459         hold on;
460         if (a>1)
461             %plot(pointx(a - 1:a), pointy(a - 1:a));
462         end
463         %text(points(a, 1), points(a, 2), num2str(a), 'FontSize', 8, ...
464             'Color', 'black');
465     end
466
467     hold on;
468     %plot(points(:, 1), points(:, 2), '*', 'Color', 'k', 'MarkerSize', 2);
469
470     %plot grain: if convhull raises an error, other method to draw the points.
471     try
472         for k = 1:length(C)
473             if all(C{k}~= 1)
474                 VertCell = V(C{k}, :);
475                 KVert = convhulln(VertCell);
476                 patch('Vertices', VertCell, 'Faces', KVert, ...

```



```

        'FaceVertexCData', hsv(1), 'FaceColor', 'flat', ...
        'EdgeColor', [0 0 0], 'LineWidth', ...
        0.1);%'LineSmoothing', 'on');
476     end
477   end
478 catch errN
479   for j = 1:length(C)
480     b = C{j, :};
481     number_vert = size(b);
482     for i = 1:number_vert(2)
483       hold on;
484       if (i>1)
485         plot([V(b(i-1), 1) V(b(i), 1)], [V(b(i-1), 2) V(b(i), ...
486           2)], 'Color', [0 0 0], 'LineWidth', 0.1);
487       else
488         plot([V(b(1), 1) V(b(number_vert(2)), 1)], [V(b(1), 2) ...
489           V(b(number_vert(2)), 2)], 'Color', [0 0 0], ...
490           'LineWidth', 0.1);
491       end
492     end
493   end
494 end
495
496
497 %plot the slipbands
498 function plot_slipbands(V, C, points, sb)
499 for grain = 1:length(points(:, 1))
500   find_slip_band( V, C, grain, sb(grain, :), points(grain, 1), ...
501     points(grain, 2), [], true );
502 end
503
504 %find the equation of the line
505 function [A, B] = line_equation( X, Y )
506 A = (Y(1) - Y(2))/(X(1) - X(2));
507 B = Y(2) - A*X(2);
508 end
509
510 %give the length of the segment
511 function length_seg = distance_segment(x1, y1, x2, y2)
512 length_seg = sqrt((x1 - x2)^2 + (y1 - y2)^2);
513 end
514
515 %give the next grain
516 function boundary_grain = find_next_grain( V, C, grain, x_inter, ...
517   y_inter )
518
519 global calculus_error;

```

```

520 boundary_grain = 0;
521
522 test = C{grain, :};
523 tamanho = size(test);
524
525 %loop on vertices
526 for i = 1:tamanho(2)
527
528     x1 = V(test(i), 1);
529     y1 = V(test(i), 2);
530     first_point = test(i);
531
532     if i == tamanho(2)
533         x2 = V(test(1), 1);
534         y2 = V(test(1), 2);
535         second_point = test(1);
536     else
537         x2 = V(test(i+1), 1);
538         y2 = V(test(i+1), 2);
539         second_point = test(i+1);
540     end
541
542     %check if the line is/not vertical
543     if abs(x1 - x2) < calculus_error
544         erro = abs(x_inter - x1);
545     else
546         [A, B] = line_equation([x1 x2], [y1 y2]);
547         erro = abs(A*x_inter+B - y_inter);
548     end
549
550     %disp(['erro ' , num2str(erro)]);
551
552     if erro < calculus_error
553
554         for j = 1:length(C)
555             tem_first_point = 0;
556             tem_second_point = 0;
557             vertices_list = C{j, :};
558             tamanhoc = size(vertices_list);
559             for k = 1:tamanhoc(2)
560                 if vertices_list(k) == first_point
561                     tem_first_point = 1;
562                 elseif vertices_list(k) == second_point
563                     tem_second_point = 1;
564                 end
565             end
566             if tem_first_point == 1 && tem_second_point == 1 && grain ~...
567                 = j
568                 boundary_grain = j;
569             end
570         end

```

```

571
572     end
573
574 end
575
576 end
577
578 %choose the next slipband
579 function [maxgrainx, maxgrainy, slip_band_index, ...
        slip_band_oriented_angle] = find_slip_band( V, C, grain, anglesb, ...
        x_init, y_init, first_step_sb, print )
580
581 maxlc = 0;
582 minlc = pi;
583 slip_band_index = 0;
584 slip_band_oriented_angle = 0;
585
586 global calculus_error;
587 global load_orientation;
588 global global_dmean;
589 %global scale_structure;
590 scale_structure = 1;
591
592 maxgrainx = 0;
593 maxgrainy = 0;
594
595 b = C{grain, :};
596 tamanho = size(b);
597 tamanho = tamanho(2);
598
599 vgx = zeros(tamanho+1, 1);
600 vgy = zeros(tamanho+1, 1);
601
602 for i = 1:tamanho
603     vgx(i) = V(b(i), 1);
604     vgy(i) = V(b(i), 2);
605 end
606
607 %close the grain
608 vgx(tamanho+1) = V(b(1), 1);
609 vgy(tamanho+1) = V(b(1), 2);
610
611 for sbg = 1:length(anglesb)
612     linex = [cos(anglesb(sbg))+x_init cos(anglesb(sbg)+pi)+x_init];
613     liney = [sin(anglesb(sbg))+y_init sin(anglesb(sbg)+pi)+y_init];
614
615     [xi, yi] = polyxpoly(vgx, vgy, linex, liney);
616
617     if length(xi)>1 && max(abs(max(vgx - 0.5*scale_structure)), ...
        abs(min(vgx - 0.5*scale_structure))) <= 1.0*scale_structure && ...
        max(abs(max(vgy - 0.5*scale_structure)), abs(min(vgy - ...
        0.5*scale_structure))) <= 1.0*scale_structure %p assegurar que ...

```

```

618
619
620
621
622
623
624
625
626
627
628
629
630
631
632
633
634
635
636
637
638
639
640
641
642
643
644
645
646
647
648
649
650
651
652
653
654
655
656
657
658
659

```

todas as linhas formam um polígono fechado

```

if abs(xi(2) - x_init) < calculus_error
    %disp(['need to invert the matrix init (' , ...
        num2str(x_init), ', ', num2str(y_init), ') and ...
        xi(2):', num2str(xi(2))]);
    temp_x = [xi(2) xi(1)];
    temp_y = [yi(2) yi(1)];
    xi = temp_x;
    yi = temp_y;
end

%plot(vgx, vgy, 'Color', 'green');
if print == true
    if isempty(first_step_sb) == true
        plot(xi, yi, ':', 'Color', [1 1 1]);%, ...
            'LineStyle', 'solid');
    else
        plot(xi, yi, '--', 'Color', [0.5 0.5 0.5]);%, ...
            'LineStyle', 'solid');
    end
end

if isempty(first_step_sb) == true %draw slipband from the ...
    center of the grain

    sb_length = distance_segment(xi(1), yi(1), xi(2), yi(2));

    lc = abs(sb_length*cos(2*(pi/4 - (anglesb(sbg) - ...
        load_orientation)))));

    global_dmean(1, 2) = global_dmean(1, 2)+1;
    global_dmean(1, 1) = global_dmean(1, 1)+sb_length;

    if lc>maxlc
        maxlc = lc;
        maxgrainx = xi;
        maxgrainy = yi;
        slip_band_index = sbg;
        slip_band_oriented_angle = anglesb(sbg);
    end
end

else

    macroangle = get_angle_with_coordinates(xi(1), yi(1), ...
        xi(2), yi(2));
    ref_angle = get_angle_with_coordinates(first_step_sb(1), ...
        first_step_sb(2), first_step_sb(3), first_step_sb(4));

    %find the closest shear stress plane
    shear_stress_dir = [ -3*pi/4-load_orientation ...
        -pi/4-load_orientation pi/4-load_orientation ...

```

```

        3*pi/4-load_orientation ];
660     [C, I] = min(compute_angle_diff(shear_stress_dir, ref_angle));
661     ref_angle = shear_stress_dir(I);
662
663     lc = compute_angle_diff(ref_angle, macroangle);
664
665     if lc > pi
666         lc = 2*pi - lc;
667     end
668
669     if lc <= minlc
670         minlc = lc;
671         maxgrainx = xi;
672         maxgrainy = yi;
673         slip_band_index = sbg;
674         slip_band_oriented_angle = macroangle;
675     end
676
677     end
678 end
679 end
680
681 end
682
683 function result = compute_angle_diff(angle1, angle2)
684 result = abs(sin(angle1) - sin(angle2)) + abs(cos(angle1) - cos(angle2));
685 end
686
687 function angle = get_angle_with_coordinates(x1, y1, x2, y2)
688 angle = atan((y2 - y1)/(x2 - x1));
689 % as atan give result between pi/2 and - pi/2, update here:
690 if y1 < y2 && x1 > x2
691     angle = angle + pi;
692 elseif y1 >= y2 && x1 > x2
693     angle = angle - pi;
694 end
695 end
696
697 %find the preferential line ie composed by several grains
698 function PL_Structure = preferential_line(V, C, sb, PL_Structure, step)
699 global print_slipbands_during_propagation;
700 global plot_result;
701
702 if plot_result
703     if ~isempty(get(0, 'children'))
704         figure(1);
705     else
706         figure('Name', 'Grain structure');
707     end
708 end
709
710 function [next_grain_id, sb_id, pointx, pointy, sb_length, ...

```

```

    sb.angle, will_pro] = next_grain_slipband(current_grain, ...
    current_pointx, current_pointy)
711 will_pro = true;
712 sb.id = 0;
713 pointx = 0;
714 pointy = 0;
715 sb.length = 0;
716 sb.angle = 0;
717
718 next_grain_id = find_next_grain( V, C, current_grain, ...
    current_pointx, current_pointy );
719
720 if next_grain_id ~= 0
721     [pointx, pointy, sb.id, sb.angle] = find_slip_band( V, C, ...
        next_grain_id, sb(next_grain_id, :), current_pointx, ...
        current_pointy, ...
        [PLStructure(1*sign(step)).init_point(1), ...
        PLStructure(1*sign(step)).init_point(2), ...
        PLStructure(1*sign(step)).end_point(1), ...
        PLStructure(1*sign(step)).end_point(2)], ...
        print_slipbands_during_propagation );
722 else
723     will_pro = false;
724 end
725
726 if numel(pointx)>1 && numel(pointy)>1 && will_pro == true
727     sb.length = distance_segment(pointx(1), pointy(1), ...
        pointx(2), pointy(2));
728 else
729     will_pro = false;
730 end
731 end
732
733 [next_grain, next_sb_id, next_points_x, next_points_y, next_sb_length, ...
    next_sb_angle, lado_ok] = next_grain_slipband( ...
    PLStructure(step).grain_id, PLStructure(step).end_point(1), ...
    PLStructure(step).end_point(2) );
734 if next_grain ~= 0 && numel(next_points_x)>1 && numel(next_points_y)>1
735     PLStructure(step+sign(step)) = struct('grain_id', next_grain, ...
        'slipband_id', next_sb_id, 'init_point', [next_points_x(1) ...
        next_points_y(1)], 'end_point', [next_points_x(2) ...
        next_points_y(2)], 'length', next_sb_length, 'total_length', ...
        PLStructure(step).total_length+next_sb_length, 'angle', ...
        next_sb_angle, 'is_border', next_grain == 0);
736 else
737     PLStructure(step) = struct('grain_id', ...
        PLStructure(step).grain_id, 'slipband_id', ...
        PLStructure(step).slipband_id, 'init_point', ...
        PLStructure(step).init_point, 'end_point', ...
        PLStructure(step).end_point, 'length', ...
        PLStructure(step).length, 'total_length', ...
        PLStructure(step).total_length, 'angle', ...

```

```
PLStructure(step).angle, 'is.border', true);  
738 end  
739  
740 end
```

### C.3 File classTM.m

```
1 % classTM.m class
2 % this is the class for Martensite
3
4 classdef classTM
5
6     properties (SetAccess = private, GetAccess = public)
7
8         applied_stress_;
9         load_direction;
10
11         materialDist = [100];
12
13         sigFL_ = [368/2];
14         surfRoughnessVariance_ = normrnd(1.0,0.1);
15
16         sigComp_ = [284];%Martensite: medium carbon steel 0.4C, 142*2
17         nu_ = [0.29];%Martensite
18         G_ = [79*10^3];%Martensite
19
20         propertiesArray = ones(350,8)*(-1);
21
22     end
23
24     methods ( Access = private )
25
26         function [self,res] = getValueByDist(self,i,propertyIndex)
27             current_index=1+(1-sign(i))/2;
28             if ...
29                 self.propertiesArray(abs(i),(propertyIndex-1)*2+current_index)==-1
30                 %for the first time, compute and store the value
31                 if propertyIndex==1
32                     matrixValue=self.sigFL_;
33                 elseif propertyIndex==2
34                     matrixValue=self.sigComp_;
35                 elseif propertyIndex==3
36                     matrixValue=self.nu_;
37                 elseif propertyIndex==4
38                     matrixValue=self.G_;
39                 end
40                 %half the crack for both side
41                 grainNumber=ceil(1+3*(abs(i)-1)/2);
42                 r_ = randi(100,1,grainNumber);
43                 a = self.materialDist;
44                 c_ = cell2mat(arrayfun(@(a,matrixValue) ...
45                     matrixValue+zeros(1,a), a, matrixValue, 'unif', 0));
46                 self.propertiesArray(abs(i),(propertyIndex-1)*2 + ...
47                     current_index) = mean(c_(r_));
48             if (abs(i)==1)%for the first grain, the values are the ...
```



```

46         same
47         self.propertiesArray(abs(i), (propertyIndex-1)*2 + ...
48             1 + (1-sign(-i))/2) = mean(c_-(r_));
49     end
50     res = self.propertiesArray(abs(i), (propertyIndex-1)*2 ...
51         + current_index);
52 else
53     %get the value if it was already computed
54     res = self.propertiesArray(abs(i), (propertyIndex-1)*2 ...
55         + current_index);
56 end
57
58 function [self, res] = sigFL(self, i)
59     %disp(['sigFL', num2str(i)]);
60     [self, res]=self.getValueByDist(i, 1);
61 end
62
63 function [self, res] = sigComp(self, i)
64     %disp(['sigComp', num2str(i)]);
65     [self, res]=self.getValueByDist(i, 2);
66 end
67
68 function [self, res] = nu(self, i)
69     %disp(['nu', num2str(i)]);
70     [self, res]=self.getValueByDist(i, 3);
71 end
72
73 function [self, res] = G(self, i)
74     %disp(['G', num2str(i)]);
75     [self, res]=self.getValueByDist(i, 4);
76 end
77
78 function [self, res] = f(self, i)
79     [self, sigFLTemp] = self.sigFL(i);
80     [self, sigCompTemp] = self.sigComp(i);
81
82     if self.applied.stress > sigFLTemp
83         res = 8.3044*10^(-20)*(self.applied.stress_)^6.8132;
84     else
85         res=0;
86     end
87 end
88
89 function res = applied_stress(self, i)
90     res = self.applied.stress_;
91 end
92
93 function [self, res] = phi(self, a, n, i)
94     [self, nuTemp] = self.nu(i);
95     [self, GTemp] = self.G(i);
96     res = ...

```

```

2*(1-nuTemp)*sqrt(1-n^2)*self.applied_stress(i)*a/(GTemp*n);
94     end
95
96     function res = f_1(self,b)
97         if abs(b)<10
98             res=(10-abs(b))/9;
99         else
100             res=0;
101         end
102     end
103
104     function res = f_2(self,b)
105         if abs(b)<10
106             res=(abs(b)-1)/9;
107         else
108             res=1;
109         end
110     end
111
112     function [self,res] = mim1(self,i)
113
114         function res = mi_(t)
115
116             direction_vectors = [
117                 [1 0 -1],%(1 1 1)
118                 [0 -1 1],
119                 [-1 1 0],
120                 [0 -1 -1],%(1 -1 1)
121                 [-1 0 1],
122                 [1 1 0],
123                 [1 1 0],%(-1 1 1)
124                 [-1 0 -1],
125                 [0 -1 1],
126                 [0 -1 -1],%(-1 -1 1)
127                 [-1 1 0],
128                 [1 0 1]
129             ];
130
131             normal.direction_vectors = [
132                 [1 1 1],%(1 1 1)
133                 [1 1 1],
134                 [1 1 1],
135                 [1 -1 1],%(1 -1 1)
136                 [1 -1 1],
137                 [1 -1 1],
138                 [-1 1 1],%(-1 1 1)
139                 [-1 1 1],
140                 [-1 1 1],
141                 [-1 -1 1],%(-1 -1 1)
142                 [-1 -1 1],
143                 [-1 -1 1]
144             ];

```

```

145
146     function res = normalize(vector)
147         length_vec = sqrt(vector(1)^2 + vector(2)^2 + ...
148             vector(3)^2);
149         res = [vector(1)/length_vec vector(2)/length_vec ...
150             vector(3)/length_vec];
151     end
152
153     function res = scalar_product(vector1,vector2)
154         res = vector1(1)*vector2(1) + ...
155             vector1(2)*vector2(2) + vector1(3)*vector2(3);
156     end
157
158     angle=0;
159     grain_number=ceil(1+3*(abs(t)-1)/2);
160
161     if abs(i) > 1
162         for a = 1:grain_number
163             %random load direction
164             load_direction_vec = [random('unif',0.0,2.0)-1 ...
165                 random('unif',0.0,2.0)-1 ...
166                 random('unif',0.0,2.0)-1];
167
168             orient_matrix=zeros(length(direction_vectors(:,1)),1);
169             for k = 1:length(direction_vectors(:,1))
170                 load_v=normalize(load_direction_vec);
171                 norm_v=normalize(normal_direction_vectors(k,:));
172                 dire_v=normalize(direction_vectors(k,:));
173                 value=abs( 1/( scalar_product( load_v, ...
174                     norm_v ) * scalar_product( load_v, ...
175                     dire_v ) ) );
176                 orient_matrix(k)=value;
177             end
178
179             [m,mi]=sort(orient_matrix);
180             lowest5index = mi(1:5);
181             angle=angle+mean(orient_matrix(lowest5index));
182         end
183         res = angle/grain_number;
184     else
185         res = 2.3;
186     end
187 end
188
189     res = 1 + 2*(mi_-(abs(i)) - 2.3) + 2.07*( 2/pi*atan(0.522*( ...
190         abs(i) - 1 ) * 2) ) ^1.86;
191
192 end
193
194 %constant mim1
195 function res = mim1.(self,i)

```

```

189         res = 1+2.07*(2/pi*atan( 0.522*(abs(i)-1)*2))^1.86;
190     end
191
192     function [self,res] = sigLi(self,miml,dmean,c,i)
193         [self,sigFLTemp] = self.sigFL(i);
194         res = sigFLTemp*miml*sqrt(dmean/(2*c)) * ...
            self.surfRoughnessVariance.;
195     end
196
197     function [self,res] = nc(self,sigLi,i)
198         [self,sigCompTemp] = self.sigComp(i);
199         res = cos(pi/2*((self.applied_stress(i)-sigLi)/sigCompTemp));
200     end
201
202     function [self,res] = ns(self,cml,c,nc)
203         res = cml/c*nc;
204     end
205
206     function [self,res] = dN(self,ns,nc,i)
207         [self,nuTemp] = self.nu(i);
208         [self,GTemp] = self.G(i);
209         [self,fTemp] = self.f(i);
210         if fTemp== 0
211             res = 0;
212         else
213             res = ( GTemp/(fTemp*(1 - ...
                nuTemp)*2*self.applied_stress(i)) )*( asin(nc) - ...
                asin(ns) );
214         end
215     end
216
217 end
218
219 methods ( Access = public )
220
221 %constructor
222 function self = classTM(app_stress,load_direction)
223     self.applied_stress_ = app_stress;
224     self.load_direction = load_direction;
225 end
226
227 %i is the current plastic zone side & j the opposite
228 function [self,res] = ...
    crack_position_by_dN(self,dN,ns,c,i,j,Crack_Structure,PL_Structure)
229
230 %the plastic zone is in the entire grain for the first step
231 if j==0
232     j=-sign(i);
233 end
234
235 [self,GTemp] = self.G(i);
236 [self,nuTemp] = self.nu(i);

```

```

237         [self,fTemp] = self.f(i);
238
239         res = abs(c*sin( ...
                dN/(GTemp/(fTemp*(1-nuTemp)*2*self.applied_stress(i))) ...
                + asin(ns) ));
240     end
241
242     %i is the current plastic zone side & j the opposite
243     function [self,res] = ...
                dadN(self,a,n,i,j,Crack_Structure,PL_Structure)
244
245         %the plastic zone is in the entire grain for the first step
246         if j==0
247             j=-sign(i);
248         end
249
250         [self,phiTemp] = self.phi(a,n,i);
251         [self,fTemp] = self.f(i);
252
253         res = fTemp*phiTemp;
254     end
255
256     function [dN,nc] = compute_long_crack(self,i,c,dmean,ns)
257         miml = self.miml(i);
258         [self,sigFLTemp] = self.sigFL(i);
259         sigLi = sigFLTemp*miml*sqrt(dmean/(2*c)) * ...
                self.surfRoughnessVariance_;
260         [self,sigCompTemp] = self.sigComp(i);
261         nc = cos(pi/2*((self.applied_stress(i)-sigLi)/sigCompTemp));
262         [self,GTemp] = self.G(i);
263         [self,nuTemp] = self.nu(i);
264         [self,fTemp] = self.f(i);
265
266         dN = ( GTemp/( fTemp*( 1 - nuTemp ...
                )*2*self.applied_stress(i) ) )*( asin(nc) - asin(ns) );
267     end
268
269     function matrix = statistics( self, i, ns, miml_c, length_c, ...
                roughness_c, miml_v, length_v, roughness_v )
270         matrix=zeros(4,1);
271
272         function value = dN(grain,m,l,r)
273             [self,sigFLTemp] = self.sigFL(grain);
274             sigLi_ = sigFLTemp*m*l/r;
275             [self,sigCompTemp] = self.sigComp(grain);
276             nc_ = cos( pi/2*(( self.applied_stress(grain) - sigLi_ ...
                )/sigCompTemp) );
277             [self,GTemp] = self.G(grain);
278             [self,nuTemp] = self.nu(grain);
279             [self,fTemp] = self.f(grain);
280
281             value = (GTemp/( fTemp*(1 - ...

```

```

        nuTemp)*2*self.applied_stress(grain) ) ...
        )*(asin(nc-) - asin(ns));
282     end
283
284     without_disp=dN(i,miml_c,length_c,roughness_c);
285
286     matrix(1,1)=dN(i,miml_v,length_c,roughness_c)-without_disp;
287     matrix(2,1)=dN(i,miml_c,length_v,roughness_c)-without_disp;
288     matrix(3,1)=dN(i,miml_c,length_c,roughness_v)-without_disp;
289     matrix(4,1)=0;
290
291     end
292
293     %does the crack propagate?
294     %i is the current plastic zone side & j the opposite
295     function [self, Crack_Structure, will_pro, disp_matrix] = ...
        is_propagating(self, i, j, will_pro, Crack_Structure, PL_Structure)
296
297     %the plastic zone is in the entire grain for the first step
298     if j==0
299         j=-sign(i);
300     end
301
302     dc = PL_Structure(i).length;
303     if abs(i)==1
304         %ddm = PL_Structure(1).length+PL_Structure(-1).length;
305         ddm = PL_Structure(i).length*2;
306     else
307         ddm = dc;
308     end
309
310     %global global_dmean;
311     %global_dmean(1,1) OR ...
        (Crack_Structure(i-1*sign(i)).d.mean*(abs(i)-1)+ddm)/abs(i)
312     current_step = struct('c', Crack_Structure(i - ...
        1*sign(i)).c+dc, 'd_mean', (Crack_Structure(i - ...
        1*sign(i)).d.mean*(abs(i) - 1)+ddm)/abs(i), 'nc', 0, ...
        'ac', 0, 'ns', 0, 'dN', 0, 'N', 0, 'is_blocked', false);
313
314     [self, miml] = self.miml(i);
315     [self, sigLi] = ...
        self.sigLi(miml, current_step.d.mean, current_step.c, i);
316     [self, current_step.nc] = self.nc(sigLi, i);
317
318     current_step.ac = current_step.c*current_step.nc;
319     [self, current_step.ns] = self.ns( Crack_Structure( i - ...
        1*sign(i) ).c, current_step.c, Crack_Structure( i - ...
        1*sign(i) ).nc );
320     [self, current_step.dN] = ...
        self.dN(current_step.ns, current_step.nc, i);
321
322     current_step.N = ...

```

```

    Crack_Structure(i-1*sign(i)).N+current_step.dN;
323
324     current_index=1+(1-sign(i))/2;
325     will_pro(1,current_index) = true;
326     [self,sigFLTemp]=self.sigFL(i);
327
328     %statistics
329     disp_matrix=zeros(4,1);
330     disp_matrix=self.statistics(i, current_step.ns, ...
        self.miml(i), sqrt(1/(2*abs(i)-1)), 1, miml, ...
        sqrt(current_step.d.mean/(2*current_step.c)), ...
        self.surfRoughnessVariance_ );
331
332     % stop the crack if ... OR if dN==0 or dN<0
333     if self.applied.stress(i)<sigLi || ...
        self.applied.stress<sigFLTemp || current_step.dN<=0
334         will_pro(1,current_index) = false;
335     end
336
337     current_step.is.blocked = ~will_pro(1,current_index);
338     Crack_Structure(i) = current_step;
339
340     end
341
342     end
343
344     end

```

## C.4 File classFP.m

```
1  % classFP.m class
2  % this is the class for Ferrite-Pearlite
3
4  classdef classFP
5
6      properties (SetAccess = private, GetAccess = public)
7
8          applied_stress_;
9          load_direction;
10
11         materialDist = [47 53];%Ferrite & Pearlite
12
13         sigFL = [260/2 385/2];%Ferrite & Pearlite
14         surfRoughnessVariance_ = normrnd(1.0,0.1);
15
16         sigComp_ = [140 268];%Ferrite: 70*2 & Pearlite: 134*2
17         nu_ = [0.28 0.28];%Ferrite & Pearlite
18         G_ = [82*10^3 82*10^3];%Ferrite & Pearlite
19
20         propertiesArray = ones(350,10)*(-1);
21         AVERAGE = 100;
22
23     end
24
25     methods ( Access = private )
26
27         function [self,res] = getValueByDist(self,i,propertyIndex)
28             current_index=1+(1-sign(i))/2;
29             if ...
30                 self.propertiesArray(abs(i), (propertyIndex-1)*2+current_index)==-1
31                 %for the first time, compute and store the value
32                 if propertyIndex==1
33                     matrixValue=self.sigFL;
34                 elseif propertyIndex==2
35                     matrixValue=self.sigComp;
36                 elseif propertyIndex==3
37                     matrixValue=self.nu;
38                 elseif propertyIndex==4
39                     matrixValue=self.G;
40                 elseif propertyIndex==5
41                     [self,sigFLTemp] = self.sigFL(i);
42                     if self.applied_stress_>sigFLTemp
43                         matrixValue=[ ...
44                             4.8938*10^(-16)*(self.applied_stress_)^5.4884 ...
45                             1.9279*10^(-20)*(self.applied_stress_)^7.0320 ...
46                             ];
47                     else
48                         matrixValue=[0 0];
49                     end
50                 end
51             end
52         end
53     end
54 end
```



```

45         end
46     end
47     %half the crack for both side
48     grainNumber=ceil(1+3*(abs(i)-1)/2);
49     valueToStore=-1;
50
51     % /\ always start inside a ferrite grain
52     if abs(i)==1
53         valueToStore = matrixValue(1);
54     elseif abs(i)<self.AVERAGE
55         r_ = randi(100,1,grainNumber);
56         a = self.materialDist;
57         c_ = cell2mat(arrayfun(@(a,matrixValue) ...
58             matrixValue+zeros(1,a), a, matrixValue, ...
59             'unif', 0));
60         valueToStore = mean(c_(r_));
61     else%the material properties are the average values.
62         valueToStore = ( ...
63             matrixValue(1)*self.materialDist(1) + ...
64             matrixValue(2)*self.materialDist(2) )/100;
65     end
66
67     self.propertiesArray( abs(i), ( propertyIndex - 1 ) * 2 ...
68         + current_index ) = valueToStore;
69     if (abs(i)==1)%for the first grain, the values are the ...
70         same
71         self.propertiesArray( abs(i), (propertyIndex-1)*2 ...
72             + 1 + (1-sign(-i))/2 ) = valueToStore;
73     end
74
75     res = self.propertiesArray( abs(i), ...
76         (propertyIndex-1)*2 + current_index );
77     else
78         %get the value if it was already computed
79         res = self.propertiesArray( abs(i), ...
80             (propertyIndex-1)*2 + current_index );
81     end
82 end
83
84 function [self,res] = sigFL(self,i)
85     %disp(['sigFL',num2str(i)]);
86     [self,res]=self.getValueByDist(i,1);
87 end
88
89 function [self,res] = sigComp(self,i)
90     %disp(['sigComp',num2str(i)]);
91     [self,res]=self.getValueByDist(i,2);
92 end
93
94 function [self,res] = nu(self,i)
95     %disp(['nu',num2str(i)]);
96     [self,res]=self.getValueByDist(i,3);

```

```

88     end
89
90     function [self,res] = G(self,i)
91         %disp(['G',num2str(i)]);
92         [self,res]=self.getValueByDist(i,4);
93     end
94
95     function [self,res] = f(self,i)
96         %[self,sigFLTemp] = self.sigFL(i);
97         [self,res]=self.getValueByDist(i,5);
98     end
99
100    function res = applied.stress(self,i)
101        res = self.applied.stress.;
102    end
103
104    function [self,res] = phi(self,a,n,i)
105        [self,nuTemp] = self.nu(i);
106        [self,GTemp] = self.G(i);
107        res = ...
108            2*(1-nuTemp)*sqrt(1-n^2)*self.applied.stress(i)*a/(GTemp*n);
109    end
110
111    function [self,res] = mim1(self,i)
112
113        function res = mi-(t)
114
115            direction.vectors = [
116                [1 0 -1],%(1 1 1)
117                [0 -1 1],
118                [-1 1 0],
119                [0 -1 -1],%(1 -1 1)
120                [-1 0 1],
121                [1 1 0],
122                [1 1 0],%(-1 1 1)
123                [-1 0 -1],
124                [0 -1 1],
125                [0 -1 -1],%(-1 -1 1)
126                [-1 1 0],
127                [1 0 1]
128            ];
129
130            normal.direction.vectors = [
131                [1 1 1],%(1 1 1)
132                [1 1 1],
133                [1 1 1],
134                [1 -1 1],%(1 -1 1)
135                [1 -1 1],
136                [1 -1 1],
137                [-1 1 1],%(-1 1 1)
138                [-1 1 1],
139                [-1 1 1],

```

```

139         [-1 -1 1],%(-1 -1 1)
140         [-1 -1 1],
141         [-1 -1 1]
142     ];
143
144     function res = normalize(vector)
145         length_vec=sqrt(vector(1)^2+vector(2)^2+vector(3)^2);
146         res=[vector(1)/length_vec vector(2)/length_vec ...
147             vector(3)/length_vec];
148
149     function res = scalar_product(vector1,vector2)
150         res=vector1(1)*vector2(1) + vector1(2)*vector2(2) ...
151             + vector1(3)*vector2(3);
152
153     end
154
155     angle=0;
156     grain_number=ceil(1+3*(abs(t)-1)/2);
157
158     if abs(i) > 1
159         for a = 1:grain_number
160             %random load direction
161             load_direction_vec = [random('unif',0.0,2.0)-1 ...
162                 random('unif',0.0,2.0)-1 ...
163                 random('unif',0.0,2.0)-1];
164
165             orient_matrix=zeros(length(direction_vectors(:,1)),1);
166             for k = 1:length(direction_vectors(:,1))
167                 load_v=normalize(load_direction_vec);
168                 norm_v=normalize(normal_direction_vectors(k,:));
169                 dire_v=normalize(direction_vectors(k,:));
170                 value = abs(1/( scalar_product( load_v, ...
171                     norm_v )*scalar_product( load_v, ...
172                     dire_v ) ) );
173                 orient_matrix(k)=value;
174             end
175
176             [m,mi]=sort(orient_matrix);
177             lowest5index = mi(1:5);
178             angle=angle+mean(orient_matrix(lowest5index));
179         end
180         res = angle/grain_number;
181     else
182         res = 2.3;
183     end
184
185 end
186
187 res = 1 + 2*( mi_-(abs(i)) - 2.3 ) + 2.07*( ...
188     2/pi*atan(0.522*( abs(i) - 1 )^2) )^1.86;
189
190 end

```

```

184
185 %constant miml
186 function res = miml.(self,i)
187     res = 1+2.07*(2/pi*atan( 0.522*(abs(i)-1)*2))^1.86;
188 end
189
190 function [self,res] = sigLi(self,miml,dmean,c,i)
191     [self,sigFLTemp] = self.sigFL(i);
192     res = sigFLTemp*miml*sqrt(dmean/(2*c)) * ...
193         self.surfRoughnessVariance;
194 end
195
196 function [self,res] = nc(self,sigLi,i)
197     [self,sigCompTemp] = self.sigComp(i);
198     res = cos(pi/2*((self.applied.stress(i)-sigLi)/sigCompTemp));
199 end
200
201 function [self,res] = ns(self,cml,c,nc)
202     res = cml/c*nc;
203 end
204
205 function [self,res] = dN(self,ns,nc,i)
206     [self,nuTemp] = self.nu(i);
207     [self,GTemp] = self.G(i);
208     [self,fTemp] = self.f(i);
209     if fTemp== 0
210         res = 0;
211     else
212         res = ( GTemp/(fTemp*( 1 - nuTemp ...
213             )*2*self.applied.stress(i)) )*( asin(nc) - ...
214             asin(ns) );
215     end
216 end
217
218 end
219
220 methods ( Access = public )
221
222 %constructor
223 function self = classFP(app.stress,load.direction)
224     self.applied.stress_ = app.stress;
225     self.load.direction = load.direction;
226 end
227
228 %i is the current plastic zone side & j the opposite
229 function [self,res] = ...
230     crack_position_by_dN(self,dN,ns,c,i,j,Crack_Structure,PL_Structure)
231
232     %the plastic zone is in the entire grain for the first step
233     if j==0
234         j=-sign(i);
235     end

```

```

232
233     [self,GTemp] = self.G(i);
234     [self,nuTemp] = self.nu(i);
235     [self,fTemp] = self.f(i);
236
237     res = abs(c*sin( ...
           dN/(GTemp/(fTemp*(1-nuTemp)*2*self.applied.stress(i))) ...
           + asin(ns) ));
238 end
239
240 %i is the current plastic zone side & j the opposite
241 function [self,res] = ...
           dadN(self,a,n,i,j,Crack_Structure,PL_Structure)
242
243 %the plastic zone is in the entire grain for the first step
244 if j==0
245     j=-sign(i);
246 end
247
248 [self,phiTemp] = self.phi(a,n,i);
249 [self,fTemp] = self.f(i);
250
251 res = fTemp*phiTemp;
252 end
253
254 function [dN,nc] = compute_long_crack(self,i,c,dmean,ns)
255     miml = self.miml(i);
256     %here i=self.AVERAGE to have average values
257     [self,sigFLTemp] = self.sigFL(self.AVERAGE);
258     sigLi = sigFLTemp*miml*sqrt(dmean/(2*c)) * ...
           self.surfRoughnessVariance;
259     [self,sigCompTemp] = self.sigComp(self.AVERAGE);
260     nc = cos(pi/2*((self.applied.stress(i)-sigLi)/sigCompTemp));
261     [self,GTemp] = self.G(self.AVERAGE);
262     [self,nuTemp] = self.nu(self.AVERAGE);
263     [self,fTemp] = self.f(self.AVERAGE);
264
265     dN = (GTemp/(fTemp*(1 - ...
           nuTemp)*2*self.applied.stress(i)))*( asin(nc) - ...
           asin(ns) );
266 end
267
268 function matrix = statistics(self, i, ns, miml_c, length_c, ...
           roughness_c, miml_v, length_v, roughness_v)
269     matrix=zeros(4,1);
270
271     function value = dN(grain,m,l,r)
272         [self,sigFLTemp] = self.sigFL(grain);
273         sigLi_ = sigFLTemp*m*l/r;
274         [self,sigCompTemp] = self.sigComp(grain);
275         nc_ = cos( pi/2*((self.applied.stress(grain) - ...
           sigLi_)/sigCompTemp) );

```

```

276         [self,GTemp] = self.G(grain);
277         [self,nuTemp] = self.nu(grain);
278         [self,fTemp] = self.f(grain);
279
280         value = (GTemp/(fTemp*( 1 - nuTemp ...
                )*2*self.applied.stress(grain)))*( asin(nc_) - ...
                asin(ns) );
281     end
282
283     without_disp=dN(self.AVERAGE,miml_c,length_c,roughness_c);
284
285     matrix(1,1)=dN(self.AVERAGE,miml_v,length_c,roughness_c)-without_disp;
286     matrix(2,1)=dN(self.AVERAGE,miml_c,length_v,roughness_c)-without_disp;
287     matrix(3,1)=dN(self.AVERAGE,miml_c,length_c,roughness_v)-without_disp;
288     matrix(4,1)=dN(i,miml_c,length_c,roughness_c)-without_disp;
289
290     end
291
292     %does the crack propagate?
293     %i is the current plastic zone side & j the opposite
294     function [self, Crack_Structure, will_pro, disp_matrix] = ...
        is_propagating(self, i, j, will_pro, Crack_Structure, PL_Structure)
295
296     %the plastic zone is in the entire grain for the first step
297     if j==0
298         j=-sign(i);
299     end
300
301     dc = PL_Structure(i).length;
302     if abs(i)==1
303         %ddm = PL_Structure(1).length+PL_Structure(-1).length;
304         ddm = PL_Structure(i).length*2;
305     else
306         ddm = dc;
307     end
308
309     %global global_dmean;
310     %global_dmean(1,1) OR ...
        (Crack_Structure(i-1*sign(i)).d_mean*(abs(i)-1)+ddm)/abs(i)
311     current_step = struct('c', Crack_Structure(i - ...
        1*sign(i)).c+dc, 'd_mean', (Crack_Structure(i - ...
        1*sign(i)).d_mean*(abs(i) - 1)+ddm)/abs(i), 'nc', 0, ...
        'ac', 0, 'ns', 0, 'dN', 0, 'N', 0, 'is_blocked', false);
312
313     [self,miml] = self.miml(i);
314     [self,sigLi] = ...
        self.sigLi(miml,current_step.d_mean,current_step.c,i);
315     [self,current_step.nc] = self.nc(sigLi,i);
316
317     current_step.ac = current_step.c*current_step.nc;
318     [self,current_step.ns] = self.ns( Crack_Structure( i - ...
        1*sign(i) ).c,current_step.c,Crack_Structure( i - ...

```

```

319         1*sign(i) ).nc );
        [self,current_step.dN] = ...
            self.dN(current_step.ns,current_step.nc,i);
320
321     current_step.N = ...
        Crack.Structure(i-1*sign(i)).N+current_step.dN;
322
323     current_index=1+(1-sign(i))/2;
324     will_pro(1,current_index) = true;
325     [self,sigFLTemp]=self.sigFL(i);
326
327     %statistics
328     disp_matrix=zeros(4,1);
329     disp_matrix=self.statistics(i, current_step.ns, ...
        self.miml(i), sqrt(1/(2*abs(i)-1)), 1, miml, ...
        sqrt(current_step.d.mean/(2*current_step.c)), ...
        self.surfRoughnessVariance_ );
330
331     % stop the crack if ... OR if dN==0 or dN<0
332     if self.applied_stress(i)<sigLi || ...
        self.applied_stress<sigFLTemp || current_step.dN<=0
333         will_pro(1,current_index) = false;
334     end
335
336     current_step.is_blocked = ~will_pro(1,current_index);
337     Crack.Structure(i) = current_step;
338
339     end
340
341     end
342
343     end

```

APPENDIX D  
*3D Surface*

Appendix C presents Scanning Electron Microscopy (SEM) images used for the 3D reconstruction of the surface roughness profile with photometric stereo technique.

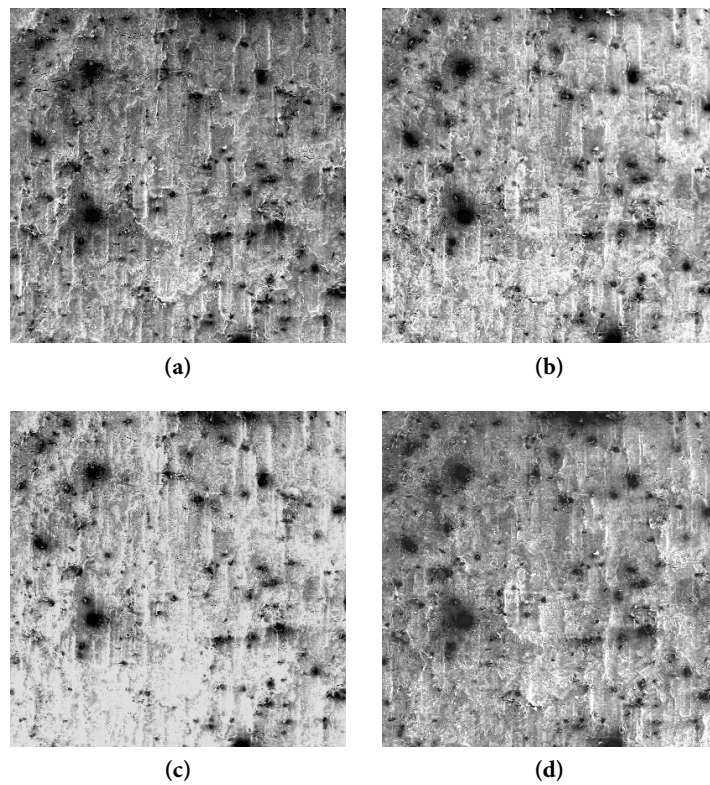
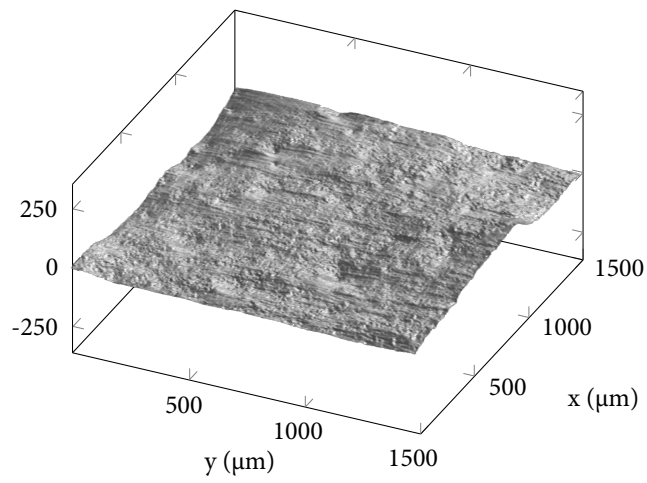


**Figure D.1** – 3D surface reconstruction using photometric stereo technique: (a)-(d) source SEM images.





(e)

**Figure D.1** – 3D surface reconstruction using photometric stereo technique: (e) 3D reconstructed surface.

## S-N-P fatigue curves using maximum likelihood

### Method for fatigue resistance curves with application to straight and welded rebars

— Luca D'Angelo<sup>1</sup>, Marina Rocha<sup>2</sup>, Alain Nussbaumer<sup>1</sup>, Eugen Brühwiler<sup>2</sup>

Published in EUROSTEEL 2014, September 10-12, 2014, Naples, Italy

### Introduction

When checking the fatigue life of steel bridges with concrete deck slabs, both steel details and embedded reinforcing steel bars (rebars) must be considered. In this paper a method for estimation of fatigue resistance curves is presented with application to straight and welded rebars. Rebar fatigue resistance is traditionally presented in the form of *S-N-P* curves which relate the applied stress range, *S*, to the *p*-quantile of fatigue life, *N*. These *S-N-P* curves are obtained from rebar fatigue tests at constant stress amplitudes. Test results for hot rolled (HR), cold worked (CW) and quenched and self-tempered (QST) rebars can be found in [1–7]. Both HR and CW rebars show a ductile cross section consisting of pearlite-ferrite microstructure and low or medium Carbon content [8, 9]; however, HR and CW rebars have been mainly replaced by QST rebars since the 1970's. QST rebars are produced from a specific thermal treatment called Thermex or Tempcore [10, 11] which results in a different microstructure at the surface and in the core. Typically the surface is a hard martensite, whereas the core consists of pearlite-ferrite. Fatigue datasets for different rebar connections such as lapping, coupling or welding as well as for corroded rebars can be found from tests performed in the 1970's.

<sup>1</sup>École Polytechnique Fédérale de Lausanne, Steel Structures Laboratory (ICOM), Switzerland

<sup>2</sup>École Polytechnique Fédérale de Lausanne, Structural Safety and Maintenance Laboratory (MCS), Switzerland

In the EN standards, characteristic  $S-N$  curves are created by fitting a linear regression to the experimental failure data points and translating the linear regression mean curve to the  $p$ -lower hyperbolic prediction bound (typically  $p=0.05$ ), at 1 million cycles [12]. This approach has several limitations: 1) run-out test results are neglected; 2) a constant amplitude fatigue limit (CAFL) (stress below which tested bars experience no fatigue damage) is arbitrarily chosen to begin at 1 million cycles for straight rebars and at 10 million cycles for welded rebars [13]; and 3)  $S-N$  curves are based on fatigue data scatter in the finite-life region ( $N$  less than 1 million cycles) resulting in less accuracy in the high cycle fatigue (HCF) region ( $N$  over 1 million cycles). The statistical method recommended by the EN standards is currently used in the standards for concrete structures [14]. Analysing the fatigue data using more statistically robust approaches may overcome some of these issues.

In this paper a Maximum Likelihood (ML) method-based approach is used together with Monte-Carlo Simulations (MCS) to estimate  $S-N-P$  curves of straight and welded rebars. Run-out test results are considered and particular attention is given to the position of the CAFL. The influence of rebar size and rebar type is studied. Comparisons between ML-based  $S-N-P$  curves and EN-based characteristic  $S-N$  curves are made. The approach proposed in this study is presented with application to straight and welded rebars but it has generic applicability for estimating fatigue  $S-N-P$  curves of fatigue sensitive details of steel bridges like welded and bolted connections.

## E.1 Statistical evaluation of S-N-P curves

This section presents the statistical method for estimation of characteristic  $S-N$  curves recommended by the EN standards [12], and presents the formulation for the ML-based approach.

### E.1.1 Statistical evaluation of S-N-P curves based on EN background documentation

A linear statistical model is used to define the relationship between the logarithm of the number of cycles to failure,  $Y = \ln(N)$ , and the logarithm of the nominal stress range,  $X = \ln(S)$ :

$$Y = \beta_0 + \beta_1 \cdot X + \varepsilon(0, \sigma) \quad (\text{E.1})$$

In Eq. 1,  $\beta_0$  and  $\beta_1$  are respectively the intercept and the slope of the  $S-N$  curve in

the log-log plane. It is assumed that the model error  $\epsilon$  can be modeled with a normal random variable, with an expected value equal to zero and standard deviation equal to  $\sigma$ . The model  $E(Y) = \beta_0 + \beta_1 \cdot X$ , which represents the mean value of  $\ln(N)$  for an assigned stress range, is fitted to the experimental dataset  $(y_1, x_1) \dots (y_n, x_n)$  using the least square method (LSM). Only failure points are considered.

According to the LSM, the unbiased, normally distributed estimators of model parameters are:

$$\hat{\beta}_1 = \sum_{i=1}^n \frac{(x_i - \bar{x})(y_i - \bar{y})}{(x_i - \bar{x})^2} = \frac{S_{xy}}{S_{xx}} \quad (\text{E.2})$$

$$\hat{\beta}_0 = \bar{y} - \beta_1 \bar{x} \quad (\text{E.3})$$

Since  $\hat{\beta}_0$  and  $\hat{\beta}_1$  are normally distributed in repeated sampling, it follows that  $\hat{Y} = \hat{\beta}_0 + \hat{\beta}_1 \cdot X$  is also normally distributed. In order to obtain the characteristic S-N curve, a  $100(\alpha)\%$  lower hyperbolic prediction bound can be determined around the mean regression line, using the following expression:

$$\hat{\beta}_0 + \hat{\beta}_1 \cdot x^* + t_{\alpha, n-2} \cdot StD \cdot \sqrt{1 + \frac{1}{n} + \frac{(x^* - \bar{x})^2}{S_{xx}}} \quad (\text{E.4})$$

In Eq. 4,  $StD$  is the sample standard deviation,  $t_{\alpha, n-2}$  is the  $\alpha$ -quantile of the Student's T distribution with  $n-2$  degrees of freedom and  $x^*$  is the natural logarithm of the reference stress range. Characteristic S-N curves are determined by translating the mean regression line to the corresponding point of the 5% lower hyperbolic prediction bound, at 1 million cycles. The constant amplitude fatigue limit (CAFL) is arbitrarily chosen to begin at 1 million cycles for straight bars and at 10 million cycles for welded bars [13].

### E.1.2 Statistical evaluation of S-N-P curves based on maximum likelihood approach

As previously mentioned, this EN standard approach is limited because: 1) run-out test results are neglected (loss of information) 2) the CAFL position is arbitrarily chosen; and 3) prediction bounds of linear regression curves are based on fatigue data scatter in the finite-life region resulting in less accuracy in the HCF region. To overcome these limitations, Pascual et al. [15] proposed a 5-parameter random fatigue limit (RFL) model that fit a nonlinear S-N curve having a random CAFL, to a complete fatigue dataset using ML estimation. In [15], characteristic S-N curves

were determined by finding lower  $\alpha$ -confidence bounds of  $p$ -quantile S-N curves (typically  $\alpha=75\%$  and  $p=0.05$ ). This ML model proposed by Pascual is still affected by two limitations: 1) the choice of the  $\alpha$ -confidence level for the lower bound of the  $p$ -quantiles is arbitrary; and 2) RFL-based S-N curves are nonlinear and are not easily comparable to the current standard linear S-N curves from the EN method.

This study proposes a bi-linear random fatigue limit (BLRFL) model that fits a bi-linear median S-N curve to a complete fatigue dataset, using again ML estimation. S-N-P curves are computed using Monte-Carlo Simulations (MCS), whereby the arbitrary choice of the  $\alpha$ -confidence level for the lower bound of the  $p$ -quantiles is not required.

The dependence between fatigue life and stress range is modeled as follows:

$$Y = \frac{\beta_0 + \beta_1 \cdot X}{H(X - V)} + \varepsilon(o, \exp(\sigma_Y)) \quad (\text{E.5})$$

Where  $H(\cdot)$  is the unit step function and  $V$  is the natural logarithm of CAFL.  $Y$  and  $V$  are assumed to be normal distributed random variables:

$$Y = \text{Normal}(\mu_Y, \exp(\sigma_Y)) \quad (\text{E.6})$$

$$V = \text{Normal}(\mu_V, \exp(\sigma_V)) \quad (\text{E.7})$$

The location parameter of the  $Y$  distribution is:

$$\mu_Y = \frac{(\beta_0 + \beta_1 \cdot X)}{H(X - V)} \quad (\text{E.8})$$

The conditional probability density function of  $Y|V$  is:

$$f_{Y|V} = \frac{1}{\sigma_Y} \phi_{Y|V}(x, y, v; \beta_0, \beta_1, \sigma_Y) \quad (\text{E.9})$$

The marginal probability density function of  $Y$  is:

$$f_Y = \int_{-\infty}^x \frac{1}{\sigma_Y \sigma_V} \phi_{Y|V}(x, y, v; \beta_0, \beta_1, \sigma_Y) \phi_V(v; \mu_V, \sigma_V) dv = f_Y(x, y; \underline{\theta}) \quad (\text{E.10})$$

Similarly the marginal cumulative distribution function of  $Y$  is:

$$F_Y = \int_{-\infty}^x \frac{1}{\sigma_Y} \phi_{Y|V}(x, y, v; \beta_0, \beta_1, \sigma_Y) \phi_V(v; \mu_V, \sigma_V) dv = F_Y(x, y; \underline{\theta}) \quad (\text{E.11})$$

Where the model parameter vector is indicated as:

$$\underline{\theta} = (\beta_0, \beta_1, \sigma_Y, \mu_V, \sigma_V) \quad (\text{E.12})$$

The sample likelihood is:

$$L(\underline{\theta}) = \prod_{i=1}^{N_{\text{tot}}} [f_Y(x_i, y_i; \underline{\theta})]^{\delta_i} [1 - F_Y(x_i, y_i; \underline{\theta})]^{1-\delta_i} \quad (\text{E.13})$$

where  $\delta_i = 1$  for the failure points and  $\delta_i = 0$  for run-out points. The negative sample log-likelihood is:

$$-\ln(L(\underline{\theta})) = -\left( \sum_{i=1}^{N_{\text{fail}}} \ln(f_Y(x_i, y_i; \underline{\theta})) + \sum_{i=1}^{N_{\text{runouts}}} \ln(1 - F_Y(x_i, y_i; \underline{\theta})) \right) \quad (\text{E.14})$$

The maximum likelihood estimate of the parameters vector  $\underline{\theta}$  is the vector that minimizes the negative sample log-likelihood.

$$E(\underline{\theta}) = [E(\beta_0), E(\beta_1), E(\sigma_Y), E(\mu_V), E(\sigma_V)] \quad (\text{E.15})$$

The inverse of the Fisher information matrix is the asymptotic covariance matrix  $\underline{\underline{C}}$  and gives information on the uncertainty of the stochastic model. Once the vector  $E(\underline{\theta})$  and the covariance matrix  $\underline{\underline{C}}$  have been computed, following MCS approach is used to estimate *S-N-P* curves:

- A stress range  $S$  is selected
- $10^6$  values of  $Y$  are sampled using  $E(\underline{\theta})$  and  $\underline{\underline{C}}$  information
- $P_f$  is computed for each value of the sample
- the  $p$ -quantile of the fatigue life,  $N$  that gives  $E(P_f) = p$ , for the selected stress range
- the process is repeated

## E.2 Results of statistical analysis

Five different experimental datasets were analysed using both the EN- and ML-based approaches. The five different data sets represent:

- HRCW straight rebars with diameter,  $d$ , smaller than 20 mm [1,2]
- HRCW straight rebars with  $d$  greater than 20 mm [1-3,7]
- QST straight rebars with  $d$  smaller than 20 mm [4][anonymous industrial dataset]

- QST straight rebars with  $d$  greater than 20 mm [4, 5]
- HR butt welded rebars (60-degree single-v weld joint) [6]

Figs. 1 to 3 (b) show the ML-based median S-N curves, the ML-based 5<sup>th</sup> quantile S-N curves and EN-based characteristic curves for the five considered datasets. ML-based 5<sup>th</sup> quantile nonlinear S-N curves were linearized (dotted lines) for direct comparison with EN-based characteristic S-N curves, using the following approach: 1) a horizontal line at CAFL<sub>5%</sub> is traced; 2) a straight line with slope equal to the slope of the median line and starting at the lower abscissa point of the nonlinear curve is intersected with the CAFL<sub>5%</sub> horizontal line; 3) the intersection point is the knee point. For all considered datasets, the ML-based 5<sup>th</sup> quantile S-N curves and EN-based characteristic curves are almost identical while  $N < 10^6$  cycles.

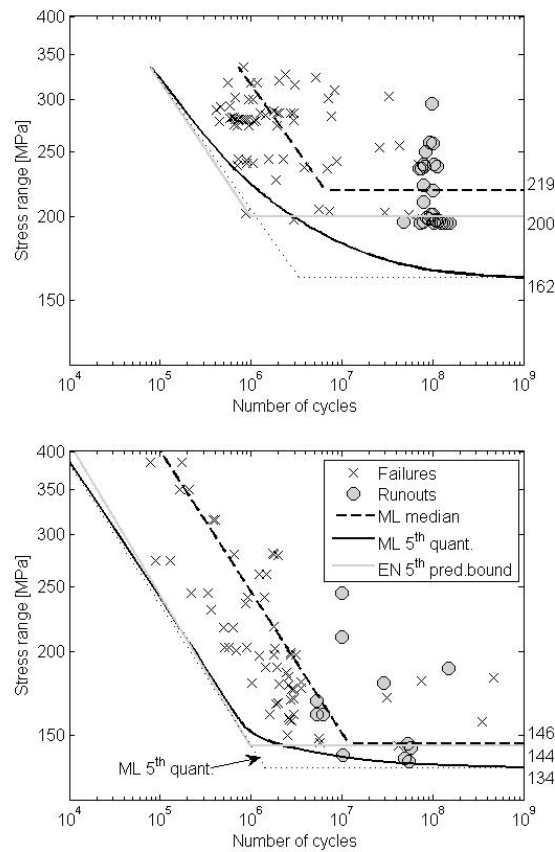


Fig. 1. S-N curves for HRCW straight rebars; (a) diameter  $\leq 20$  mm; (b) diameter  $> 20$  mm

Figs. 1 and 2 show that for HRCW and QST straight rebars ML-approach gives considerably lower estimation of the CAFL with respect to the EN-based approach:

ML-approach gives estimates of the knee point between 1.4 and 3.4 million cycles (see Table E.1).

Fig. 3 (a) shows that for HR welded rebars the EN-based approach gives an over conservative estimate of the CAFL of the characteristic curve with respect to the ML-based approach: ML-approach gives estimate of the knee point at 5.5 million cycles (see Table E.1).

For HRCW and QST straight rebars the fatigue resistance increases by decreasing the diameter of the section; for HRCW straight rebars the CAFL of the ML-based 5<sup>th</sup> quantile S-N curve decreases from 162 MPa ( $d \leq 20$  mm) to 134 MPa ( $d > 20$  mm) while the fatigue resistance of the ML-based 5<sup>th</sup> quantile curve at  $10^6$  cycles decreases from 224 MPa ( $d \leq 20$  mm) to 152 MPa ( $d > 20$  mm). For QST straight rebars, the CAFL of the ML-based 5<sup>th</sup> quantile S-N curve decreases from 214 MPa ( $d \leq 20$  mm) to 188 MPa ( $d > 20$  mm) while the fatigue resistance of the ML-based 5<sup>th</sup> quantile curve at  $10^6$  cycles decreases from 234 MPa ( $d \leq 20$  mm) to 107 MPa ( $d > 20$  mm) (see Table E.1).

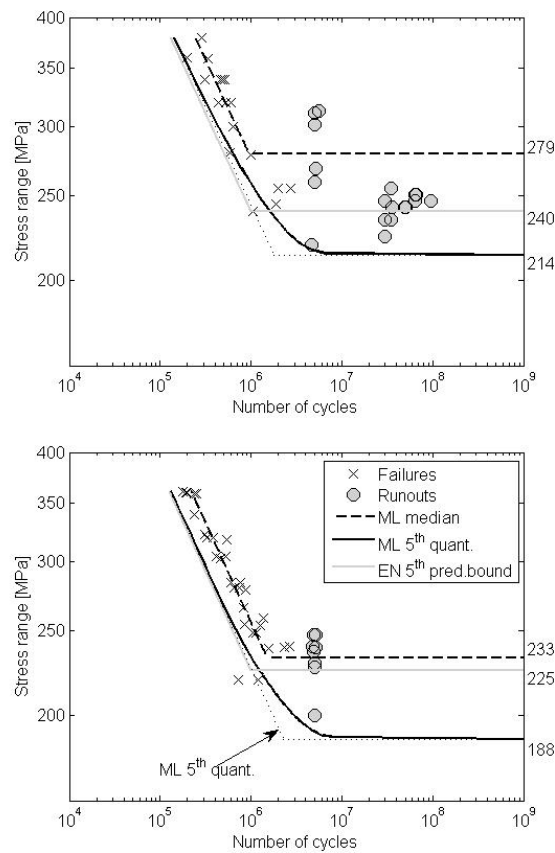
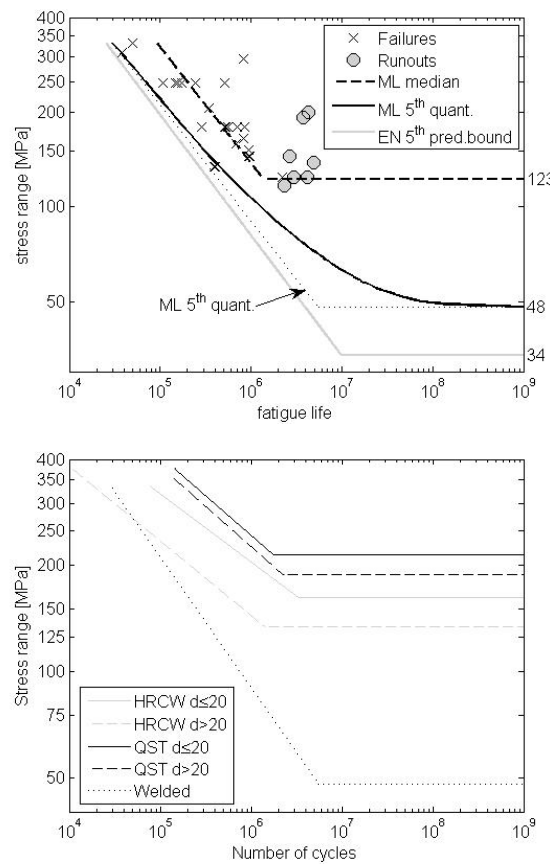


Fig. 2. S-N curves for QST straight rebars; (a) diameter  $\leq 20$  mm; (b) diameter  $> 20$  mm



**Table E.1** – Summary of characteristic values of ML-based linearized S-N curves

Type of rebars	Slope	CAFL <sub>50%</sub>	CAFL <sub>5%</sub>	knee point	S (N=10 <sup>6</sup> ) <sub>5%</sub>
HRCW d<20 mm	-5.17	219 MPa	162 MPa (200 MPa) <sup>3</sup>	3.4 × 10 <sup>6</sup>	224 MPa
HRCW d>20 mm	-4.72	146 MPa	134 MPa (144 MPa)	1.4 × 10 <sup>6</sup>	152 MPa
QST d<20 mm	-4.46	279 MPa	214 MPa (240 MPa)	1.8 × 10 <sup>6</sup>	258 MPa
QST d>20 mm	-4.39	233 MPa	188 MPa (225 MPa)	2.3 × 10 <sup>6</sup>	234 MPa
Welded	-2.71	123 MPa	48 MPa (34 MPa)	5.5 × 10 <sup>6</sup>	107 MPa



*Fig. 3. (a) S-N curves for HR welded rebars (b) ML 5<sup>th</sup> quant. linearized S-N curves for all experimental datasets*

ML-based 5<sup>th</sup> quantile S-N curves were plotted in Fig. 3 for the five considered datasets: both for d<20 mm and for d>20 mm QST straight rebars show higher fatigue resistance with respect to HRCW straight rebars. HR welded rebars have the by far lowest fatigue resistance both in terms of CAFL and of stress range at 10<sup>6</sup> cycles.

*Figs. 2 and 3 (a)* show that QST straight rebars and HR welded rebars have a small deviation of 5<sup>th</sup> quantile curve from the median curve in the finite life region and higher deviation in HCF region. *Fig. 1 (a)* shows that HRCW ( $d > 20$  mm) straight rebars have high deviation both in finite life region and in HCF region; HRCW ( $d > 20$  mm) straight rebars have high deviation in finite life region and a smaller deviation in HCF region.

### **E.3 Discussion of statistical analysis results**

Comparison of the ML-based S-N curves and the EN-based characteristic curves in the HCF region for HRCW and QST straight rebars, indicates that the arbitrary assumption of having the CAFL at  $10^6$  cycles is unsafe since ML estimates of the S-N curve knee point lie between 1.4 and 3.4 million cycles. On the contrary, comparison of ML-based S-N curves and EN-based characteristic curves in the HCF region for HR welded rebars, indicate that the arbitrary assumption of having the CAFL at  $10^7$  cycles seems is over conservative since the ML estimate of knee point of the S-N curve lies at 5.5 million cycles.

ML-based linearized 5<sup>th</sup> quantile S-N curves indicate that fatigue resistance of HRCW and QST straight rebars decreases as the diameter increases. For a given diameter interval, QST straight rebars have higher fatigue resistance with respect to HRCW straight rebars. HR welded rebars have the lowest fatigue resistance within all analysed datasets.

High deviation of the ML-based 5<sup>th</sup> quantile curve from the median curve was observed in HCF region for QST straight rebars, HRCW ( $d \leq 20$  mm) straight rebars and HR welded rebars: this is due to the fact that the experimental datasets are highly dispersed in the HCF region. On the contrary a small standard deviation was observed in HCF region for HRCW straight ( $d > 20$  mm) rebars, which is probably due to the fact that only run-out points exist at lowest stress ranges in the experimental datasets.

In conclusion the findings of this paper suggest that the limitations included in the current EN recommendations for statistical evaluations of characteristic S-N curves lead to incoherent fatigue resistance estimation in the HCF region for all types of analysed rebars. The ML-approach proposed herein constitutes a powerful tool that can be used to re-define the characteristic S-N curves for straight and welded rebars by taking in account both rebar type and size effect. The estimation of the characteristic S-N curves in the HCF region is directly related to experimental

data and the coherence of the estimates can be ameliorated by increasing the significance of the dataset information in the HCF region. Furthermore it has to be noted that the ML-approach is presented with application to straight and welded rebars but it has generic applicability for estimating fatigue *S-N-P* curves of fatigue sensitive details of steel bridges like welded and bolted connections.

## **Acknowledgements**

The authors wish to thank Professor Michael Havbro Faber for his suggestions on development of statistical method.

---

## *Bibliography*

---

- [1] Tilly G.P., Oct. 1979, Fatigue of Steel Reinforcement Bars in Concrete: a Review, *Fatigue & Fracture of Engineering Materials and Structures*, vol. 2, no. 3, pp. 251-268.
- [2] Tilly G.P., Jan. 1984, Fatigue testing and performance of steel reinforcement bars, *Matériaux et Constructions*, vol. 17, no. 97, pp. 43-49.
- [3] Rabbat B.G., Corley W.G., 1984, Long-time fatigue properties of high yield reinforcing bars, *Matériaux et Constructions*, vol. 17, no. 97, pp. 35-38.
- [4] Zheng H., Abel A., 1999, Fatigue properties of reinforcing steel produced by TEMPCORE process, *Journal of Materials in Civil Engineering*, vol. 11, no. 2, pp. 158-165.
- [5] Donnel M.J., Spencer W., Abel A., Fatigue of Tempcore reinforcing bars - the effect of galvanizing, *10<sup>th</sup> Australasian Conference on the Mechanics of Structures and Materials*, 1986, pp. 327-332.
- [6] Barone M.R., Cannon J.P., Munse W.H., 1974, "Fatigue behavior of reinforcing steel bars", *IHR-64*
- [7] Hanson J.M., Burton K.T., Hognestad E., 1968, Fatigue Tests of Reinforcing Bars - Effect of Deformation Pattern, *Journal of PCA Research and Development Laboratories*, vol. 10, no. 3, pp. 2-13.
- [8] Ray A., Mukerjee D., Sen S.K., Bhattacharya A., Dhua S.K., Prasad M.S., Banerjee N., Popli A.M., Sahu A.K., June 1997, Microstructure and Properties of Thermomechanically Strengthened Reinforcement Bars : A Comparative Assessment of Plain-Carbon and Low-Alloy Steel Grades, *Journal of Materials Engineering and Performance*, vol. 6, pp. 335-343.

- [9] MacGregor J.G., Jhamb I.C., Nuttal N., 1971, Fatigue Strength of Hot Rolled Deformed Reinforcing Bars, *ACI Journal*, pp. 169-179.
- [10] Rehm G., Russwurm D., 1977, Assessment of Concrete Reinforcing Bars made by Tempcore Process, *Betonwers + Fertigteil-Technik*, vol. 6, pp. 300-307.
- [11] Virmani Y.P., Wright W., Nelson R.N., 1991, Fatigue Testing for Thermex Reinforcing Bars, *Public Roads*, vol. 55, no. 3, pp. 72-78.
- [12] Eurocode EN 1993 - Part 1 - Background Documentation, European Committee for Standardization, Bruxelles, 1989.
- [13] Eurocode 1992: Design of concrete structures - Part 1-1: General rules and rules for buildings. European Committee for Standardization, Bruxelles, 2005.
- [14] fib Model Code for Concrete Structures, Fédération internationale du béton, 2013.
- [15] Pascual F.G., Meeker W.Q., 1999, Estimating Fatigue Curves With the Random Fatigue-Limit Model, *Technometrics*.

---

## Curriculum Vitae

---

Marina ROCHA PINTO PORTELA NUNES

Born: 1983  
Nationality: Brazilian

 [marina.rocha@alumni.epfl.ch](mailto:marina.rocha@alumni.epfl.ch)



### EDUCATION

---

- 2010-2014 **PhD** in *Structural Engineering*, Swiss Federal Institute of Technology in Lausanne – EPFL, Lausanne, SWITZERLAND  
Thesis entitled: *Fatigue Behaviour of Steel Reinforcement Bars at Very High Number of Cycles*  
Directors: Prof. E. Brühwiler and Prof. A. Nussbaumer
- 2007-2010 **Master of Science** in *Structural Engineering*, Polytechnic School at the University of São Paulo – EPUSP, São Paulo - SP, BRAZIL  
Thesis entitled: *A new algorithm for the modeling of Fracture Mechanics using Boundary Element Method*  
Director: Prof. Dr. Marcos Aurélio Marques Noronha
- 2002-2007 **Bachelor** in *Civil Engineering*, Federal University of Piauí – UFPI, Teresina - PI, BRAZIL  
Graduate Research: *Structural analysis of plane frames for infrastructure project - comparison between classical methods and Finite Element Method.*

### TEACHING AND PROFESSIONAL EXPERIENCES

---

- 2011-2013 **Teaching** EPFL, Lausanne, SWITZERLAND  
Description: Teaching assistant for courses in *Existing structures, structural safety & reliability and aesthetics of structures* at the School of Architecture, Civil and Environmental Engineering (ENAC) of EPFL. Supervision of master and undergraduate projects at EPFL.

- 2008 **Structural Engineer** Celenge Engenharia, São Paulo - SP, BRAZIL  
Description: Structural calculation of bridges ; design of slabs, beams and calculation of forms. Checking of conditions of stability and design of retaining walls.
- 2006 *Internship* as **Site Manager** Construtora CAXÉ, Teresina - PI, BRAZIL  
Description: Supervision of building sites such as schools, squares and housing estates. Update schedules of work with the physical and financial progress and reporting of the work week.
- 2005-2006 *Internship* as **Structural Engineer** Maloca Arquitetura e Estruturas, Teresina - PI, BRAZIL  
Description: Structural calculation of infrastructure projects such as houses, with design of slabs, beams. Structural calculation of bridges with design of foundations.

#### HONORS AND AWARDS

---

- 2014 **3<sup>rd</sup> prize** ENAC Doctoral Poster, EPFL
- 2008-2009 **Postgraduate research scholarship** FAPESP
- 2005-2006 **Graduate research scholarship** Institutional Program of Scientific Initiation
- 2006 **Poster selected for presentation** XV Seminar of Scientific Initiation, UFPI

#### JOURNAL PAPERS

---

- 2014 Rocha, M., Michel, S., Brühwiler, E. & Nussbaumer, A. Very high cycle fatigue tests of quenched and self-tempered steel reinforcement bars. *Materials and Structures* (submitted).
- 2014 Rocha, M., Brühwiler, E. & Nussbaumer, A. Geometrical and material characterisation of quenched and self-tempered steel reinforcement bars. *Journal of Materials in Civil Engineering* (submitted).
- 2014 Rocha, M., Brühwiler, E. & Nussbaumer, A. Microstructural influence on the scatter in the fatigue life of steel reinforcement bars. *International Journal of Fatigue* (submitted).
- 2014 Rocha, M., Brühwiler, E. & Nussbaumer, A. Fatigue behaviour prediction of steel reinforcement bars using an adapted Navarro and De Los Rios model. *International Journal of Fatigue* (submitted).

#### CONFERENCE PROCEEDINGS

---

- 2014 D'Angelo, L.; Rocha, M.; Nussbaumer, A. & Brühwiler, E. S-N-P fatigue curves using maximum likelihood. *7<sup>th</sup> Conference on Steel and Composite Structures*, Napoli, Italy (accepted).
- 2012 Brühwiler, E.; Rocha, M., Treacy; M. A., Bittencourt, T. N.; & Neto, A. P. C. Updating existing railway bridges based on monitoring data. *Proceedings Bridge Maintenance, Safety, Management, Resilience and Sustainability* (Vol. 1, No. EPFL-CONF-180269, pp. 2820-2826). CRC Press/Balkema.
- 2012 Rocha, M.; & Brühwiler, E. Prediction of fatigue life of reinforced concrete bridges using Fracture Mechanics. *Proceedings Bridge Maintenance, Safety, Management, Resilience and Sustainability* (Vol. 1, No. EPFL-CONF-180270, pp. 3755-3761). CRC Press/Balkema.
- 2009 Nunes, M. R. P. P.; Noronha, M. A. M. Um novo algoritmo para modelagem de Mecânica da Fratura usando o Método dos Elementos de Contorno. *XXX Iberian Latin American Congress on Computational Methods in Engineering (CILAMCE)*, Búzios, Brazil.

#### LANGUAGES

---

Portuguese, mother tongue  
English, fluent  
French, intermediate

#### COMPUTER SKILLS

---

Document Preparation System:  $\LaTeX$ , Microsoft Office (Word, Excel, PowerPoint)  
Finite Element Software: Abaqus  
Computer Programming: Java, Visual Basic & VBA, Delphi, Netbeans, Eclipse, UML  
Numerical Computing: Matlab  
Computer-Aided Design: AutoCAD  
Vector Graphics Editor Application: Inkscape



